UNIVERSITY OF MIAMI

STUDY OF 3-DIMENSIONAL CO-FLOW JET AIRPLANE AND HIGH-RISE
BUILDING FLOW USING CFD SIMULATION

By

John Aguirre

A THESIS

Submitted to the Faculty
of the University of Miami
in partial fulfillment of the requirements for
the degree of Master of Science

Coral Gables, Florida

December 2008

UNIVERSITY OF MIAMI

A thesis submitted in partial fulfillment of
the requirements for the degree of
Master of Science

STUDY OF 3-DIMENSIONAL CO-FLOW JET AIRPLANE AND HIGH-RISE
BUILDING FLOW USING CFD SIMULATION

John Aguirre

Approved:

—————————————————
Gecheng Zha, Ph.D.
Associate Professor of
Mechanical & Aerospace Engineering

—————————————————
Kau-Fui Vincent Wong, Ph.D.
Professor of
Mechanical & Aerospace Engineering

—————————————————
Singiresu S. Rao, Ph.D.
Professor and Chairman of
Mechanical & Aerospace Engineering

—————————————————
Terri A. Scandura, Ph.D.
Dean of the Graduate School

—————————————————
Norman G. Einspruch, Ph.D.
Professor of
Electrical & Computer Engineering

AGUIRRE, JOHN   (M.S., Mechanical Engineering)

<u>Study of 3-Dimensional Co-Flow Jet Airplane</u>   (December 2008)

<u>and High-Rise Building Flow Using CFD Simulation</u>

Abstract of a thesis at the University of Miami.

Thesis supervised by Professor Gecheng Zha.

No. of pages in text. (112)

The purpose of this thesis is to design and study an aircraft which implements the Co-Flow Jet (CFJ) airfoil concept, as well as to study the CAARC standard high-rise building. The design concept is verified mainly by the use of a Computational Fluid Dynamics (CFD) package. A thorough methodology for geometry and mesh generation is developed, and subsequently applied to the two cases.

The first case studied is that of the CFJ Airplane (CFJA). It consists of a three-dimensional, highly blended, flying wing geometry implementing the Co-Flow Jet airfoil concept. Though a thorough comparison to a baseline geometry, it is shown that usage of the CFJ airfoil cross-section greatly improves aircraft performance by increasing lift, reducing drag, and providing a source of thrust over the operational range of angles of attack. A steady state CFD simulation is used for this case, as the air flow around an airfoil cross-section is inherently steady for attached flows. CFD results are used to support the "Engineless Aircraft" concept, where the CFJ airfoil is used as the sole form of propulsion.

The second case studied consists of a rectangular high-rise building undergoing a wind condition with Mach number of 0.1 and a Reynolds number of 160000. Due to the non-streamlined geometry of the building cross-section, aerodynamic instabilities

due to fluid separation are present, and therefore an unsteady CFD analysis is necessary to fully resolve all of the flow phenomena. Preliminary steady state results are presented, and a plan is laid down for the future study of this highly complex case.

Results are presented for a variety of angles of attack in the case of the CFJA, and for the main flow direction in the case of the CAARC building. Results are compared with baseline geometry in the case of the CFJ Airplane. The CFJ Airplane case is simulated using a 3rd order steady state scheme, which is sufficient to achieve valid results for the flow regime. The CAARC building, which has inherent flow separation, requires the use of high order schemes.

Acknowledgment

This research spanning two years of work would not have been possible without the constant help and support of many of my friends and colleagues, and thus I would like to offer them my deepest gratitude.

I would first like to thank my mentor and academic adviser, Dr. Gecheng Zha for his endless direction and encouragement. Without his valuable support, instruction, and supervision this work would not have been possible.

I would also like to thank my colleague, Bao-Yuan Wang for his constant help and instruction. Whenever in need of help, he was always willing to entertain my questions and further my knowledge of CFD.

My deepest gratitude goes to my friend and my better half, Suzanne Mouzaffar, who always had words of encouragement, even when problems seemed unsurmountable.

Contents

List of Figures

List of Tables

List of Symbols

$(L/D)_{max}$ Maximum lift to drag ratio

α Angle of attack

α thermal diffusivity

$\bar{p}_{total}$ Non-dimensionalized total pressure

$\bar{T}_{total}$ Non-dimensionalized total temperature

Δ Largest spacing of the grid cell in DES

$\dot{m}$ Mass flow rate

η Pump efficiency

γ Ratio of specific heats

λ Eigenvalues

$\mathbf{A}$ Jacobian

$\mathbf{E^c}, \mathbf{E^p}$ Split flux vectors corresponding to convective and acoustic terms

$\mathbf{E}, \mathbf{F}, \mathbf{G}$ inviscid flux vectors in x, y, and z directions

$\mathbf{I}$ Identity matrix

$\mathbf{l}, \mathbf{m}, \mathbf{n}$ Normal vectors

$\mathbf{Q}$	vector of conservative variables
$\mathbf{R}, \mathbf{S}, \mathbf{T}$	viscous flux vectors in x, y, and z directions
$\mathbf{V}$	velocity vector
μ	molecular viscosity
μ_t	Eddy viscosity
ν	kinematic viscosity
ω	vorticity
ρ	density
τ_{ij}	viscous stress tensor
θ_1, θ_2	Angles of CFJ injection and suction slots
$\tilde{a}$	Roe-averaged speed of sound
$\tilde{h}$	Roe-averaged total enthalpy
$\tilde{T}$	Eigenvalue matrix using Roe's averages
$\tilde{u}$	Roe-averaged speed of sound
a	Speed of sound
A_j	Jet area
C_D	Three-dimensional drag coefficient
C_d	Two-dimensional drag coefficient
C_L	Three-dimensional lift coefficient
C_l	Two-dimensional lift coefficient

C_p	Surface pressure coefficient
c_p	Specific heat capacity at constant pressure
D	Drag
d	Distance to the nearest surface in SA model
e	total energy per unit mass
f	oscillation frequency
$F_{x_{cfj}}, F_{y_{cfj}}$	CFJ jet effects in x and y directions
H	Total building height
h	Height
h	Total enthalpy
L	Lift
l	Mixing length in BL model
L/D	Aerodynamic efficiency
l_t, m_t, n_t	Moving grid velocities
M	Mach number
P	Power
p	Pressure
p_∞	Incoming flow static pressure
p_{total}	Total pressure
Pr	Prandtl number

Q_x, Q_y, Q_z heat flux terms in x, y, and z directions

q_x, q_y, q_z molecular heat flux in x, y, and z directions

R'_x, R'_y Surface integral forces in x and y directions

Re Reynolds number

St Strouhal number

T Temperature

t time

T_∞ Incoming flow static temperature

T_{total} Total temperature

TE Truncation error

u, v, w velocity components in x, y, and z directions

V_j Jet velocity

x, y, z Cartesian coordinate directions

y^+ Dimensionless distance to the wall

Chapter 1

Introduction

Since the beginning of powered flight, the design approach of separating the thrust and lift generating systems in aircraft has been taken. This approach has been very successful in the past, and has become the dominating paradigm. Recently, aircraft design has begun to shift from a system where the fuselage and wings are completely separate, to the Blended Wing Body (BBW) or Flying Wing (FW) system, where both fuselage and wing are blended into one structure. This approach has been shown to increase lift generation by having the entire craft contribute, as well as lead to higher fuel efficiency [1–4]. While the joining of structural systems has been much discussed, there have been few attempts to join the lift and thrust generating systems. One alternative to achieving this goal is the use of the Co-Flow Jet (CFJ) airfoil system. The present work attempts to utilize this concept in the design of the Co-Flow Jet Airplane (CFJA). The design and study of this aircraft is the main focus of this thesis.

As a secondary goal, the same tools applied to the design and validation of the CFJA have been used to begin the study of a high-rise building under high wind conditions. This constitutes a more difficult case due to the unstable aerodynamic properties of the problem. Because fluid separation is inherent to the design of a

building, the case is far more turbulent, and thus the use of a more advanced scheme and turbulence model is necessary.

1.1 Blended Wing Body and Flying Wing Aircraft

For five decades, the prevalent design of aircraft has been that of fixed wings attached to a cylindrical fuselage, with a rear tail added for stability. While this design has been very useful, and therefore has been very extensively studied, it is not the optimal aircraft configuration. This is the case because, by separating the lifting wings and the non-lifting fuselage, the aerodynamic efficiency of the entire system is compromised. The fuselage performs the function of carrying payload, yet contributes nothing to the aerodynamics of the aircraft other than added drag. The wings alone provide the lift required to fly the aircraft. A new, more efficient type of aircraft configuration would increase aircraft performance and fuel efficiency, improve payload capacity, and therefore reduce the costs of operating aircraft. This need can be fulfilled by the use of a Blended Wing Body or Flying Wing configuration. The Blended Wing Body configuration consists of a fuselage section and a wing section which are geometrically blended together, with the fuselage having an airfoil cross-section. The airfoil cross sections of the fuselage and wing may be different, varying with the specific design. The Flying Wing configuration, on the other hand, has no discernible fuselage section.

When both the wings and the fuselage are blended into one aerodynamically lifting body, the maximum Lift to Drag ratio $(L/D)_{max}$ increases by as much as 20% over a traditional "tube and plank" configuration [1]. This occurs because, by blending the two sections, and giving the new fuselage an airfoil cross-section, it is now also contributing to the overall lift produced by the aircraft. That is, there is no longer any wasted surface area, all of it is made to contribute to the aerodynamic performance of the aircraft. Another advantage to this design is that by blending

the two geometries, the whetted surface area to volume ratio of the aircraft increases. This leads to an increase in the amount of payload that can be carried, as well as a lowering of interference drag by avoiding sharp corners [3]. In fact, the Direct Operating Costs (DOC) per passenger may be improved by as much as 15% over currect airplanes, while simultaneously increasing the number of passengers that can be accomodated within a similarly-sized aircraft [2]. Another advantage of a BWB of FW configuration is the lack of a tail. While some stability issues are still under consideration, its removal also reduces the amount of drag created by the aircraft. All of these effects can lead to an overall increase in the fuel efficiency of the system. The increase in fuel efficiency will lead to lower costs for airlines, as well as a decrease in CO_2 emissions [4]. One further advantage of using this design, is that the structural design can be simplified, and the overall structure becomes stiffer.

1.2   Building Aerodynamics

Unlike the case of aircraft, where fluid separation leads to stall and is thus avoided at all costs, it is an integral part of building aerodynamics. Generally, the shape of a building, and the relatively low wind speeds which it encounters means that fluid separation is constantly present, and thus the aerodynamic instabilities which it causes are the main source of effects.

In a rectangular building, the separated flow on the wall facing away from the wind direction will cause locally low pressure. On the opposite wall, which is facing the wind direction, a stagnation point will occur where local pressure is relatively high. The large pressure gradient produced by the flow pattern will then subject the building to large forces. A building must be designed such that it can be both rigid and flexible enough to sustain its integrity under high wind conditions, and still remain comfortable for the inhabitants.

One phenomenon which can lead to disastrous results in an ill-designed building is vortex shedding. At certain flow conditions, the flow around the building might behind to create low-pressure vortices on alternating sides of the building to shed and head downstream. These low pressure vortices will pull the building to one side or the other in an alternating fashion. This phenomenon can lead to violent oscillations which can amplify and become strong enough to cause serious damage. This vortex shedding can be characterized by the dimensionless Strouhal number, which is defined as

$$St = \frac{fL}{U} \tag{1.1}$$

where f is the frequency of the vortex shedding, L is the width of the building, and U is the flow velocity past the building. This allows us to calculate the frequency of the oscillations if we note that the Strouhal number is a function of the Reynolds number as

$$St = 0.198 \left(1 - \frac{19.7}{Re}\right) \tag{1.2}$$

It is important to be able to predict this frequency in order to avoid structural damage. If the frequency of vibration approaches the natural frequency of the building, the amplitude of the motion of the structure can become so high as to cause severe damage or even total destruction.

1.3 Computational Fluid Dynamics

Computational Fluid Dynamics (CFD) has become one of the most important tools in the design of structures requiring the understanding of fluid effects. It is currently being widely used to evaluate the design of systems as varied as engines, aircraft,

watercraft, spacecraft, and buildings. An effective CFD code is capable of making engineers aware of problems in their design before it is too late or too expensive to correct them, and thus can save companies valuable time and resources. In the case of aircraft design, where structures are generally streamlined, CFD has become a leading tool in design evaluation. The lack of inherent fluid separation in the geometries involved makes even simpler schemes not including sophisticated turbulence models reasonably accurate. In the case of building design, however, where the involved geometries are more often angular and not streamlined, more advanced CFD methods must be used to capture the vortexes and other phenomena caused by turbulence and fluid separation. In the present work, both of these cases are examined and simulated using the FASIP CFD code developed at the University of Miami Aerodynamics and CFD Lab.

The first examined case is that of the Co-Flow Jet Airplane. This conceptual aircraft designed at the University of Miami [5] makes use of the Flying Wing configuration, where the fuselage and wings are seamlessly blended together into one body. Furthermore, the fuselage has the same airfoil cross-section as the wings. In this sense, the aircraft is a single "Flying Wing". This aircraft also makes use of the CFJ airfoil which was recently developed by Zha et al. [6–9]. The CFJ airfoil, which will be explained in further detail, has been shown by both CFD simulation and experimental results to greatly increase aircraft performance, while simultaneously producing reduced drag, and at some angles of attack, net thrust. Both two and three dimensional CFD simulations are run on a range of angles of attack for both the baseline and CFJ configurations. The performance of both of these cases is compared and examined.

The second examined case is that of the Commonwealth Advisory Aeronautical Research Council standard tall building. The CAARC tall building is an 8 : 1 : .75 rectangular high-rise building, and is simulated with CFD in high-wind conditions.

Due to the rectangular cross-section of the building, fluid separation is inherent in the design, even at very low wind speeds. This highly turbulent flow will lead to vortex shedding. In order to correctly capture these phenomena, it is necessary to have a very fine mesh and to use a high order unsteady scheme. Both a 3rd order steady, and a 5th order unsteady scheme are used to simulate the flow, and results are compared.

Chapter 2

CFD Simulation

2.1 Governing Equations

Fluid flow is governed by the Navier-Stokes Equations. These are a set of second-order nonlinear partial differential equations. Due to their non-linearity, analytical solutions for a vast majority of cases are not available nor practical. Therefore, the best way to obtain solutions to the fluid-flow problem in realistic conditions is to use numerical methods. Computational Fluid Dynamics (CFD) is the answer to this need. The general three-dimensional Navier-Stokes equations are shown here in their compressible form for Cartesian coordinates:

$$\frac{\partial \mathbf{Q}}{\partial t} + \frac{\partial \mathbf{E}}{\partial x} + \frac{\partial \mathbf{F}}{\partial y} + \frac{\partial \mathbf{G}}{\partial z} = \frac{\partial \mathbf{R}}{\partial x} + \frac{\partial \mathbf{S}}{\partial y} + \frac{\partial \mathbf{T}}{\partial z} \qquad (2.1)$$

where $\mathbf{Q}$ is the vector of conservative variables, $\mathbf{E}$, $\mathbf{F}$, and $\mathbf{G}$ are the inviscid flux vectors, and $\mathbf{R}$, $\mathbf{S}$, and $\mathbf{T}$ contain the viscous terms. These vectors are defined as

$$\mathbf{Q} = \begin{pmatrix} \rho \\ \rho u \\ \rho v \\ \rho w \\ \rho e \end{pmatrix} \tag{2.2}$$

$$\mathbf{E} = \begin{pmatrix} \rho u \\ \rho u^2 + p \\ \rho uv \\ \rho uw \\ \rho (\rho e + p) u \end{pmatrix}, \quad \mathbf{F} = \begin{pmatrix} \rho v \\ \rho vu \\ \rho v^2 + p \\ \rho vw \\ \rho (\rho e + p) v \end{pmatrix}, \quad \mathbf{G} = \begin{pmatrix} \rho w \\ \rho wu \\ \rho wv \\ \rho w^2 + p \\ \rho (\rho e + p) w \end{pmatrix} \tag{2.3}$$

$$\mathbf{R} = \begin{pmatrix} 0 \\ \tau_{xx} \\ \tau_{xy} \\ \tau_{xz} \\ Q_x \end{pmatrix}, \quad \mathbf{S} = \begin{pmatrix} \tau_{yx} \\ \tau_{yy} \\ \tau_{yz} \\ Q_y \end{pmatrix}, \quad \mathbf{T} = \begin{pmatrix} \tau_{zx} \\ \tau_{zy} \\ \tau_{zz} \\ Q_z \end{pmatrix} \tag{2.4}$$

and the heat flux terms are defined as

$$Q_x = u\tau_{xx} + v\tau_{xy} + w\tau_{xz} - q_x \tag{2.5}$$

$$Q_y = u\tau_{xy} + v\tau_{yy} + w\tau_{yz} - q_y \tag{2.6}$$

$$Q_z = u\tau_{xz} + v\tau_{yz} + w\tau_{zz} - q_z \tag{2.7}$$

where ρ is the fluid density, u, v, and w are the components of the velocity vector $\mathbf{V}$ in the x, y, and z directions respectively, p is the pressure, and e is total energy per unit mass. The velocity vector is defined as

9

$$\mathbf{V} = u\hat{\imath} + v\hat{\jmath} + w\hat{k} \tag{2.8}$$

and its magnitude is defined as

$$|\mathbf{V}| = \sqrt{u^2 + v^2 + w^2} \tag{2.9}$$

In equations 2.2, 2.3, and 2.4, the first components, when expanded, form the Continuity Equation. The second through fourth components form the x, y, and z direction Momentum Equations respectively, and the last components form the Energy Equation. The heat flux terms in the three directions q_x, q_y, and q_z, are defined as

$$q_x = -\frac{\mu}{(\gamma - 1)Pr}\frac{\partial a^2}{\partial x} \tag{2.10}$$

$$q_y = -\frac{\mu}{(\gamma - 1)Pr}\frac{\partial a^2}{\partial y} \tag{2.11}$$

$$q_z = -\frac{\mu}{(\gamma - 1)Pr}\frac{\partial a^2}{\partial z} \tag{2.12}$$

where $Pr = \frac{\nu}{\alpha}$ is the Prandtl number. The viscous stress terms are defined as

$$\tau_{xx} = \frac{2}{3}\mu\left(2\frac{\partial u}{\partial x} - \frac{\partial v}{\partial y} - \frac{\partial w}{\partial z}\right) \tag{2.13}$$

$$\tau_{yy} = \frac{2}{3}\mu\left(2\frac{\partial v}{\partial y} - \frac{\partial u}{\partial x} - \frac{\partial w}{\partial z}\right) \tag{2.14}$$

$$\tau_{zz} = \frac{2}{3}\mu\left(2\frac{\partial w}{\partial z} - \frac{\partial u}{\partial x} - \frac{\partial v}{\partial z}\right) \tag{2.15}$$

$$\tau_{xy} = \tau_{yz} = \mu\left(\frac{\partial u}{\partial y} - \frac{\partial v}{\partial x}\right) \tag{2.16}$$

$$\tau_{xz} = \tau_{zx} = \mu\left(\frac{\partial w}{\partial x} - \frac{\partial u}{\partial z}\right) \tag{2.17}$$

$$\tau_{yz} = \tau_{zy} = \mu \left(\frac{\partial v}{\partial z} - \frac{\partial w}{\partial y} \right) \tag{2.18}$$

In order to reduce numerical round-off error, it is useful to normalize the governing equations used in CFD such that the variables are on the order of 1. Normalizing, the Navier-Stokes equations become

$$\frac{\partial \bar{\mathbf{Q}}}{\partial t} + \frac{\partial \bar{\mathbf{E}}}{\partial x} + \frac{\partial \bar{\mathbf{F}}}{\partial y} + \frac{\partial \bar{\mathbf{G}}}{\partial z} = \frac{1}{Re} \left(\frac{\partial \bar{\mathbf{R}}}{\partial x} + \frac{\partial \bar{\mathbf{S}}}{\partial y} + \frac{\partial \bar{\mathbf{T}}}{\partial z} \right) \tag{2.19}$$

where the Reynolds number Re is defined as

$$Re = \frac{\rho_\infty L u_\infty}{\mu_\infty} \tag{2.20}$$

where ρ_∞, u_∞, and μ_∞ are reference density, velocity. and viscosity respectively.

Another set of equations which are needed in the CFD analysis are the state equations. The state equations used, in their normalized form are

$$\bar{p} = \frac{1}{\gamma M_\infty^2} \bar{\rho} \bar{T} \tag{2.21}$$

$$\bar{e} = \frac{\bar{T}}{\gamma(\gamma - 1)M_\infty^2} + \frac{1}{2} \left(\bar{u}^2 + \bar{v}^2 + \bar{w}^2 \right) \tag{2.22}$$

where γ is the ratio of specific heats for the fluid, T is the temperature, and M is the Mach number which is defined as

$$M = \frac{V}{a} \tag{2.23}$$

where a is the speed of sound in the medium.

2.2 Numerical Methods

2.2.1 Background

The basic concept behind CFD is the discretization of partial differential equations for the purpose of solving them numerically. In order to do so, it is necessary to discretize the spacial coordinates into small, non-infinitesimal segments. The smaller these segments are, the more accurate the solution obtained. This is accomplished by the creation of a mesh around the desired geometry.

For example, if the partial differential of the variable u with respect to x is defined as

$$\frac{\partial u}{\partial x} = \lim_{\Delta x \to \infty} \frac{u(x_0 + \Delta x) - u(x_0)}{\Delta x} \tag{2.24}$$

where Δx is used to represent a discretized section of x. In order to discretize this, a Taylor series expansion of $u(x_0 + \Delta x)$ about the point x_0 is used

$$u(x_0 + \Delta x) = u(x_0) + \frac{\partial u}{\partial x}|_{x_0}\Delta x + \frac{\partial^2 u}{\partial x^2}|_{x_0}\frac{(\Delta x)^2}{2!} + \frac{\partial^3 u}{\partial x^3}|_{x_0}\frac{(\Delta x)^3}{3!} + \cdots +$$

$$\frac{\partial^{n-1} u}{\partial x^{n-1}}|_{x_0}\frac{(\Delta x)^{n-1}}{(n-1)!} + \frac{\partial^n u}{\partial x^n}|_{\xi}\frac{(\Delta x)^n}{n!} \tag{2.25}$$

therefore

$$\frac{\partial u}{\partial x}|_{x_0} = \frac{u(x_0 + \Delta x) - u(x_0)}{\Delta x} - \frac{\partial^2 u}{\partial x^2}|_{x_0}\frac{\Delta x}{2!} - \frac{\partial^3 u}{\partial x^3}|_{x_0}\frac{(\Delta x)^2}{3!} + \cdots \tag{2.26}$$

In order to be useful as a numerical scheme, this equation must be truncated. This process introduces a truncation, or numerical error. The higher the order of the term where this truncation occurs, and therefore the higher the order of the

scheme, the lower the introduced truncation error is. It is for this reason that higher order schemes are generally preferred provided the numerical method used is robust. Truncating Equation 2.26 at the first term, and introducing the i notation

$$\frac{\partial u}{\partial x}\big|_i = \frac{u_{i+1} - u_i}{\Delta x} + TE \tag{2.27}$$

where TE is the introduced truncation error. The above is a first order forward differencing scheme. A backward differencing scheme expands $u(x_0 - \Delta x)$ while a central differencing scheme is a combination of these two methods.

2.2.2 Application to Navier-Stokes Equations

For simplicity, let us consider a special subset of the Navier-Stokes equations, the 1-D Euler equation

$$\frac{\partial \mathbf{Q}}{\partial t} + \frac{\partial \mathbf{E}}{\partial x} = 0 \tag{2.28}$$

where the conservative vector $\mathbf{Q}$ and the flux vector $\mathbf{E}$ are now defined as

$$\mathbf{Q} = \begin{pmatrix} \rho \\ \rho u \\ \rho e \end{pmatrix}, \ \mathbf{E} = \begin{pmatrix} \rho u \\ \rho u^2 + p \\ (\rho e + p)u \end{pmatrix} \tag{2.29}$$

It is now possible to determine the Jacobian $\mathbf{A}$ as

$$\mathbf{A} = \frac{\partial \mathbf{E}}{\partial \mathbf{Q}} \tag{2.30}$$

where $\mathbf{Q}$ is redefined as

$$\mathbf{Q} = \begin{pmatrix} \rho \\ m \\ n \end{pmatrix} \tag{2.31}$$

where $m = \rho u$ and $n = \rho e$.

Expressing $\mathbf{E}$ in terms of $\mathbf{Q}$

$$\mathbf{E} = \begin{pmatrix} m \\ \frac{m^2}{\rho} + (\gamma + 1)\left(n - \frac{1}{2}\frac{m^2}{\rho}\right) \\ \left[n + (\gamma - 1)\left(n - \frac{1}{2}\frac{m^2}{\rho}\right)\right]\frac{m}{\rho} \end{pmatrix} \tag{2.32}$$

$$\mathbf{A} = \begin{bmatrix} 0 & 1 & 0 \\ \frac{1}{2}(\gamma - 1)u^2 & -(\gamma - 3)u & \gamma - 1 \\ \frac{u}{\rho}(\rho e + p) + \frac{1}{2}(\gamma - 1)u^3 & \frac{1}{\rho}(\rho e + p) - (\gamma - 1)u^2 & \gamma u \end{bmatrix} \tag{2.33}$$

Because $\mathbf{E}(\mathbf{Q})$ is a homogeneous function of $\mathbf{Q}$

$$\mathbf{E} = \mathbf{A}{\cdot}\mathbf{Q} \tag{2.34}$$

the eigenvalues of $\mathbf{A}$ can be found from

$$|\mathbf{A} - \mathbf{I}\lambda| = 0 \tag{2.35}$$

$$\lambda_1 = u - a, \ \lambda_2 = u, \ \lambda_3 = u + a \tag{2.36}$$

It is interesting to note that when the problem is extended to three dimensions, the second eigenvalue u becomes repeated three times. Knowing the eigenvalues, the Jacobian $\mathbf{A}$ can be expressed as

$$\mathbf{A} = \mathbf{T}\lambda\mathbf{T}^{-1} \tag{2.37}$$

where the Eigenvector Matrix $\mathbf{T}$ is defined as

$$\mathbf{T} = \begin{bmatrix} 1 & 1 & 1 \\ u-a & u & u+a \\ h-ua & \frac{1}{2}u^2 & h+ua \end{bmatrix} \tag{2.38}$$

$$\lambda = \begin{bmatrix} u-a & 0 & 0 \\ 0 & u & 0 \\ 0 & 0 & u+a \end{bmatrix} \tag{2.39}$$

where a is the speed of sound and h is the total enthalpy

$$h = \frac{\rho e + p}{\rho} \tag{2.40}$$

2.2.3 Vector Splitting Schemes

Vector splitting schemes aim to separate the Flux vector into two parts, each corresponding to positive and negative eigenvalues. This separates the equations such that disturbance propagation upstream and downstream are calculated separately. A simple vector-splitting scheme was described by Steger and Warming [10]. Taking the case of the 1-D Euler equation, defined in Equation 2.28, and expressing it in its finite volume form, one arrives at

$$\frac{Q_i^{n+1} - Q_i^n}{\Delta t} = \frac{1}{\Delta x}\left(E_{i+\frac{1}{2}} - E_{i-\frac{1}{2}}\right) \tag{2.41}$$

utilizing Equation 2.34

$$\mathbf{E} = \left[\mathbf{T} \begin{pmatrix} u-a & & \\ & u & \\ & & u+a \end{pmatrix} \mathbf{T}^{-1} \right] \cdot \mathbf{Q}$$

$$= \left[\mathbf{T} \begin{pmatrix} 0 & & \\ & u & \\ & & u+a \end{pmatrix} \mathbf{T}^{-1} + \mathbf{T} \begin{pmatrix} u-a & & \\ & 0 & \\ & & 0 \end{pmatrix} \mathbf{T}^{-1} \right] \cdot \mathbf{Q} \qquad (2.42)$$

$$= E^+ + E^- \qquad (2.43)$$

That is, $\mathbf{E}$ has been split into $\mathbf{E}^+$ and $\mathbf{E}^-$, such that they correspond to the positive and negative eigenvalues respectively. The term $E_{i+\frac{1}{2}}$ in Equation 2.41 can thus be expressed as

$$E_{i+\frac{1}{2}} = E^+_{i+\frac{1}{2}} + E^-_{i+\frac{1}{2}} \qquad (2.44)$$

For first order accuracy $E^+_{i+\frac{1}{2}}$ is determined from upstream points as $E^+_{i+\frac{1}{2}} = E^+_i$ and $E^-_{i+\frac{1}{2}}$ is determined from downstream points as $E^-_{i+\frac{1}{2}} = E^-_{i+1}$. That is

$$E_{i+\frac{1}{2}} = E^+_i + E^-_{i+1} \qquad (2.45)$$

$$E_{i-\frac{1}{2}} = E^-_{i-1} + E^-_i \qquad (2.46)$$

and the time marching scheme can be derived from Equation 2.28 as

$$Q_i^{n+1} = Q_i^n + \frac{\Delta t}{\Delta x}(E^+_i + E^-_{i+1} - E^+_{i-1} - E^-_i) \qquad (2.47)$$

The Zha 2 E-CUSP Scheme

While splitting the Flux vector into positive and negative eigenvalue parts is useful and has been shown to produce good results, Zha introduced the idea of splitting the Flux vector into convective and acoustic terms [11, 12]. The advantage of using this method is that it is based on physical, and not mathematical principles. Whereas convective properties propagate only downstream in a fluid at subsonic speeds, acoustic properties propagate in all directions.

In the Zha scheme, Equation 2.42 is written as

$$
\mathbf{E} = \left[\mathbf{T} \begin{pmatrix} u & & \\ & u & \\ & & u \end{pmatrix} \mathbf{T}^{-1} + \mathbf{T} \begin{pmatrix} -a & & \\ & 0 & \\ & & a \end{pmatrix} \mathbf{T}^{-1} \right] \cdot \mathbf{Q}
$$

$$
= \mathbf{E^c} + \mathbf{E^p} \tag{2.48}
$$

where

$$
\mathbf{E^c} = u \begin{pmatrix} \rho \\ \rho u \\ \rho e \end{pmatrix}, \ \mathbf{E^p} = u \begin{pmatrix} 0 \\ p \\ pu \end{pmatrix} \tag{2.49}
$$

The vector $\mathbf{E^c}$ contains the eigenvalues of velocity (u, u, u), and therefore represents the convective term, whereas the vector $\mathbf{E^p}$ contains the eigenvalues of the speed of sound $(-a, 0, a)$, which is related to the propagation of pressure waves in the subsonic regime, and therefore represents the acoustic term.

The Flux at the interface $\frac{1}{2}$ can thus be written as

$$
E_{\frac{1}{2}} = \frac{1}{2} \left[(\rho u)_{\frac{1}{2}} (Q_L^c + Q_R^c) - |\rho u|_{\frac{1}{2}} (Q_R^c - Q_L^c) \right]
$$

$$+ \begin{pmatrix} 0 \\ \mathcal{P}^+ p \\ \frac{1}{2}p(u + a_{\frac{1}{2}}) \end{pmatrix}_L + \begin{pmatrix} 0 \\ \mathcal{P}^- p \\ \frac{1}{2}p(u - a_{\frac{1}{2}}) \end{pmatrix}_R \tag{2.50}$$

where $\mathcal{P}$ is defined as

$$\mathcal{P}^\pm = \frac{1}{4}(M \pm 1)^2(2 \mp M) \pm \alpha M(M^2 - 1)^2, \ \alpha = \frac{3}{16} \tag{2.51}$$

and the speed of sound at the interface $\frac{1}{2}$ is evaluated as

$$a_{\frac{1}{2}} = \frac{1}{2}(a_L + a_R) \tag{2.52}$$

$$M_L = \frac{u_L}{a_{\frac{1}{2}}}, \ M_R = \frac{u_R}{a_{\frac{1}{2}}} \tag{2.53}$$

$$\alpha_L = \frac{2(p/\rho)_L}{(p/\rho)_L + (p/\rho)_R}, \ \alpha_R = \frac{2(p/\rho)_R}{(p/\rho)_L + (p/\rho)_R} \tag{2.54}$$

The Zha3 Low Diffusion E-CUSP Scheme

Like the Zha 2 scheme, the basic idea of the Zha 3 LDE scheme is to split the inviscid flux vector into convective and pressure terms, E^c and E^p. In generalized coordinate system, the flux $\mathbf{E}$ can be split as the following

$$\mathbf{E} = E^c + E^p = \begin{pmatrix} \rho U \\ \rho u U \\ \rho v U \\ \rho w U \\ \rho e U \end{pmatrix} + \begin{pmatrix} 0 \\ l_x p \\ l_y p \\ l_z p \\ p\overline{U} \end{pmatrix} \tag{2.55}$$

where

$$\overline{U} = l_x u + l_y v + l_z w \tag{2.56}$$

The convective term, E^c is evaluated following the Edward's H-CUSP LDFSS scheme [13, 14] as,

$$E^c = \rho U \begin{pmatrix} 1 \\ u \\ v \\ w \\ e \end{pmatrix} = \rho U f^c, \quad f^c = \begin{pmatrix} 1 \\ u \\ v \\ w \\ e \end{pmatrix} \tag{2.57}$$

letting

$$C = a \left(l_x^2 + l_y^2 + l_z^2 \right)^{\frac{1}{2}} \tag{2.58}$$

where $a = \sqrt{\gamma R T}$ is used to evaluate the speed of sound. Then the convective flux at interface $\frac{1}{2}$ is evaluated as:

$$E^c_{\frac{1}{2}} = C_{\frac{1}{2}} \left[\rho_L C^+ f^c_L + \rho_R C^- f^c_R \right] \tag{2.59}$$

where, the subscripts L and R represent the left and right hand sides of the interface.

The relations borrowed from the Edward's H-CUSP LDFSS scheme [13, 14] are as follows:

$$\begin{aligned}
C_{\frac{1}{2}} &= \tfrac{1}{2} \left(C_L + C_R \right), \quad C^+ = \alpha_L^+ \left(1 + \beta_L \right) M_L - \beta_L M_L^+ - M_{\frac{1}{2}}^+ \\
C^- &= \alpha_R^- \left(1 + \beta_R \right) M_R - \beta_R M_R^- + M_{\frac{1}{2}}^- \\
M_L &= \frac{U_L}{C_{\frac{1}{2}}}, \quad M_R = \frac{U_R}{C_{\frac{1}{2}}}
\end{aligned} \tag{2.60}$$

$$\alpha_{L,R} = \tfrac{1}{2}\left[1 \pm sign\left(M_{L,R}\right)\right]$$

$$\beta_{L,R} = -max\left[0, 1 - int\left(|M_{L,R}|\right)\right]$$

$$M_{\frac{1}{2}}^+ = M_{\frac{1}{2}}\frac{C_R+C_L\Phi}{C_R+C_L}, \; M_{\frac{1}{2}}^- = M_{\frac{1}{2}}\frac{C_R+C_L\Phi^{-1}}{C_R+C_L}, \; \Phi = \frac{\left(\rho C^2\right)_R}{\left(\rho C^2\right)_L} \tag{2.61}$$

$$M_{\frac{1}{2}} = \beta_L \delta^+ M_L^- - \beta_R \delta^- M_R^+$$

$$M_{L,R}^\pm = \pm\tfrac{1}{4}\left(M_{L,R} \pm 1\right)^2$$

$$\delta^\pm = \tfrac{1}{2}\left\{1 \pm sign\left[\tfrac{1}{2}\left(M_L + M_R\right)\right]\right\}$$

The pressure flux, E^p is then evaluated as

$$E_{\frac{1}{2}}^p = \begin{pmatrix} 0 \\ \mathcal{P}^+ p\, l_x \\ \mathcal{P}^+ p\, l_y \\ \mathcal{P}^+ p\, l_z \\ \tfrac{1}{2}p\left[\overline{U} + \overline{C}_{\frac{1}{2}}\right] \end{pmatrix}_L + \begin{pmatrix} 0 \\ \mathcal{P}^- p\, l_x \\ \mathcal{P}^- p\, l_y \\ \mathcal{P}^- p\, l_z \\ \tfrac{1}{2}p\left[\overline{U} - \overline{C}_{\frac{1}{2}}\right] \end{pmatrix}_R \tag{2.62}$$

The contravariant speed of sound $\overline{C}$ in the pressure vector is consistent with $\overline{U}$ and is calculated as:

$$\overline{C} = C - l_t \tag{2.63}$$

The use of $\overline{U}$ and $\overline{C}$ instead of U and C in the pressure vector is to take into account the grid speed so that the flux will transit from subsonic to supersonic smoothly. When the grid is stationary, $l_t = 0$, $\overline{C} = C$, $\overline{U} = U$.

The pressure splitting coefficient borrowed from Van Leer [15] is used:

$$\mathcal{P}_{L,R}^\pm = \frac{1}{4}\left(M_{L,R} \pm 1\right)^2 \left(2 \mp M_L\right) \tag{2.64}$$

2.2.4 The Roe Scheme

Roe developed an approximate Riemann solver which can be expressed in one formulation for both subsonic and supersonic flows [16]. Flux at the $\frac{1}{2}$ interface can be calculated as follows

$$E_{\frac{1}{2}} = \frac{1}{2} \left[E_L + E_R + \tilde{T} |\tilde{\Lambda}| \tilde{T}^{-1} \left(Q_L - Q_R \right) \right] \tag{2.65}$$

where $\tilde{T}$ is the eigenvalue matrix using Roe's averages

$$\tilde{T} = \begin{bmatrix} 1 & 1 & 1 \\ \tilde{u} - \tilde{a} & \tilde{u} & \tilde{u} + \tilde{a} \\ \tilde{h} - \tilde{u}\tilde{a} & \frac{\tilde{u}^2}{2} & \tilde{h} + \tilde{u}\tilde{a} \end{bmatrix} \tag{2.66}$$

where $\tilde{h}$ is the Roe-averaged total enthalpy and $|\tilde{\Lambda}|$ is defied as

$$|\tilde{\Lambda}| = \begin{bmatrix} |\tilde{u} - \tilde{a}| & 0 & 0 \\ 0 & |\tilde{u}| & 0 \\ 0 & 0 & |\tilde{u} - \tilde{a}| \end{bmatrix} \tag{2.67}$$

Roe's averages are evaluated as

$$\tilde{u} = \frac{\sqrt{\rho_L} u_L + \sqrt{\rho_R} u_R}{\sqrt{\rho_L} + \sqrt{\rho_R}} \tag{2.68}$$

$$\tilde{h} = \frac{\sqrt{\rho_L} h_L + \sqrt{\rho_R} h_R}{\sqrt{\rho_L} + \sqrt{\rho_R}} \tag{2.69}$$

$$\tilde{a} = (\gamma - 1) \left(\tilde{h} - \frac{1}{2} \tilde{u}^2 \right) \tag{2.70}$$

2.3 Turbulence Modeling

In order to accurately resolve fluid flow problems, it is necessary to model the effects of turbulence. Because turbulence is a physical problem characterized highly chaotic effects, no general solution is available. In order to include its effect into the solving of the Navier-Stokes equations, it is necessary to make use of approximate models. Many turbulence models are available, such as algebraic, one-equation, two-equation, Large Eddy Simulation (LES), Detached Eddy Simulation (DES), or Direct Numerical Simulation (DNS) models. The present work makes use of the FASIP package's ability to implement both the algebraic Baldwin-Lomax, and the S-A one-equation models.

2.3.1 The Baldwin-Lomax Model

The Baldwin-Lomax model is an algebraic 0-equation model and is the simplest turbulence model employed by the FASIP package. The B-L model is a two layered model and was introduced in 1978 [17]. Due to its simplicity, it is capable of high CPU efficiency, however, it is not suitable with cases where there is a large degree of fluid separation.

The B-L model consists on an inner layer

$$\mu_{t,i} = \rho l^2 \left| \omega \right| \tag{2.71}$$

where the mixing length l is determined by

$$l = ky \left[1 - \exp \left(-\frac{y^+}{A^+} \right) \right] \tag{2.72}$$

The variable ω represents the vorticity, y is the dimensional distance to the wall and y^+ is the dimensionless distance to the wall.

The outer layer is defined as

$$\mu_{t,o} = K C_{cp} \rho F_{wake} F_{kleb} \tag{2.73}$$

$$F_{wake} = \min \left(y_{\max} F_{\max}, \; C_{wake} y_{\max} u_{diff}^2 / F_{\max} \right) \tag{2.74}$$

$$F_{kleb} = \left[1 + 5.5 \left(\frac{C_{kleb} y}{y_{\max}} \right)^6 \right]^{-1} \tag{2.75}$$

where the values of the constants used are $k = 0.4$, $A^+ = 26$, $C_{wake} = 0.25$, $C_{kleb} = 0.3$, $C_{cp} = 1.6$, and $K = 0.0168$.

u_{diff}, $F_{\max}$ and $y_{\max}$ are determined by the velocity profile following a line normal to the wall. $F_{\max}$ and $y_{\max}$ are the maximum value and the corresponding distance of function F_y, which is defined as

$$F_y = y \, |\omega| \left[1 - \exp \left(-\frac{y^+}{A^+} \right) \right] \tag{2.76}$$

$$u_{\text{diff}} = \left(\sqrt{u^2 + v^2 + w^2} \right)_{\max} - \left(\sqrt{u^2 + v^2 + w^2} \right)_{\min} \tag{2.77}$$

μ_t is the eddy viscosity which is determined by location as

$$\mu_t = \min \left(\mu_{t,i}, \; \mu_{t,o} \right) \tag{2.78}$$

2.3.2 The Spalart-Allmaras One-Equation Model

Spalart and Allmaras proposed a one-equation turbulence model as a more accurate alternative to the Baldwin-Lomax algebraic model [18]. The FASIP package makes use of the S-A one-equation model for higher order calculations. In order to apply the S-A model to the Zha CUSP scheme, the governing Reynolds Averaged Navier Stokes (RANS) equations which are shown in Equation 2.19 can be re-written in the

generalized coordinates as follows:

$$\frac{\partial \bar{\mathbf{Q}}}{\partial t} + \frac{\partial \bar{\mathbf{E}}}{\partial \xi} + \frac{\partial \bar{\mathbf{F}}}{\partial \eta} + \frac{\partial \bar{\mathbf{G}}}{\partial \zeta} = \frac{1}{Re}\left(\frac{\partial \bar{\mathbf{R}}}{\partial \xi} + \frac{\partial \bar{\mathbf{S}}}{\partial \eta} + \frac{\partial \bar{\mathbf{T}}}{\partial \zeta} + \mathbf{D}\right) \tag{2.79}$$

where the conservative, flux, and viscous term vectors are defined as

$$\mathbf{Q} = \begin{pmatrix} \rho \\ \rho u \\ \rho v \\ \rho w \\ \rho e \\ \rho \tilde{\nu} \end{pmatrix} \tag{2.80}$$

$$\mathbf{E} = \begin{pmatrix} \rho U \\ \rho u U + l_x p \\ \rho v U + l_y p \\ \rho w U + l_z p \\ \rho\left(\rho e + p\right) U - l_t p \\ \rho \tilde{\nu} U \end{pmatrix}, \ \mathbf{F} = \begin{pmatrix} \rho V \\ \rho u V + m_x p \\ \rho v V + m_y p \\ \rho w V + m_z p \\ \rho\left(\rho e + p\right) V - m_t p \\ \rho \tilde{\nu} V \end{pmatrix}, \ \mathbf{G} = \begin{pmatrix} \rho W \\ \rho u W + n_x p \\ \rho v W + n_y p \\ \rho w W + n_z p \\ \rho\left(\rho e + p\right) W - n_t p \\ \rho \tilde{\nu} W \end{pmatrix}$$
$$\tag{2.81}$$

$$\mathbf{R} = \begin{pmatrix} 0 \\ l_k \tau_{xk} \\ l_k \tau_{yk} \\ l_k \tau_{zk} \\ l_k \beta_k \\ \frac{\rho}{\sigma}(\nu + \tilde{\nu})(\mathbf{l} \bullet \nabla\tilde{\nu}) \end{pmatrix}, \ \mathbf{S} = \begin{pmatrix} 0 \\ m_k \tau_{xk} \\ m_k \tau_{yk} \\ m_k \tau_{zk} \\ m_k \beta_k \\ \frac{\rho}{\sigma}(\nu + \tilde{\nu})(\mathbf{m} \bullet \nabla\tilde{\nu}) \end{pmatrix}, \ \mathbf{T} = \begin{pmatrix} 0 \\ n_k \tau_{xk} \\ n_k \tau_{yk} \\ n_k \tau_{zk} \\ n_k \beta_k \\ \frac{\rho}{\sigma}(\nu + \tilde{\nu})(\mathbf{n} \bullet \nabla\tilde{\nu}) \end{pmatrix},$$
$$\tag{2.82}$$

$$\mathbf{D} = \begin{pmatrix} 0 \\ 0 \\ 0 \\ 0 \\ 0 \\ S_\nu \end{pmatrix} \tag{2.83}$$

where the matrix $\mathbf{D}$ has been added as a coupling of the RANS equation with the S-A one-equation model. In the above, the variables β_k and S_ν are defined as

$$\beta_k = u_i \tau_{ki} - q_k \tag{2.84}$$

$$S_\nu = \rho C_{b1} \left(1 - f_{t2}\right) \tilde{S} \tilde{\nu} + \frac{1}{Re} \left[-\rho \left(C_{w1} f_w - \frac{C_{b1}}{\kappa^2} f_{t2} \right) \left(\frac{\tilde{\nu}}{d}\right)^2 \right.$$
$$\left. + \frac{\rho}{\sigma} C_{b2} \left(\nabla \tilde{\nu}\right)^2 - \frac{1}{\sigma} \left(\nu + \tilde{\nu}\right) \nabla \tilde{\nu} \bullet \nabla \rho \right] + Re \left[\rho f_{t1} \left(\Delta U\right)^2 \right] \tag{2.85}$$

In the above, $\tilde{\nu}$ is an intermediate variable related to the eddy viscosity ν_t by the relation

$$\nu_t = \tilde{\nu} f_{v1}, \ \ f_{v1} = \frac{\chi^3}{\chi^3 + c_{v1}^3}, \ \ \chi = \frac{\tilde{\nu}}{\nu} \tag{2.86}$$

while the variables U, V, and W are the contravariant velocities in the direction of the generalized coordinates, and are defined based on the normal vectors $\mathbf{l}$, $\mathbf{m}$, and $\mathbf{n}$ as

$$U = l_t + \mathbf{l} \bullet \mathbf{V}$$

$$U = m_t + \mathbf{m} \bullet \mathbf{V} \tag{2.87}$$

$$U = n_t + \mathbf{n} \bullet \mathbf{V}$$

l_t, m_t, and n_t are the moving grid velocities, which for the present work are equal to

zero.

Functions used in the S-A model are given by

$$\tilde{S} = S + \frac{\tilde{\nu}}{Re\kappa^2 d^2} f_{v2}, \ f_{v2} = 1 - \frac{\chi}{1+\chi f_{v1}}$$

$$f_w = g \left[\frac{1+C_{w3}^6}{g^6 + C_{w3}^6} \right]^{\frac{1}{6}}, \ g = r + C_{w2}\left(r^6 - r\right), \ r = \frac{\tilde{\nu}}{Re\tilde{S}\kappa^2 d^2}$$

$$f_{t1} = C_{t1} g_t exp \left[-C_{t2} \frac{\omega_t^2}{\Delta U^2} \left(d^2 + g_t^2 d_t^2 \right) \right], \ g_t = min\left(0.1, \frac{\Delta U}{\omega_t \Delta x_t} \right)$$

$$f_{t2} = C_{t3} exp\left(-C_{t4} \chi^2 \right)$$

where the magnitude of the vorticity S is defined as

$$S = \sqrt{\left(\frac{\partial w}{\partial y} - \frac{\partial v}{\partial z} \right)^2 + \left(\frac{\partial u}{\partial z} - \frac{\partial w}{\partial x} \right)^2 + \left(\frac{\partial v}{\partial x} - \frac{\partial u}{\partial y} \right)^2} \qquad (2.88)$$

and d is the distance to the nearest surface.

The constants used in this model are given as

$$\sigma = \tfrac{2}{3}, \ C_{b1} = 0.1355, \ C_{b2} = 0.622, \ \kappa = 0.41, \ C_{v1} = 7.1,$$

$$C_{w1} = C_{b1}/\kappa^2 + \left(1 + C_{b2}\right)/\sigma, \ C_{w2} = 0.3, \ C_{w3} = 2,$$

$$C_{t1} = 1, \ C_{t2} = 2, \ C_{t3} = 1.2, \ C_{t4} = 0.5$$

2.3.3 Detached Eddy Simulation (DES)

The FASIP package is also capable of using a detached-eddy simulation model the E-CUSP scheme with fifth-order WENO scheme as an advancement of the RANS model. DES is a hybrid technique between the RANS model, and the Large Eddy Simulation (LES) model. Its main concept is to treat the regions of the flow which are near to a wall with a RANS-like model, while dealing with the rest of the flow with a LES-like model. This is done by modifying the distance function d as

$$\tilde{d} = min(d, C_{DES}\Delta) \qquad (2.89)$$

where Δ is the largest spacing of the grid cell and the constant $C_{DES} = 0.65$ is used.

The governing equations for the DES model are the spatially filtered 3D general Navier-Stokes equations in generalized coordinates, and are expressed as

$$\frac{\partial \mathbf{Q}'}{\partial t} + \frac{\partial \mathbf{E}'}{\partial \xi} + \frac{\partial \mathbf{F}'}{\partial \eta} + \frac{\partial \mathbf{G}'}{\partial \zeta} = \frac{1}{Re}\left(\frac{\partial \mathbf{E}'_{\mathbf{v}}}{\partial \xi} + \frac{\partial \mathbf{F}'_{\mathbf{v}}}{\partial \eta} + \frac{\partial \mathbf{G}'_{\mathbf{v}}}{\partial \zeta}\right) \tag{2.90}$$

where the conservative variable vector $\mathbf{Q}'$, and the flux vectors $\mathbf{E}'$, $\mathbf{F}'$, and $\mathbf{G}'$ are given as

$$\mathbf{Q}' = \frac{\mathbf{Q}}{J} \tag{2.91}$$

$$\mathbf{E}' = \frac{1}{J}(\xi_t \mathbf{Q} + \xi_x \mathbf{E} + \xi_y \mathbf{F} + \xi_z \mathbf{G}) \tag{2.92}$$

$$\mathbf{F}' = \frac{1}{J}(\eta_t \mathbf{Q} + \eta_x \mathbf{E} + \eta_y \mathbf{F} + \eta_z \mathbf{G}) \tag{2.93}$$

$$\mathbf{G}' = \frac{1}{J}(\zeta_t \mathbf{Q} + \zeta_x \mathbf{E} + \zeta_y \mathbf{F} + \zeta_z \mathbf{G}) \tag{2.94}$$

$$\mathbf{E}'_{\mathbf{v}} = \frac{1}{J}(\xi_x \mathbf{E}_{\mathbf{v}} + \xi_y \mathbf{F}_{\mathbf{v}} + \xi_z \mathbf{G}_{\mathbf{v}}) \tag{2.95}$$

$$\mathbf{F}'_{\mathbf{v}} = \frac{1}{J}(\eta_x \mathbf{E}_{\mathbf{v}} + \eta_y \mathbf{F}_{\mathbf{v}} + \eta_z \mathbf{G}_{\mathbf{v}}) \tag{2.96}$$

$$\mathbf{G}'_{\mathbf{v}} = \frac{1}{J}(\zeta_x \mathbf{E}_{\mathbf{v}} + \zeta_y \mathbf{F}_{\mathbf{v}} + \zeta_z \mathbf{G}_{\mathbf{v}}) \tag{2.97}$$

Spalart et al. [19] suggest the closure of the equations as follows

$$\frac{\partial \rho\tilde{\nu}}{\partial t} + \frac{\partial \rho\tilde{\nu}U}{\partial \xi} + \frac{\partial \rho\tilde{\nu}V}{\partial \eta} + \frac{\partial \rho\tilde{\nu}W}{\partial \zeta} = \frac{1}{Re}\left(\frac{\partial \frac{\rho}{\sigma}\left(\nu + \tilde{\nu}\right)\left(\mathbf{l} \bullet \nabla\tilde{\nu}\right)}{\partial \xi}\right.$$

$$+\frac{\partial \frac{\rho}{\sigma}\left(\nu+\tilde{\nu}\right)\left(\mathbf{m} \bullet \nabla \tilde{\nu}\right)}{\partial \eta}+\frac{\partial \frac{\rho}{\sigma}\left(\nu+\tilde{\nu}\right)\left(\mathbf{n} \bullet \nabla \tilde{\nu}\right)}{\partial \zeta}+S_{\nu}\Bigg) \qquad (2.98)$$

where

$$\begin{aligned} S_{\nu}=\rho C_{b1}\left(1-f_{t2}\right)\tilde{S}\tilde{\nu}+\tfrac{1}{Re}\bigg[-\rho\left(C_{w1}f_{w}-\tfrac{C_{b1}}{\kappa^{2}}f_{t2}\right)\left(\tfrac{\tilde{\nu}}{d}\right)^{2} \\ +\tfrac{\rho}{\sigma}C_{b2}\left(\nabla\tilde{\nu}\right)^{2}-\tfrac{1}{\sigma}\left(\nu+\tilde{\nu}\right)\nabla\tilde{\nu}\bullet\nabla\rho\bigg]+Re\left[\rho f_{t1}\left(\Delta U\right)^{2}\right] \end{aligned} \qquad (2.99)$$

The variable $\tilde{\nu}$ is the same as in the S-A model, and is used to determine the filtered sub-grid scale (SGS) stress terms. $\tilde{\nu}$ can be obtained from the relation

$$\mu_{sgs}=\rho\tilde{\nu}f_{v1} \qquad (2.100)$$

Chapter 3

Methodology For Use of the FASIP CFD Package

A thorough methodology is developed and presented here for the preparation and use of the Fluid-Acoustics-Structure Interaction Package (FASIP). This includes mesh generation, preparation of all the files needed to run the code, as well as defining of the boundary conditions and other specific information needed to fully define a case.

3.1   Mesh Generation

During the process of mesh generation for any geometry with for CFD simulation, there exist two separate domains. The first is the physical domain, which contains the physical geometric information about the mesh. This domain is defined within the Cartesian coordinate system (x, y, z). The second is the computational domain, within which the CFD code solves the governing equations. This domain is defined within the generalized curvilinear (ξ, η, ζ) coordinate system. The physical domain must be transformed into the computational domain in order to run the CFD code. This transformation can be achieved for any simply connected domain by stretching and deforming it into a rectangular (or cubic in the case of 3-D geometries) shape. Therefore, the gridlines around a body of arbitrary shape can be defined with the generalized curvilinear index system (ξ, η, ζ). Upon transformation, this curvilinear system becomes the Cartesian computational domain. Any doubly connected domain

can be transformed into a simply-connected one by introducing a suitable branch-cut. This can be circumvented by creating multiple domains, which is possible with the use of the MPI system. It can then be transformed into a computational domain. Grid generation is done within the physical domain, and the CFD code then transforms this into the computation domain.

For grid generation, the Gridgen software software is used. Gridgen is a widely-used commercial tool for structured grid generation for CFD. In order to create a grid around a given geometry, it must first be designed through the use of any CAD program. The CAD file must then be transfered to an IGES format, which is then imported into Gridgen, where the process of generating a mesh can begin.

Gridgen uses a progressive method to generate a mesh. One begins by creating 1-D connectors, followed by 2-D domains, and finally 3-D blocks. The latter cannot be created until the former are fully defined. Gridgen has the capability of creating both unstructured and structured meshes, that is, meshes with either rectangular or triangular elements. However, the present work only makes use of structured meshes, which are supported by FASIP. Gridgen also allows the user to define the distribution of the points within a connector, allowing for a higher density of elements in areas where higher resolution is needed. For example, the highest distribution of points is usually given near physical walls where a thin boundary layer will be present in the flow.

The following steps should be followed when using Gridgen to generate a three-dimensional mesh:

1. Create the desired geometry in a CAD program

2. Export the geometry as an IGES file

3. Import the IGES file containing geometric data into Gridgen

4. Under the "Database" section, delete all unnecessary construction lines from the IGES file

5. Under the "Connectors" section, select the "Create Connectors" function to create connectors "On Database Entries"

6. Clean up created connectors by joining those which are unnecessarily separated, adding or removing connectors as necessary

7. One-by-one, use the "Modify" function on connectors and redefine them by giving them a dimension (number of points), and giving the created points a suitable distribution

8. Use the "Create Domains" function to create domains on all surfaces, far-fields, interfaces and other sections requiring a boundary condition to be defined. Take care to define domains such that they are all mutually consistent in the orientation of their local coordinate systems where possible

9. Use the "Create Blocks" function to create blocks using the previously created domains as boundaries

10. Use the "Redefine ξ, η, and ζ" function to select the appropriate coordinate system orientation for all blocks such that they are right-handed and coincident to each other

11. If necessary, run the "Structured Solver" on blocks until grid lines are mostly orthogonal to each other

The mesh can then be saved into a data file using the unformatted PLOT3D format with double precision, which can then be read by the CFD code.

3.2 Preparation of FASIP Code For Use

The CFD code utilized to run the simulation in this thesis is the in-house code for the University of Miami College of Engineering CFD Laboratory, which is headed by Dr. Ge-Cheng Zha [12, 20–23]. This code, named Fluid-Acoustics-Structure Interaction Package is under constant development and testing, and includes a wide range of CFD schemes at a variety of orders of accuracy. The cases studied herein make use primarily of the Roe and Zha schemes. The FASIP code makes use of Message Parsing Interface (MPI) in order to split the CFD computation over several CPUs. This method allows for much greater efficiency due to faster computation times. Generally, each block within the mesh is assigned to a single CPU, and the MPI attends to the constant communication between the different CPUs.

All running of the code occurs within a Linux Operating System environment. The code consists of the following executable and input files:

1. **Executable Files**

    - *main.out* - the main FASIP CFD code

    - *init.out* - the initializing program which prepares the case with its mesh, initial flow field, inputs, and boundary conditions for simulation

    - *plot3d2rans* - translates the Plot3D format mesh obtained from Gridgen into a format readable by the FASIP code

    - *post_proc* - post processing code which calculates lift and drag coefficients, as well as outputs *.plt* files readable by Tecplot for visualization

    - *flowrate* - additional post processing code which calculates CFJ flowrates and jet effects

2. **Input Files**

- *datain* - main input file read by *init.out* containing flow parameters, computational options, and boundary conditions

- *init.input* - secondary input file read by *init.out* containing mesh size data and inlet and additional injection nd suction parameters for the CFJ case

- *geo.grd* - the grid file in Plot3D format generated by Gridgen

- *nodes.txt* - a list of cluster nodes to be used in the computation by the MPI

Once all of these files are contained within the same directory, preparation of any case for CFD simulation is accomplished by the following steps:

1. Prepare a mesh using Gridgen or any similar grid-generating software. Make sure that blocks are ordered in the manner specified within the boundary conditions by the `block` statement [20]

2. Import the *.grd* Plot3D file into the appropriate directory and save it to *geo.grd*

3. Run the *plot3d2rans* code, which generates a series of *.plt* files for each block

4. Edit the *datain* file with the correct flow parameters

5. Edit the *datain* file with the desired computational parameters

6. Edit the *datain* file with the correct boundary conditions

7. Edit the *init.input* file with the correct mesh size information, and additional CFJ injection and suction parameters if necessary. Note that the number of cells in a block and not the number of points should be used

8. Run the *init.out* code to generate the initial solutions. This created the a series or *rstart* files for each block

9. Run the *main.out* code using mpi for parallel computation by using the following syntax:

```
$ mpirun -np n -machinefile nodes.txt main.out > hist.dat &
```

where n is the number of blocks. The convergence history will be output to the file *hist.dat*. Results will be saved in the *rstore* files

The *main.out* code outputs averaged and maximum L2 norm residuals on screen. These values are visually monitored for convergence and errors. Iteration of the above is necessary while manipulating numerical parameters such as the CFL number. Once the desired convergence has been achieved, the post processing codes can be run and results prepared for visualization.

3.3   Defining Boundary Conditions

The FASIP code uses a boundary condition definition system developed by Wang [20]. A sample boundary condition is given below:

```
&bcdef bcdir='xie',block=1,bctype=3,start=1,1,1,end=1,20,1/
```

The boundary condition is declared by the use of the `&bcdef` statement, and finalized by the use of a backslash `/`. The direction of the boundary condition is defined by the `bcdir` statement. Boundary conditions are defined by the direction normal to the boundary. These directions are given within the local (ξ, η, ζ) coordinate system, and are named `xie`, `eta`, and `zta` respectively. The block wherein the boundary condition is defined is given in the statement `block`. Boundary condition type is given by `bctype`. A list of boundary conditions is given in Table 3.1.

Boundary condition mapping is achieved by the use of a procedure developed by Wang et. al. [20]. Any one, two, or three dimensional boundary can be defined uniquely by the indices of two diagonal points. This is done with the use of the `start` and `end` statements. Figure **??** shows the manner in which blocks, faces, and edges are

BC	BC type
1	zero gradient
2	supersonic inflow
3	no-slip wall boundary
4	zero gradient with $w = 0$
5	subsonic outlet, p_{static} fixed by user (for internal flow or injection)
6	subsonic inflow, ρ and V at inlet fixed from initial flowfield (for far-field)
7	interface boundary between blocks for mpi
8	symmetry boundary
9	subsonic inlet, p_{total} and T_{total} fixed by user (for internal flow or suction)
10	periodic boundary condition (used with same-block interface)
11	subsonic outflow, fixed static pressure (for far-field)
19	isothermal wall, zero-gradient pressure
20	periodic boundary for flow variables only (used with 3D cases)

Table 3.1: Boundary condition numbers and corresponding definitions used in *datain*

ordered for boundary condition definitions. From this figure, the diagonal points used to define the right face of the given block would be `start=n1,1,1,end=n1,n2,n3`.
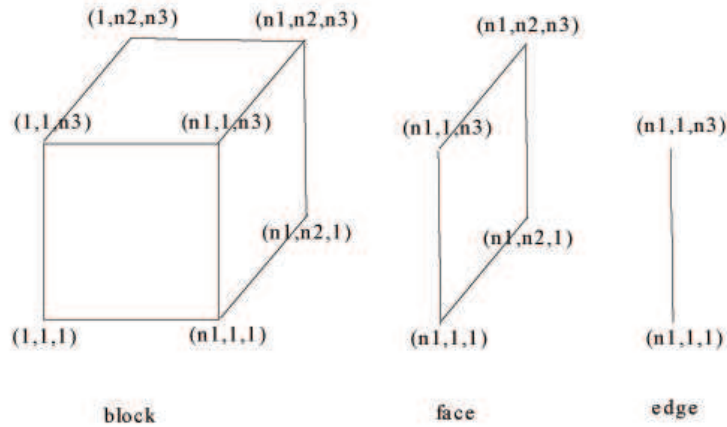

Figure 3.1: Block, face, and edge ordering for boundary condition definition

3.3.1   The Inner Boundary for MPI

In the case of an interface boundary between adjacent blocks where no physical boundary exists, that is, a boundary that exists only for MPI, then additional information must be given to fully define the boundary condition [20]. Figure 3.2 illustrates the manner in which the inner boundary for MPI is defined for two arbitrary three dimensional blocks labeled p and q.
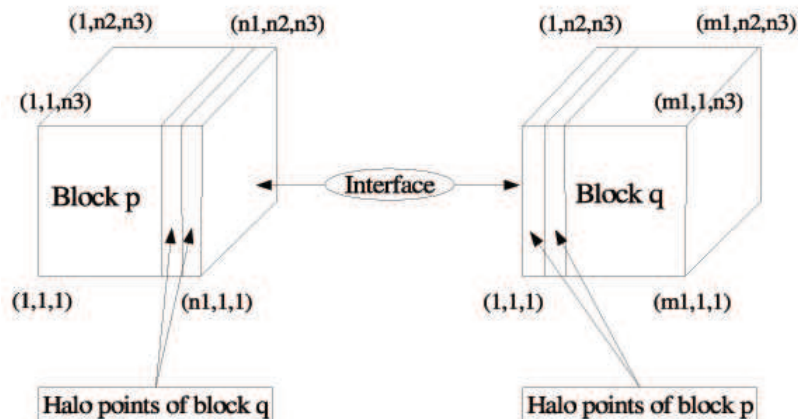

Figure 3.2: Setup for inner boundary for MPI boundary condition in three dimensions

An example of such a case can be seen below:

```
&bcdef bcdir='xie',block=1,bctype=7,start=1,1,1,end=1,20,1,
iblock=2,istart=20,1,1,iend=20,20,1,order=1,2,3/
```

The interface boundary condition is defined by `bctype=7`. The first line defined the interface boundary from the perspective of block 1, however, we must also define this boundary from block 2. This definition is given in line 2. The interfacing block is given by `iblock`, and the indices of the starting and ending points in block 2 are given by `istart` and `iend`. It is very important to note that the points `start` and `istart` *must* coincide. The same is true for the points `end` and `iend`. For example,

from Figure 3.2, if the interface is defines in block p as `start=n1,1,1,end=n1,n2,n3`, then in block q it *must* be defined as `istart=1,1,1,iend=1,n2,n3`.

There may occur a case where the coordinate system directions do not coincide between adjacent blocks. In order to allow for this case, the `order` statement is introduced. In the above example, if the order of block 1 were (ξ, η, ζ), but block 2 were ordered (η, ξ, ζ), then the order would be `order=2,1,3`. If the coordinate system directions coincide between adjacent blocks, then the `order` statement may be omitted. Figure 3.3 gives a list of the order definition as it must be given for all possible coordinate system directions of the adjacent block.
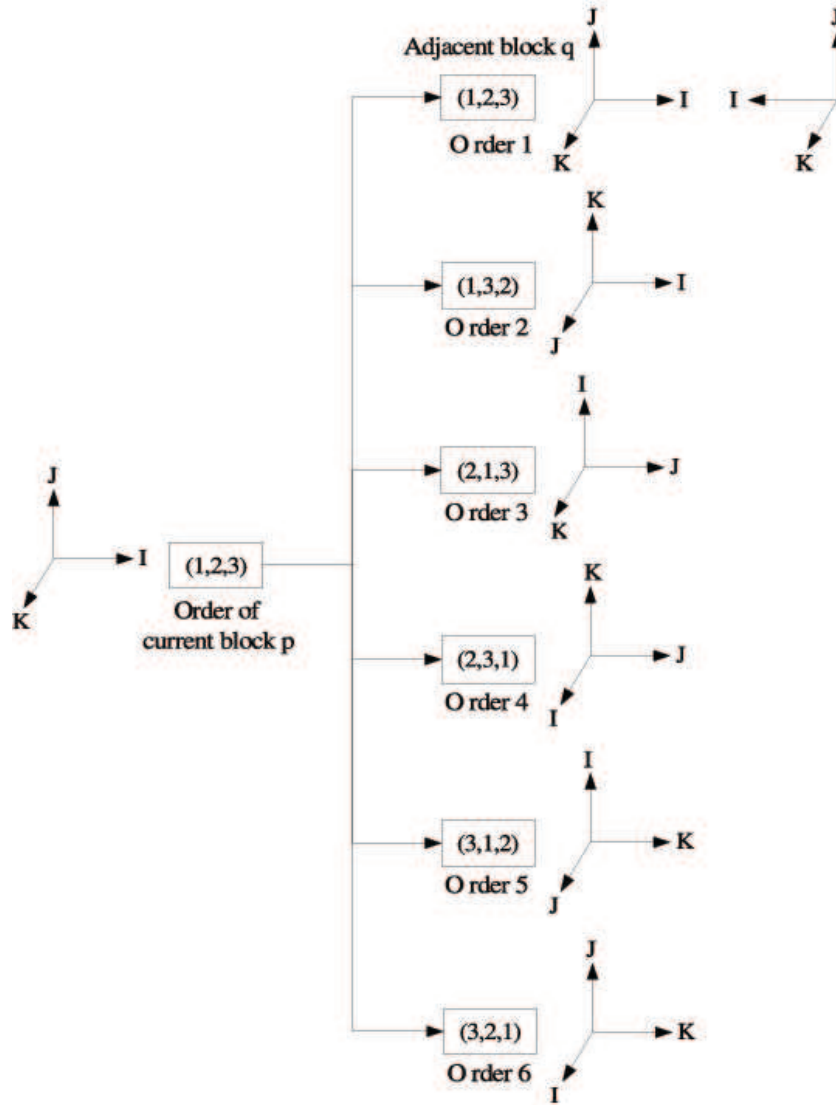
Figure 3.3: Order definitions for interface boundary

Chapter 4

Co Flow Jet Flying Wing CFD Simulation

4.1 Co-Flow Jet Airfoil Concept

The Co-Flow Jet (CFJ) Airfoil concept was introduced by Zha [6–9, 24] as a means of improving the performance of nearly any airfoil cross-section. In its basic concept, it introduces a high-energy jet of recirculated air into the laminar boundary layer on the suction surface of the airfoil, therefore increasing its turbulence and promoting attached flow even in adverse conditions. Due to increased circulation, the CFJ airfoil has been shown to increase lift and reduce drag significantly, as well as to increase the stall margin, that is, the angle of attack at which flow detaches.

In the CFJ concept, an injection slot near leading edge and a suction slot near trailing edge on the airfoil suction surface are introduced onto the baseline airfoil as sketched in Fig.4.4. A high energy jet of air is then injected near the leading edge in the same direction of the main flow and the same amount of mass flow is sucked near trailing edge. The jet is thus recirculated and maintained at a zero net mass-flux flow control. The fundamental mechanism which drives the CFJ concept is that the severe adverse pressure gradient on the suction surface strongly augments the turbulent shear layer mixing between the main flow and the jet [25]. This mixing then induces a lateral transport of energy from the jet to the main flow and allows the now energized main

flow to overcome the large adverse pressure gradient and remain attached even at high angles of attack. The stall margin is hence significantly increased. At the same time, the high momentum jet drastically increases the circulation, which significantly augments lift, reduces drag or even generates thrust (net negative drag), much like a bird wing does. Fig.4.2 shows a typical comparison where the baseline airfoil has a massive flow separation at high angle of attack, whereas the CFJ airfoil has a very well attached flow [6, 7]. To most effectively make use of the adverse pressure gradient to enhance mixing, the injection slot is designed to be located downstream of the leading edge suction peak.
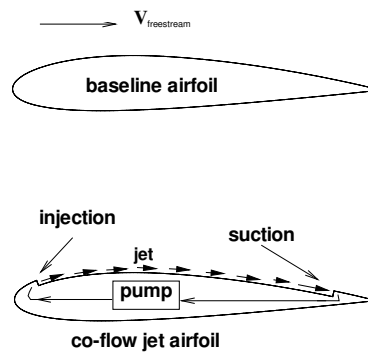

Figure 4.1: Baseline NACA2415 and CFJ2415 Airfoil

In [6, 7, 24], an overview of different flow control methods is given. Compared with the circulation control (CC) airfoil, the working mechanism of CFJ airfoil is different. A CC airfoil relies on a large leading edge (LE) or trailing edge (TE) to have the Coandă effect and enhance circulation. The large TE or LE, however, may generate a large drag penalty during cruise. The CFJ airfoil relies on the jet mixing to energize the main flow and overcome the adverse pressure gradient so that the flow can induce high circulation and remain attached at high AoA. The CC airfoil dumps away the jet mass flow, which is a considerable penalty to the propulsion system. The CFJ airfoil, on the other hand, recirculates the jet mass flow and achieves the
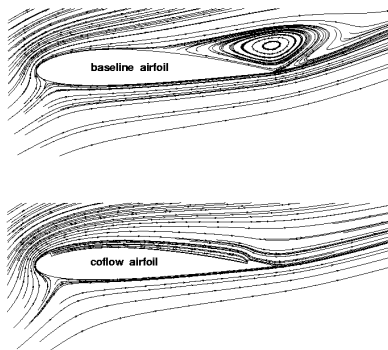
Figure 4.2: Flow field for the baseline NACA2415 and CFJ2415 Airfoil at a high angle of attack

zero net jet mass flux to have very low energy expenditure. Flow control has also been attempted with the use of acoustic waves or plasma jets. Compared with this synthetic jet flow control, the enhancement of airfoil performance by the CFJ airfoil is much more drastic because the interaction of the main flow with the synthetic jet generated either by acoustic waves or plasma is generally too weak.

The CFJ airfoil simultaneously achieves three radical improvements at low energy expenditure: lift enhancement, stall margin increase, and drag reduction or thrust generation. No other flow control methods enhance the airfoil performance as drastically as the co-flow jet airfoil [6, 7, 26–28].

In [9], the control volume analysis indicates that the drag or thrust of a CFJ airfoil measured in the wind tunnel is the actual force acting on the airfoil or aircraft system in the stream-wise direction. This is not the same as the CC airfoil, which must consider the equivalent drag due to the suction penalty from the free-stream. For a CC airfoil, the equivalent drag is significantly larger than the drag measured in a wind tunnel and is also substantially larger than the drag of a CFJ airfoil. For a CFJ airfoil, the suction penalty is already included in the measured drag and is off set by the higher circulation and stronger leading edge suction induced by the CFJ [9, 29]. The drag reduction mechanism of a CFJ airfoil is not based on the

conventional concept to reduce the skin friction. Instead, it relies on the help of the pressure resultant force, which overwhelms the skin friction. When the leading edge suction is very strong, the low pressure at leading edge results in a resultant force that is forward-pointing and is greater than the skin friction. Thus a thrust is produced. When a thrust is generated by the wing, the conventional engines may not needed.

4.2   Flying Wing Airframe Design

Unlike most conventional aircraft, where the wings and fuselage are separate structures, the CFJ Aircraft will make use of a Flying Wing airframe where both of these components are incorporated into a single, blended body as shown in Figure 4.3. Because the fuselage has the same airfoil cross section as the wings, it acts as an extension of the same and thus produces additional lift. This feature also allows for an increased coverage area for the CFJ device, therefore increasing the benefits gained from using it. The planform of the aircraft was chosen such that the desired aspect ratio of about $AR = 4$ was achieved, while allowing the fuselage section to be thicker than the wings for storage and payload purposes, and still having the same airfoil cross-section. The wings are not highly swept, because the target mission for this study would not near sonic speeds.
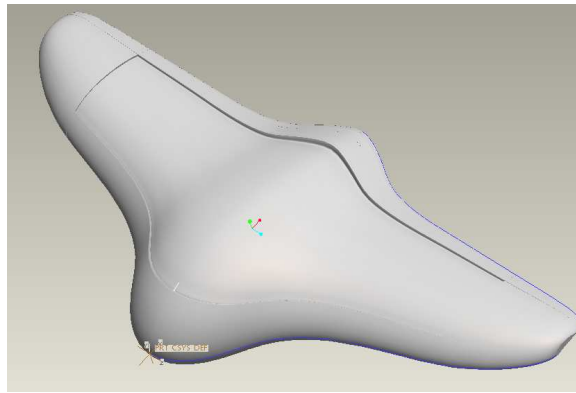

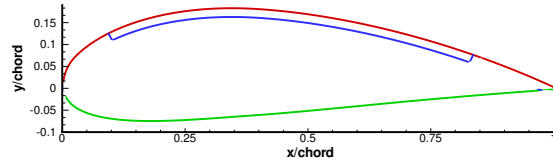Figure 4.3: CFJ Aircraft concept using Flying Wing and CFJ Airfoil

Figure 4.4: CFJ 6425 airfoil configuration

A flying wing design also allows for a reduction in the wingspan of the aircraft. Because the fuselage surface is no longer "wasted", but instead made to produce lift, the aircraft can produce more lift with a shorter wingspan.

The baseline airfoil chosen for this study is the NACA 6425 airfoil, which can be seen in Figure 4.4. This airfoil has a camber of 6% located 40% from the leading edge, with a maximum thickness of 25% of the chord. This airfoil was chosen for its moderate camber and high thickness. The high thickeness would allow for comfortable placement of all of the CFJ components, such as the pump and ducting. Also, airfoils with high thicknesses will produce higher lift as long as the air flow remains attached. Conventional aircraft shy away from thicknesses higher than 15% due to the increased risk of flow separation. However, with the use of the CFJ device, a higher thickness airfoil can be used without fear of separation occuring, and therefore an even higher lift can be achieved. A moderate camber was chosen in order to reduce the effect of wing-tip vortices. A higher camber airfoil will produce a higher lift, but there is a penalty in the form of stronger induced drag from wing-tip vortices. The NACA 6425 was found to have a good balance in lift produced versus induced drag.

4.3 "Engineless Aircraft" Concept Using CFJ Airfoil

The concept Engineless Aircraft using the CFJ airfoil would not need to rely as

heavily in a any propeller or jet engine system. Instead, the CFJ airfoil itself is capable of generating thrust, which can be used to overcome the 3-D induced drag due to tip vortices. This generated thrust can be controlled by varying the strength of the air jet, and may even be used as the sole method of propulsion under certain conditions. The flying wing configuration is the most suitable for such an aircraft because the CFJ airfoil can cover the entire aircraft surface to achieve the maximum possible benefit. This flying wing is basically be a wing with the CFJ airfoil cross-section, which generates lift and thrust wherever it is applied. Thus, the majority of the drag that needs to be overcome by the CFJ airfoil thrust would be the induced drag due to tip vortices. In order to operate, such an airplane needs a pumping system to draw the jet mass flow near the trailing edge and inject the jet near the leading edge as sketched in Fig.4.4. At different phases of the flight mission, the lift and thrust can be controlled by adjusting the jet strength. At take off, a strong jet will be used to generate high thrust and high lift. At cruise, mild jet will be used due to the lower lift coefficient and thrust required. At landing, the jet will be adjusted to allow the CFJ airplane fly at high angle of attack with high lift and high drag.

A conventional airplane draws the air flow from the free-stream environment through the engine inlet, energizes the air through the combustion process, and then exhausts the high momentum air to the environment through the engine nozzle. Such a process is purely for thrust generation and has no interaction with the lift system. The energy transfer from the chemical energy of combustion to mechanical energy (momentum increase) is usually very inefficient and accompanies a very large thermal energy (total enthalpy) loss of 50% or more.

A CFJ wing draws the air flow on the suction surface of the wing near the trailing edge, pressurizes the air within the wing and then exhausts the same air near the wing leading edge. Such a process has a direct interaction with the wing and enhances the wing lift by inducing a large circulation, simultaneously generating thrust. The mass

flow of the jet will be substantially less than that of a jet engine. The jet recirculating or pumping process (suction and injection) needs much less power than running a jet engine and can be done by electric power. The energy transfer is from mechanical energy (pumping the CFJ) to mechanical energy (high momentum injection jet) and therefore the efficiency is much higher. No combustion process is needed and hence zero emission will be produced.

4.3.1 Low Energy Expenditure, Long Range and Endurance

The power required to pump the jet for this aircraft will be significantly less than the power required to run a conventional jet engine. When the power is consumed to generate the CFJ and enhance lift, it will also reduce the drag, and at low angles of attack produce thrust. For conventional airplanes, the power system is used only to overcome the drag without enhancing lift coefficient. The equivalent aerodynamic efficiency L/D of the CFJ airplane hence will be much higher than that of the conventional airplane. Since the lift coefficient of the CFJ aircraft element is significantly higher than the baseline, the overall lifting surface area to have the same payload will thus be much smaller. The weight of the airplane and the drag due to the whetted surface will be also significantly reduced. With no aircraft engines, the weight of the engines and the drag due to the engine nacelles and captured area will also be removed. The reduced weight and drag will further reduce the energy consumption.

The power consumption of the pump that drives the CFJ jet can be defined as:

$$P = \frac{\dot{m} c_p T_{01}}{\eta} \left(\left[\frac{p_{01}}{p_{02}} \right]^{\frac{\gamma-1}{\gamma}} - 1 \right) \tag{4.1}$$

where c_p is the specific heat capacity at constant pressure, taken to be $1003.4 J/kg \cdot K$, γ is the ratio of specific heats valued at 1.4, and η is the efficiency of the pump. Assuming a small unmanned reconnaissance-type aircraft with a chord length of $1.16m$, the power necessary to drive this pump at a take-off speed of $M = 0.1$ is only $79.1W$.

As seen from Eq. 4.1, the power required to pump the jet is determined by the ratio of the total pressure at the injection and suction and the mass flow rate of the jet. The jet pressure ratio for this aircraft has been calculated to be about 1.1, whereas the ratios seen with conventional jet engines can be as high as 40. Compared with a jet engine system, the reduction of power required comes from the following 5 sources:

1. The mass flow rate of the jet is much smaller than the mass flow rate of a jet engine; conservative estimations show that the maximum jet mass flow rate would not exceed 30% of that of a conventional jet engine

2. The total pressure ratio to pump the jet is much smaller than that of a jet engine compressor, CFD analysis shows that the velocity at the jet injection do not exceed a Mach number of 0.65

3. The CFJ injection and suction are located at the most energy efficient locations. The suction is at near trailing edge where pressure is the highest except the LE stagnation point. Injection is downstream of the leading edge suction peak where the pressure is the lowest. The pressure gradient is favorable to recirculate the jet and minimize the power required to pump and energize the jet

4. No combustion is needed and hence very little thermal loss occurs

5. The overall Engineless airplane weight and drag is much less than the conventional airplane. The energy expenditure is hence greatly reduced

Conceptually, based on the data of the F-5E aircraft mission analysis [6], the estimation shows that the reduction of the power required for an Engineless CFJ airplane could be up to 70% or more. The lower power consumption of a CFJ airplane will give much longer range and endurance than a conventional airplane.

4.3.2 Extremely Short Take Off/Landing Distance

The take off/landing distances and the stall velocity are determined only by the maximum lift coefficient. The CFJ airplane will hence have extremely short take off/landing (ESTOL) distance due to the very high maximum lift coefficient. For the same reason, the stall velocity will be significantly lower than the conventional airplane. The lower stall velocity will allow soft landing and take off at substantially lower speed. Another important use of CFJ airfoil during take off/landing is to enhance the subsonic performance of a supersonic wing for a supersonic airplane.

4.3.3 High Maneuverability and Safety

Due to the high stall margin, the CFJ airplane will have significantly higher maneuverability and safety margin to resist severe weather conditions, such as unexpected gusts of wind. The high stall margin is also particular useful for Mars airplanes to resist flow separation and stall at low Reynolds number.

4.3.4 Jet effects on CFJ aircraft performance

By using a control volume analysis, Zha and Gao derived an expression for the force effect of the injection and suction jets on the CFJ wing [30]. In keeping with Newton's third law, at the injection and suction slots, the high velocity flow produces a reactive force which must be taken into account in the drag and lift calculations. The expressions for these reaction forces are given as:

$$F_{x_{cfj}} = (\dot{m}_j V_{j1} + (p_{pj1} A_{j1}) * cos(\theta_1 - \alpha) - \gamma(\dot{m}_j V_{j2} + (p_{j2} A_{j2}) * cos(\theta_2 + \alpha) \quad (4.2)$$

$$F_{y_{cfj}} = (\dot{m}_j V_{j1} + (p_{pj1} A_{j1})) * sin(\theta_1 - \alpha) - \gamma(\dot{m}_j V_{j2} + (p_{j2} A_{j2})) * sin(\theta_2 + \alpha) \quad (4.3)$$

where the subscripts 1 and 2 refer to the injection and suction respectively and θ_1 and θ_2 are the angles that the injection and suction slots, respectively, make to the vertical. A definition for these angles can be seen in Figure 4.5.
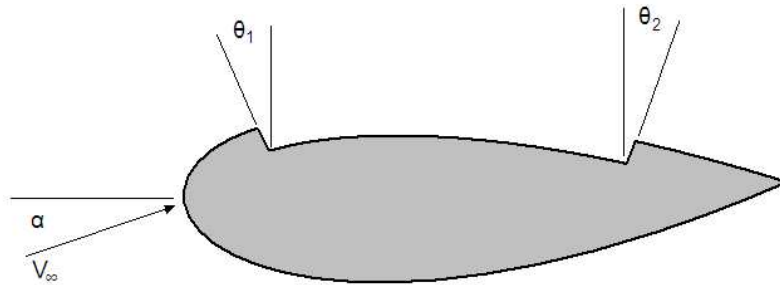

Figure 4.5: Definition of angles θ_1 and θ_2 with respect to angle of attack α

The total modified lift and drag on the wing can then be expressed as:

$$D = R'_x - F_{x_{cfj}} \quad (4.4)$$

$$L = R'_y - F_{y_{cfj}} \quad (4.5)$$

These quantities modify the forces calculated from the surface integral, R'_x and R'_y, in order to correct for the reaction forces induced by the jet effect. It is expected, as can be seen from equations 4.2 and 4.3, that the corrected Lift will decrease when $v_{j1} > 0$ and increase when $v_{j1} < 0$.

4.4 Past Results

4.4.1 Two Dimensional CFD Simulation

As a preliminary to the fully three dimensional CFD simulation of the CFJ airplane, a two dimensional CFD simulation of the CFJ6425-065-196 airfoil was first carried out. This designation means that the baseline airfoil is the NACA6425, the injection slot size is 0.65% of the chord length and the suction slot size is 1.96% of the chord. A simulation of the baseline NACA6425 airfoil was also performed for the purpose of comparison with the CFJ case. Flow and computational conditions for this simulation can be found in Table 4.1.

Variable	Value
Mach	0.1
p_{outlet}	71.42857
p_{total}	71.92982
Reynolds	2000000
T_{total}	1.002
CFL	0.1
LHS Scheme	Zha2
RHS Scheme	Van Leer
LHS Order	3
RHS Order	1
Time Steps	15000

Table 4.1: Flow and numerical conditions given in *datain* file for 2D CFJ6425-065-196 case

CFD simulations for the two-dimensional case show that separation, and therefore stall, occurs for the baseline airfoil at 16° angle of attack, while it occurs at 35° AoA for the CFJ airfoil, a 19° difference, as shown in Table 4.2. This constitutes a significant increase in performance because a higher lift can be produced without the danger of stalling, even at a relatively low Mach number of 0.1. These results imply that the stall velocity for such an aircraft would be drastically reduced, and operational angle of attack vastly increased. A lower stall velocity and increased lift can lead to reduced

take-off and landing distances, which is a very highly desirable trait.

Furthermore, it can be seen that the two-dimensional drag coefficient C_d is negative in the case of the CFJ airfoil at angles of attack as high as 20°. The drag coefficient becomes positive at high angles of attack because the form drag has become large enough at that point to overcome the thrust generated by the CFJ airfoil. However, it would be improbable that the aircraft would ever need to fly in conditions where the angle of attack were so high. Even at high angles of attack, however, the drag coefficient of the CFJ airfoil is much lower than that of the baseline airfoil, reducing the high drag generated at such conditions.

α	BL C_l	CFJ C_l	BL C_d	CFJ C_d
0	0.0542	2.8517	0.0232	-0.9855
10	1.3946	3.9734	0.0408	-0.5939
15	1.5225	5.0729	0.0558	-0.3168
20	1.4431	5.4402	0.0686	-0.1217
30	1.1147	6.5638	0.1690	0.2613
35	0.9348	5.5526	0.2342	0.1913

Table 4.2: 2-D CFD results for aerodynamic parameters of baseline (BL) airfoil and CFJ airfoil.

4.4.2   Wind Tunnel Testing

Wind Tunnel testing was performed at the University of Florida wind tunnel facilities by the team of Dr. Zha [31, 32]. The airfoil used for these experiments was the CFJ0025 airfoil, which is derived from the cross-section of the NACA0025 airfoil. Tests were performed for two cases, the first being the CFJ0025-065-196, with an injection slot size of 0.65% and a suction slot size of 1.96% of the chord, the second being the CFJ0025-131-196, with an injection slot size of 1.31% and a suction slot size of 1.96% of the chord. Wind Tunnel tests were run for these two cross sections both with a trip added at the leading edge to induce turbulent flow within the boundary layer, and without the trip.
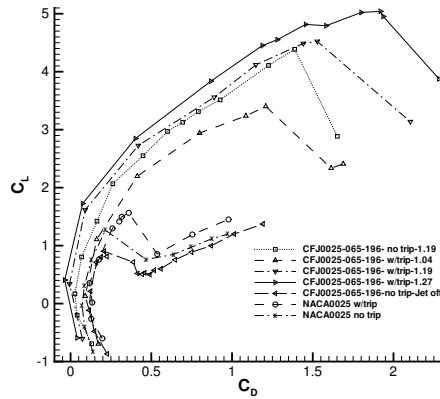
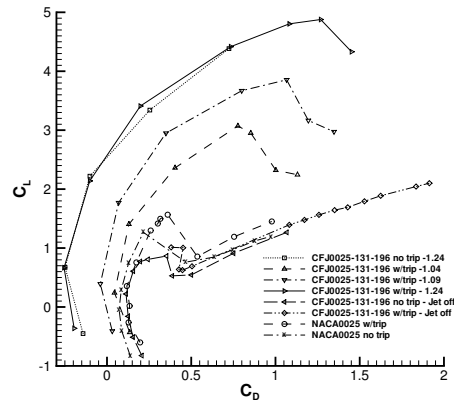Figure 4.6: Measured drag polar of CFJ0025-065-196 airfoil.

Figure 4.7: Measured drag polar of CFJ0025-131-196 airfoil.

The measured drag polar curves for this series of experiments can be seen in Figures 4.6 and 4.7. Results showed a significant improvement in performance over the baseline for all cases which utilized the CFJ airfoil section. Maximum coefficient of life C_L was seen to increase 220%, while stall margin was seen to increase by 132%.

4.5 3D CFD Simulation

A three dimensional CFD simulation was carried out for the CFJ flying wing case. For comparison, a comparable CFD simulation was also carried out for the baseline geometry, which consists of the same shape as the CFJ airplane, but excluding the CFJ slot. Due to the streamlined nature of the geometry, a low order simulation was sufficient to acquire high-fidelity results. Due to the symmetry of the case, it was only necessary to run CFD on one half of the wing, and a symmetry boundary condition was used to mirror the results.

4.5.1 Mesh Generation for CFD

The mesh generated for this case can be seen in Figure 4.8, and its block allocation can be seen in Figure 4.9. The mesh consisted of eight blocks consisting of the following:

block	section	size	number of cells
1	top front	29×64×114	201666
2	top center	38×64×114	264252
3	top rear	29×64×114	201666
4	bottom rear	24×64×114	201666
5	bottom rear center	24×64×114	201666
6	bottom front center	24×64×114	201666
7	bottom front	24×64×114	201666
8	cfj slot	38×20×40	30400
total	-	-	1504648

Table 4.3: Block allocation for CFJ Airplane mesh

Block sizes were chosen such that the CPUs running the code were not overloaded with data. A total number of eight blocks with about 200000 solutions point each was found to be an ideal size. The CFJ slot was given its own block for simplicity in mesh generation. An O-mesh was chosen for its relatively simple shape and conformity to the geometry.

The geometry of the airplane was modified slightly in the wingtip region for the
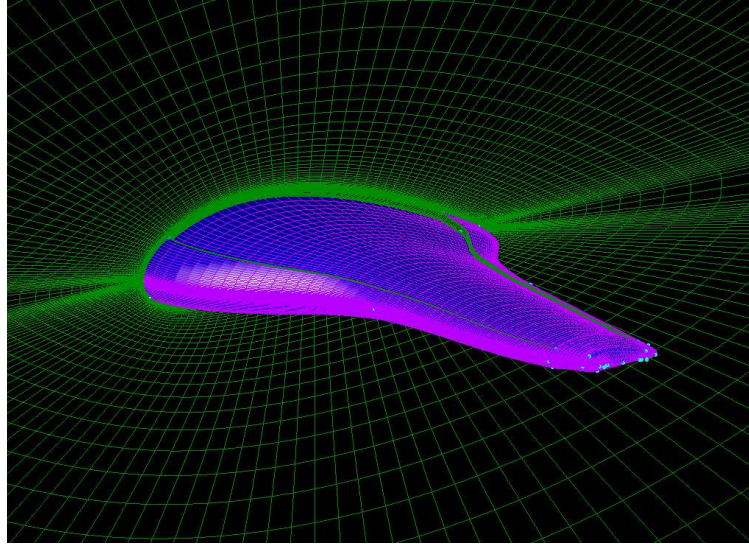
Figure 4.8: Mesh generated for CFJ Airplane case

purpose of mesh generation. This was necessitated by the need to reduce the geometry from a doubly-connected to a simply-connected domain. This was necessary because the far-field flow, which is a simply-connected domain is also simulated in a direction away from the wingtip. In order to generate a suitable mesh on this sort of geometry, it is necessary to reduce the doubly-connected O-shape or the wing to a line. This was achieved by giving a high slope to a small section of the wingtip, such that it was reduced to a line, as shown in Figure 4.10.

4.5.2 CFD Pre-Processing

The CFJ airplane case was simulated at a low Mach number, corresponding to the take-off phase of flight when the highest demands are made on the system. Ambient conditions are given in Table 4.4. These conditions are specified in the *datain* file, which is subsequently read by the main CFD code.

The variable p_{outlet} is the incoming flow dimensionless static pressure, defined as

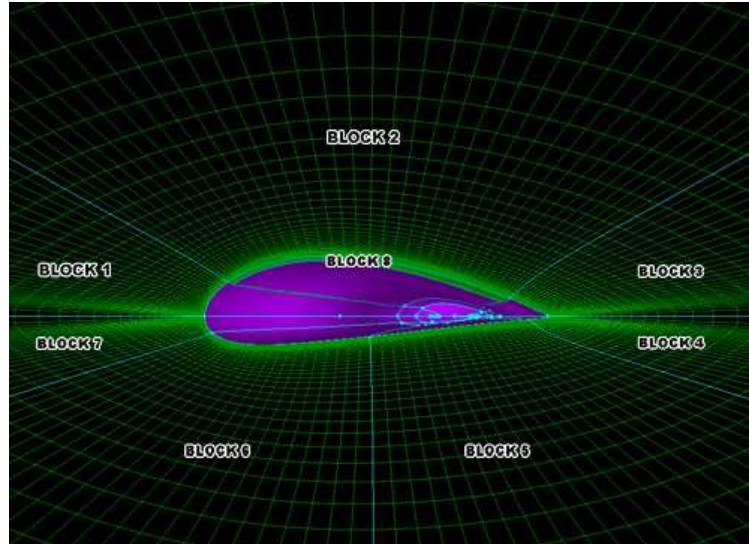$$p_{outlet} = \frac{1}{\gamma M^2} \tag{4.6}$$

Figure 4.9: Block configuration for CFJ Airplane mesh

Variable	Value
Mach	0.1
p_{outlet}	71.42857
p_{total}	71.92982
Reynolds	2000000
T_{total}	1.002

Table 4.4: Flow conditions given in *datain* file for CFJ case

and p_{total} can be obtained from p_{outlet} as

$$\bar{p}_{total} = \frac{p_{total}}{p_\infty} \left(1 + \frac{\gamma - 1}{2} M^2\right)^{\frac{\gamma}{\gamma - 1}} \tag{4.7}$$

Similarly, T_{total} can be found from the relation

$$\bar{T}_{total} = \frac{T_{total}}{T_\infty} \left(1 + \frac{\gamma - 1}{2} M^2\right) \tag{4.8}$$

4.5.3 Boundary Condition Definition

The full boundary condition setup can be seen in the appendix, where the *datain* file is included in its entirety. The boundary conditions used for the CFJ Airplane case
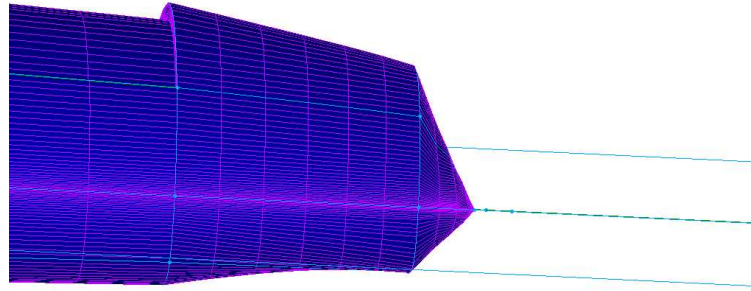
Figure 4.10: Wingtip geometry for CFJ Airplane case

are as follows:

- BC 3 - no-slip wall boundary given at all aircraft surfaces

- BC 5 - subsonic outlet used along the injection slot

- BC 6 - subsonic inflow used at the far-field where flow is entering the region

- BC 7 - interface boundary for MPI used at all block boundaries

- BC 8 - symmetry boundary used along the root of the aircraft to indicate mirrored results

- BC 9 - subsonic outlet used along the suction slot

- BC 11 - subsonic outflow used at the far-field where flow is leaving the region

4.5.4 CFD Simulation Setup

A steady state third order CFD simulation was performed on the CFJ airplane geometry as well as the baseline geometry in a range of angles of attack from $-5°$ to

45°. The baseline geometry consists of the same cross-section and body shape as the CFJ airplane model, but with no CFJ slot on the suction surface. It is therefore completely smooth and more akin to a traditionally shaped aircraft. A Zha CUSP 2 scheme was used as the numerical scheme for the left-hand side (LHS) of the Navier-Stokes equation, and a Van Leer scheme for the right-hand side (RHS). The numerical parameters used in the computation are listed in Table 4.5.

Variable	Value
CFL	10.0
LHS Scheme	Zha2
LHS Order	3
RHS Scheme	Van Leer
RHS Order	1
Time Steps	7500
Initial L2 Residual	0.57E-04
Final L2 Residual	0.15E-07

Table 4.5: Numerical parameters given in *datain* file and residuals for CFJ airplane case

The simulation for the CFJ airplane converged well to three orders of magnitude, beginning with an $L2$ residual in the order of 10^{-4} and converging to a value in the order of 10^{-7}, as shown in Figure 4.11.

4.6   Results

A plot of the CFD computed three-dimensional coefficient of lift C_L for a range of angles of attack α can be seen in Figure 4.12. The jet effect, which tends to have the negative effects of decreasing lift and increasing drag has been taken into account. Computational results show that the CFJ airplane begins to stall at an angle of attack of about 35°, much higher than that computed for the baseline of 15°. This constitutes an increase in stall margin of 57%, which is a very significant improvement in performance. These results imply that the stall velocity for such an
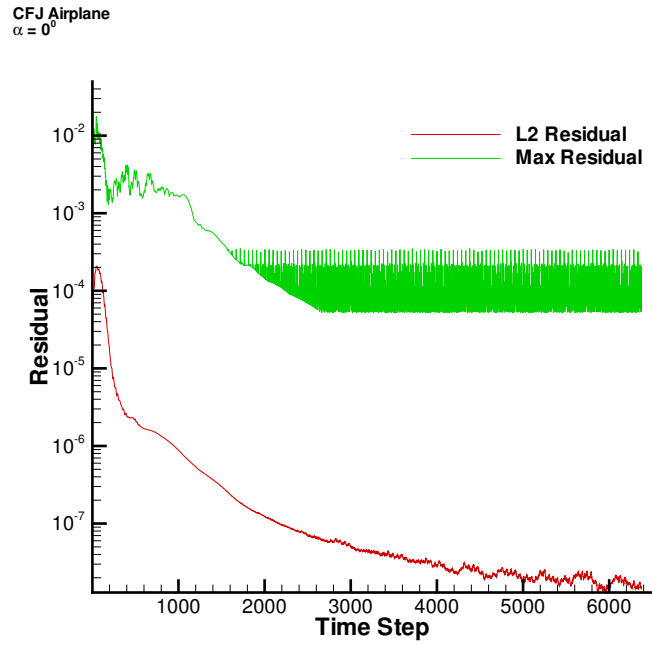
Figure 4.11: L2 and maximum residuals for CFJ airplane simulation at $\alpha = 0$

aircraft would be drastically reduced, due to its ability to keep flow attached even with adverse pressure gradients. A lower stall velocity and increased lift will lead to reduced take-off and landing distances.
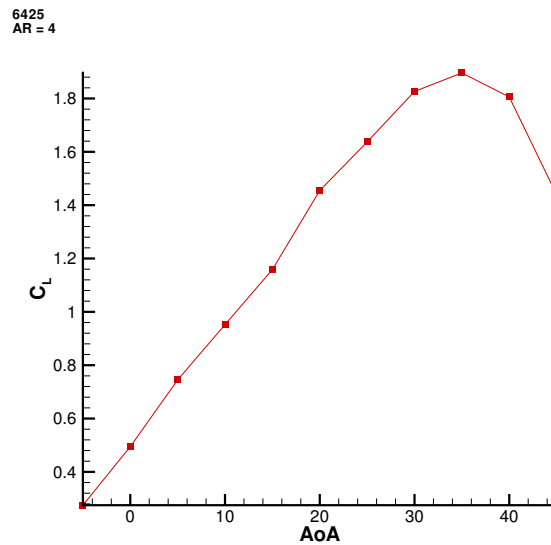

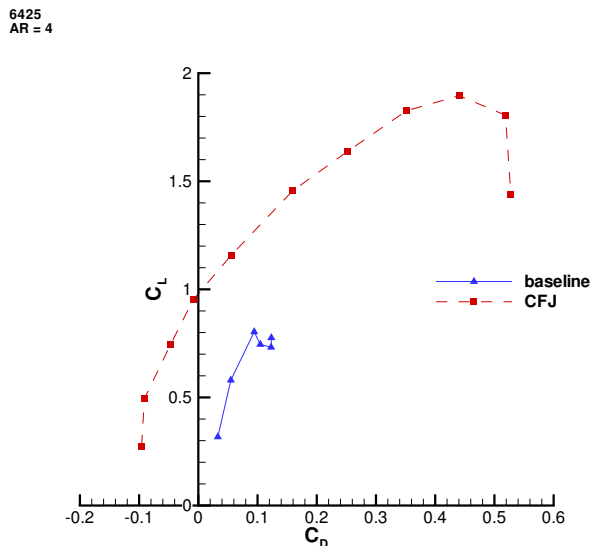Figure 4.12: Computed 3D C_L vs. α curve for CFJ airplane

Figure 4.13: Computed 3D drag polar curve for CFJ airplane compared to baseline

A comparison of the drag polar curves of the CFJ airplane and the baseline geometry can be seen in Figure 4.13. The maximum C_L can be seen to increase 137.5% for the CFJ airplane value of 1.9 over the baseline value of 0.8. Also, the C_D remains negative in a range of angles of attack from $-5°$ to $10°$. Over this range, the CFJ airfoil is producing net thrust, having overcome all drag sources. While drag becomes positive for large angles of attack, it is improbable than any aircraft would be operating within such a range. It can therefore be said that this aircraft produces net thrust over the operating range without the use a conventional engine. Therefore, it can be concluded that implementation of the CFJ airfoil into a wing will reduce the amount of thrust that needs to be provided by the main engine, and thus increase its efficiency.

Figure 4.14 shows a plot of the sources of drag and lift over the span of the airplane at $\alpha = 0°$. From this figure, it can be seen that over the span at which the CFJ airfoil section occurs the wing is generating a net thrust as well as a much higher lift compared to the section in the wingtip where no CFJ airfoil is present. Over this range, the thrust provided by the CFJ is greater than that needed to overcome the
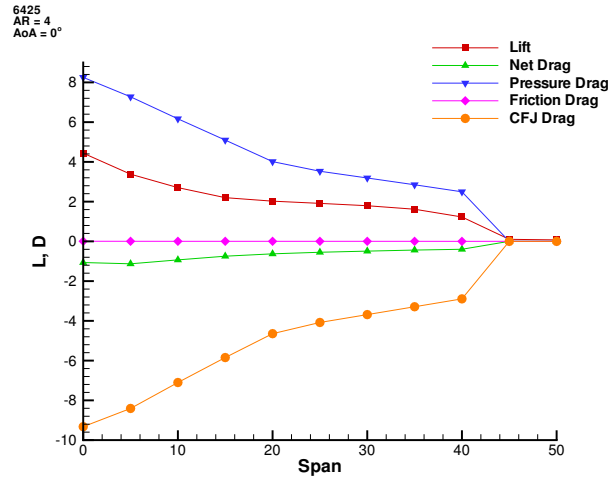
Figure 4.14: Lift and Drag distribution over CFJ airplane span at $\alpha = 0°$

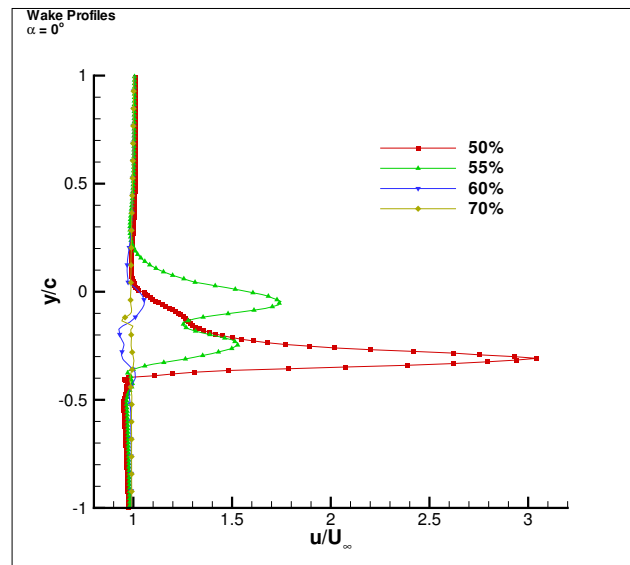sum of the pressure and friction drag generated by the wing.

Figure 4.15: Wakeshape at varying sections for CFJ airplane compared to baseline for $\alpha = 0°$

Wake profile plots for the aircraft at different sections along the wing show that there is a velocity surplus within the wake of the aircraft, where normally a velocity deficit is expected. This surplus has a maximum value at the root, decreasing towards the mid-span, and becoming a deficit towards the wingtips. This result is expected
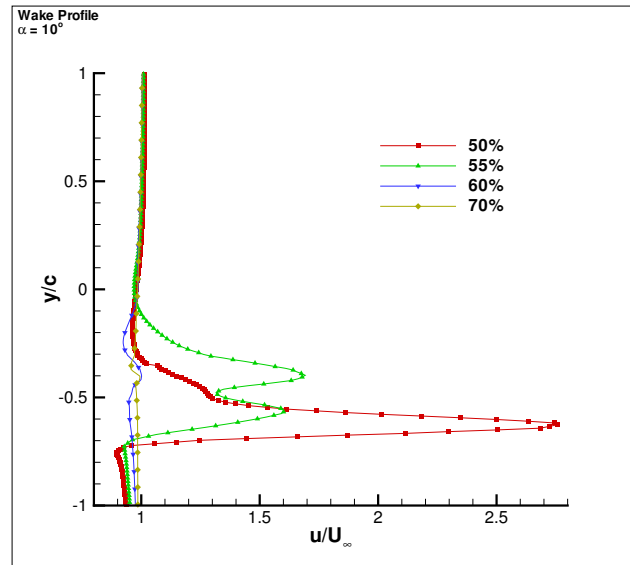
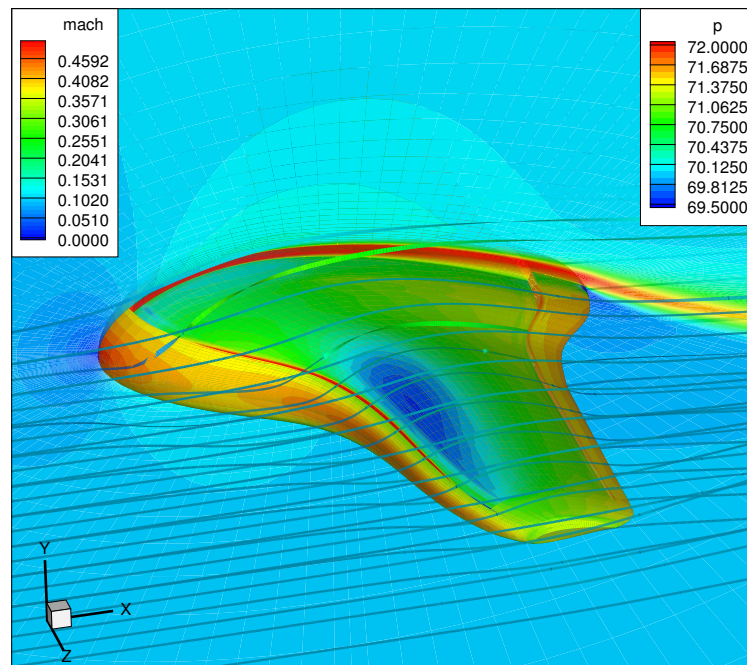Figure 4.16: Wakeshape at varying sections for CFJ airplane compared to baseline for $\alpha = 10°$

Figure 4.17: Root Mach contours, surface pressure contours, and 3D streamlines for CFJ airplane at $\alpha = 0°$

because the wingtips do not make use of the CFJ airfoil. Induced drag from wing-tip vortices also becomes significant in this wingtip region, as an be seen from Figures 4.15
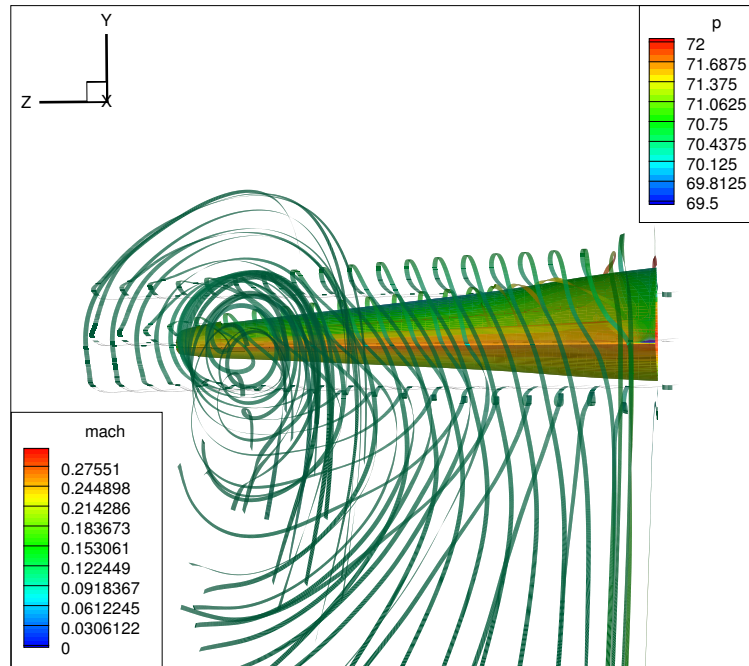
Figure 4.18: 3D rear view of CFJ airplane showing wing-tip vortices for $\alpha = 0°$

and 4.16. The wingtip vortices are relatively large due to the high 25% thickness of the airfoil, and can be seen in Figure 4.18. However, when averaged over the wingspan, the net drag is negative at low angles of attack. Under traditional circumstances, the wake of a wing features flow that is slower than in surrounding areas, that is, a velocity deficit. This is due to the energy which has been lost in the viscous boundary layer due to skin friction and fluid viscosity. However, the CFJ wake is particular in that the flow within it is dramatically faster than in surrounding areas, as can see from Figures 4.15 and 4.16. This increase of velocity can be attributed to the extra energy which is being injected into the boundary layer via the CFJ jet. Even though zero net mass flux is maintained by suctioning the same amount of air, the incoming flow has been energized though turbulent mixing, causing it to accelerate. Thus, the suctioned air has a lower velocity than when it was injected, having transfered much of its energy onto the incoming flow. This type of wake profile will lead to a net thrust being produced [6,9,30]. The increase in velocity in the wake can also be seen in Fig.

4.17, which shows Mach number contours in a slice of the 3D flow corresponding to the root of the aircraft. This plot also shows 3D streamlines above and below the wing.
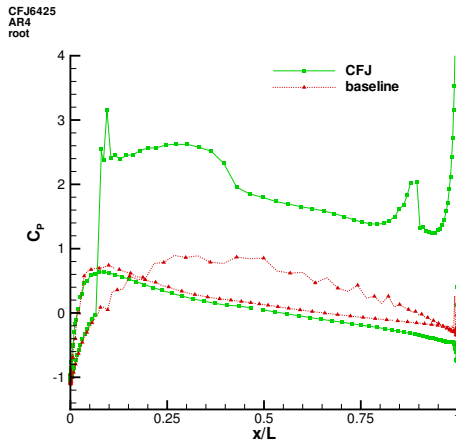

Figure 4.19: Root distribution of surface C_p of CFJ airplane compared to baseline for $\alpha = 0°$

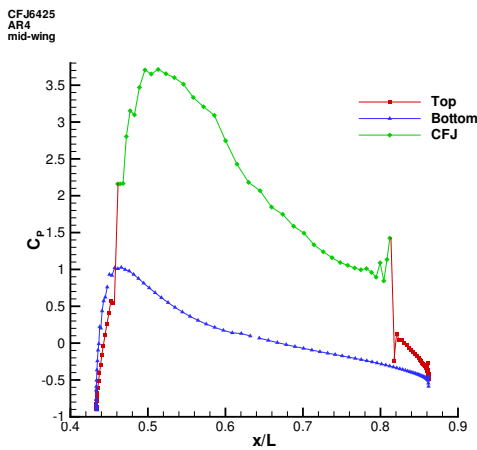Figure 4.20: Mid-span distribution of surface C_p of CFJ airplane

Figure 4.19 shows the pressure coefficient distribution over the surface of the CFJ aircraft at the root, compared to the surface C_p distribution over the baseline geometry. The surface pressure coefficient is defined in Equation 4.9. Note that a pressure higher to the reference value p_∞ will have a negative C_p value, whereas a low

pressure will have a positive value. The much greater area between the curves formed by the upper and lower surfaces in the CFJ case accounts for the dramatic increase in lift over the baseline. The surface pressure coefficient remains very similar for the two cases at the leading edge, trailing edge, and bottom surface, areas which not covered by the CFJ slot. However, the C_p can be seen to become up to 70% higher over the CFJ section of the wing. Therefore, the bulk of the increse in lift can be attributed to the introduction fo the CFJ airfoil section.

$$C_p = -\frac{p - p_\infty}{\frac{1}{2}\rho V_\infty^2} \tag{4.9}$$
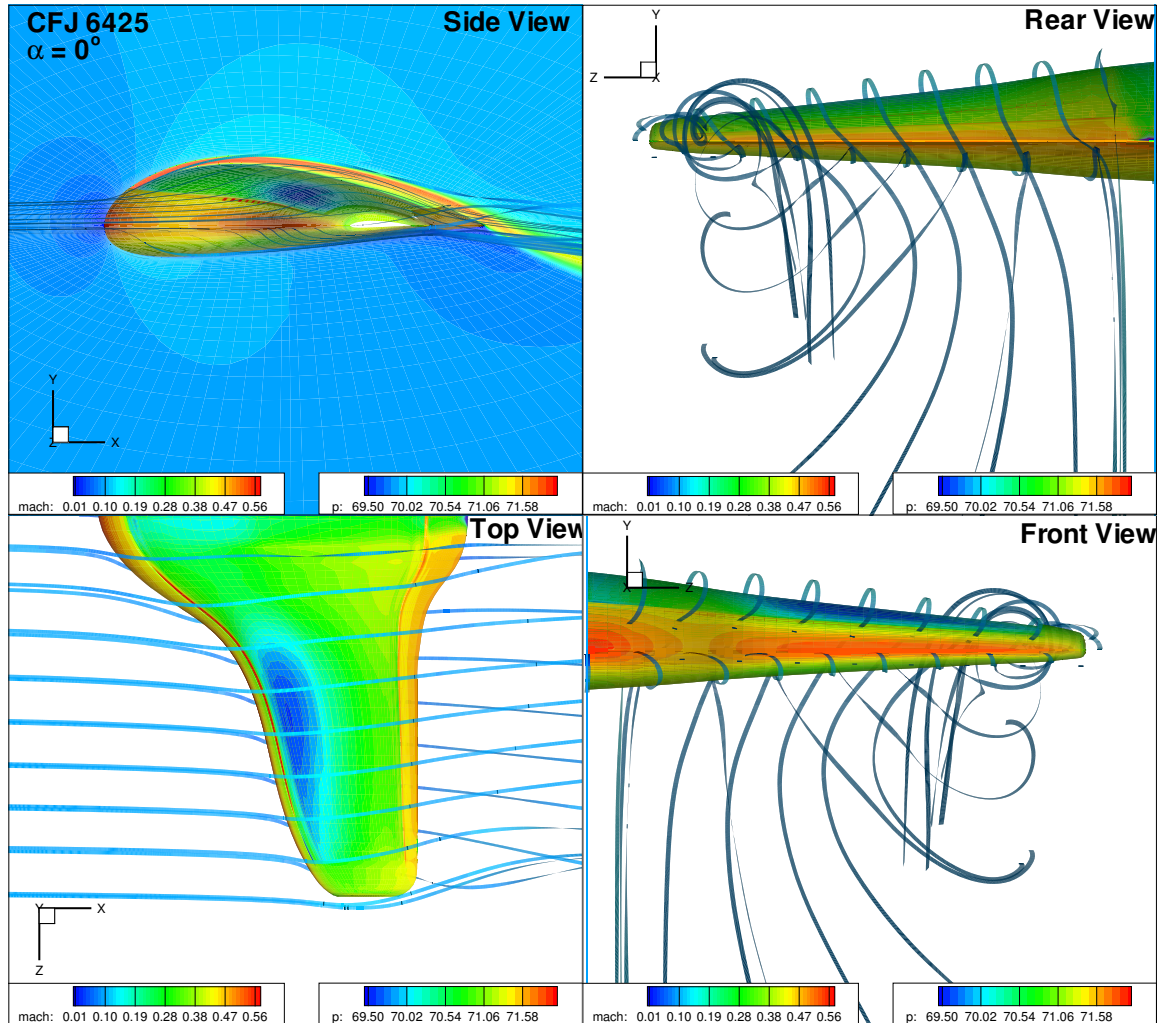
4.6.1   Detailed Results for Different Angles of Attack

Figure 4.21: 3D surface pressure contours with Mach contours in mid-plane and 3D streamtraces for $\alpha = 0°$

Figure 4.21 shows four different three dimensional views for the CFJ airplane at an angle of attack of zero degrees. Dimensionless pressure contours are shown on the surface of the airplane, and Mach contours are shown in the mid-plane of the z-axis, as well as on the streamtraces. From the side view streamtraces, it is clear that flow around the airplane is very clean and attached. It can also be seen that there is accelerated flow from the jet in the wake of the aircraft. The maximum velocity is reached within the CFJ slot at a Mach number of 0.56. The front view shows that

maximum surface pressure is located at the stagnation point in the leading edge of the airplane. The top view shows that the lowest pressures occur within the CFJ slot. The rear view shows that while wing-tip vortices are present, they are not particularly strong.
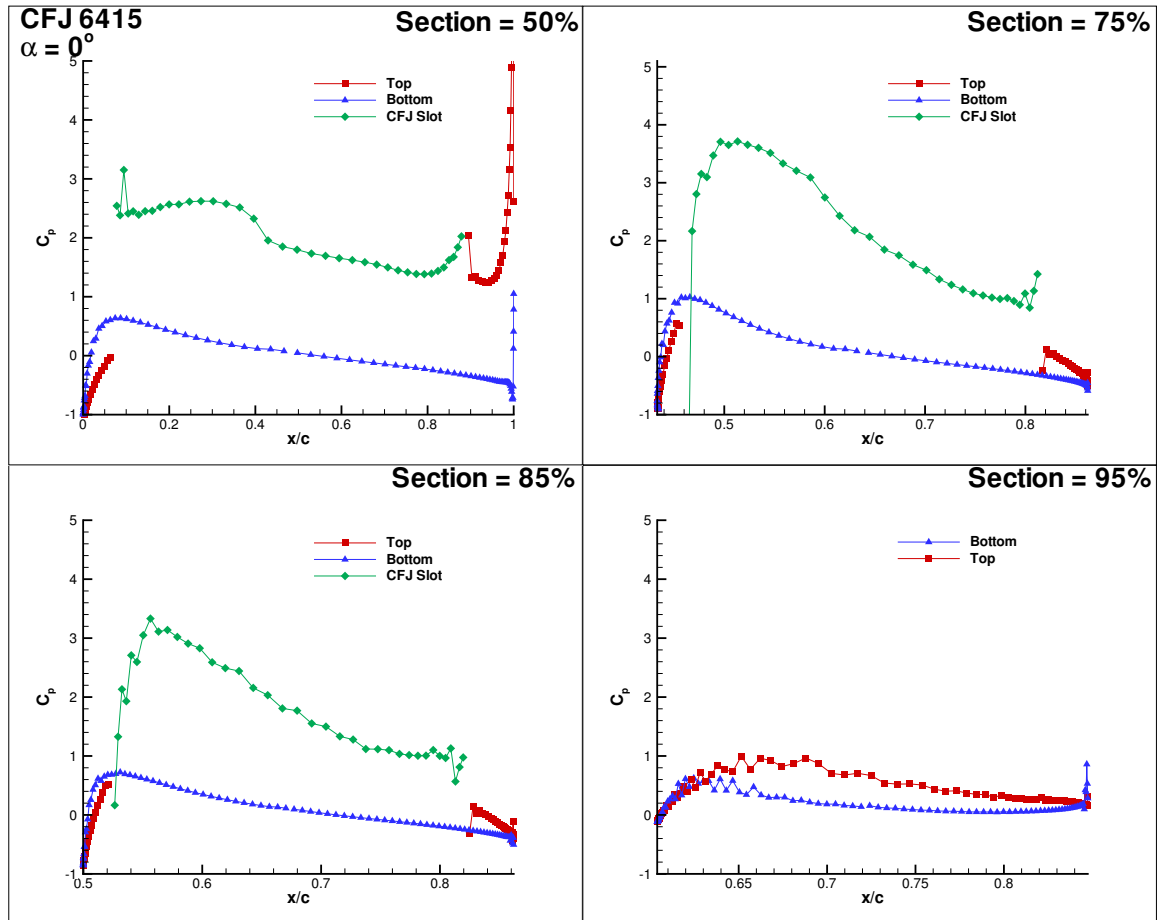
Figure 4.22: Pressure coefficient profiles for CFJ airplane at several span-wise locations for $\alpha = 0°$

Figure 4.22 shows the pressure coefficient profiles as a function of the chord. Profiles are shown at several locations along the span-wise direction corresponding to 50%, 75%, 85%, and 95% of the total wing span. Note that the vertical scale is kept constant for the four profiles for comparison, but the horizontal scale varies from plot to plot according to the varying chord length along the wing span. In the first three profiles, which occur in areas of the span with the CFJ airfoil cross-section, the

majority of the lift is produced within the CFJ slot (green line). The C_p reaches a peak of 0.4 at the front section of the CFJ slot. The lift contribution, which is the area between the upper and lower curves, is greater towards the front of the slot, and this difference in contribution becomes more pronounced towards the wingtip. The final profile, which occurs in the wingtip, where there is no CFJ cross-section, the lift contribution along the entire chord drops dramatically. This can be attributed to the disappearance of the CFJ slot in this section.
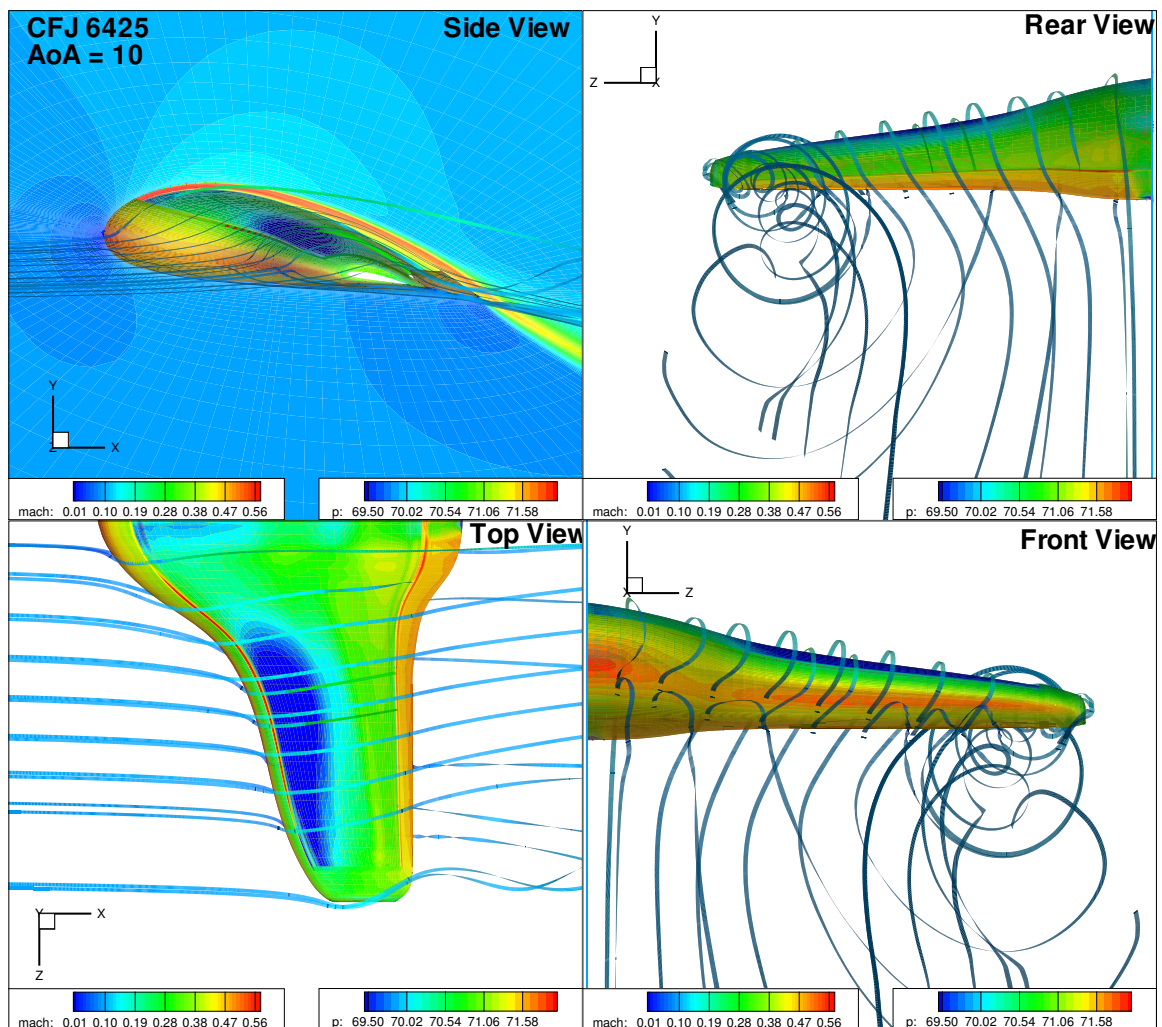

Figure 4.23: 3D surface pressure contours with Mach contours in mid-plane and 3D streamtraces for $\alpha = 10°$

Figure 4.23 shows the four views for the CFJ airplane at $\alpha = 10°$. From the side

view it is apparent that flow still remains clean and well attached. The accelerated flow within the wake is still present at this angle of attack. From the top view it can be seen that the low pressure area within the CFJ slot has become more extensive. The highest pressure can still be found in the leading edge stagnation point. From the rear view, it can be seen that the wing-tip vortices have become more pronounced.

Figure 4.24: Pressure coefficient profiles for CFJ airplane at several span-wise locations for $\alpha = 10°$

Figure 4.24 shows the C_p profiles at the same locations used previously. The majority of the lift still comes from the CFJ slot area. The root profile is similar to that of the $\alpha = 0°$, however there is an additional area of low pressure at $x/c = 0.6$. This low pressure area, however, is localized and seems to dissipate quickly.

The 75% and 85% sections again show a higher contribution to lift from the front

Figure 4.25: 3D surface pressure contours with Mach contours in mid-plane and 3D streamtraces for $\alpha = 20°$

section of the CFJ slot. The peak C_p is higher at this angle of attack, reaching a value of 0.5 in the front section of the CFJ slot, the same location as for $\alpha = 0°$. Once again, at the wing-tip section of 95%, the lift contribution drops drmatically.

Figure 4.25 shows the four views for the CFJ airplane at $\alpha = 20°$. Flow around the airplane still remains well attached for this angle of attack. Flow is still highly accelerated within the wake region. The low pressure areas within the CFJ slot are becoming even more extensive and pronounced. The high pressure stagnation point at the LE is moving towards the lower surface of the aircraft. Wing-tip votrices are
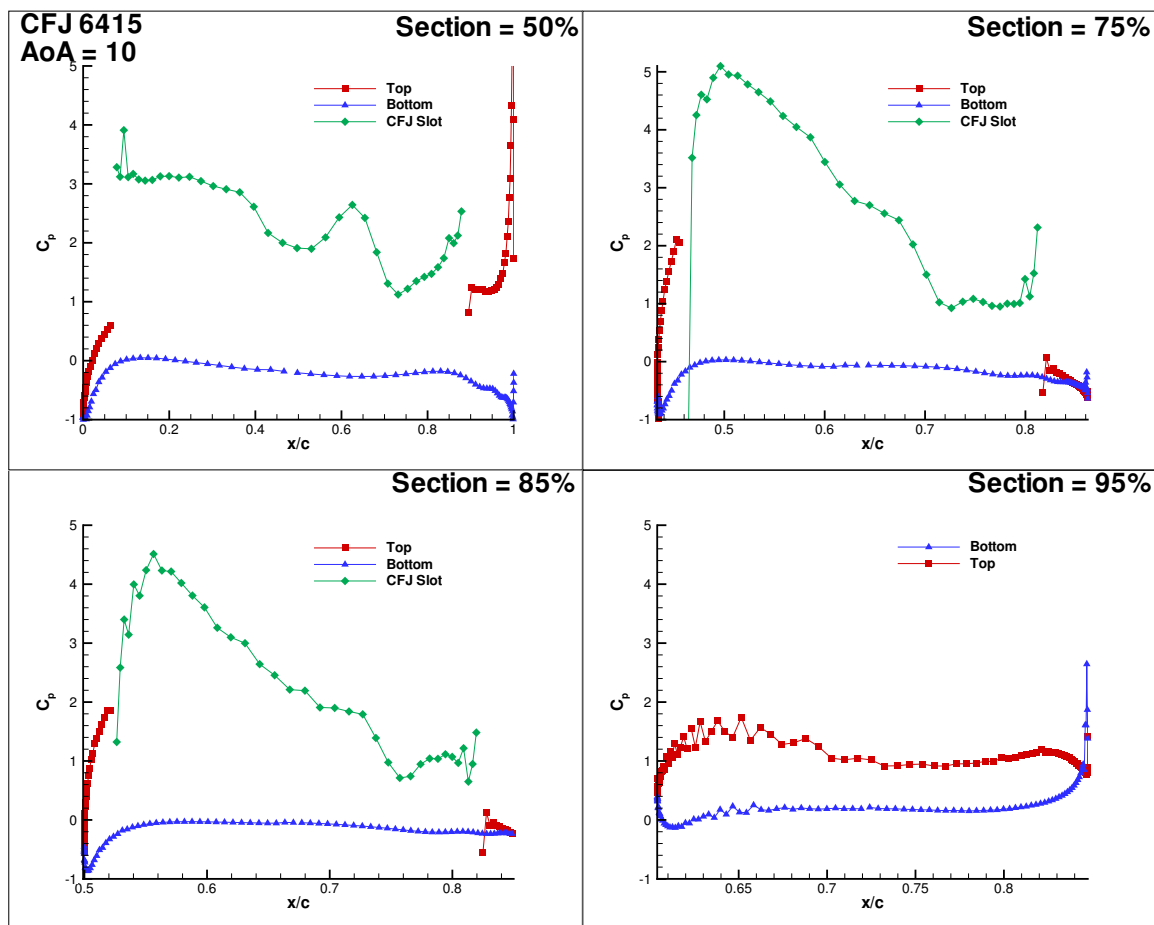
becoming very strong.

Figure 4.26: Pressure coefficient profiles for CFJ airplane at several span-wise locations for $\alpha = 20°$

Figure 4.26 shows the C_p profiles for an angle of attack of 20°. The local area of low pressure at the root section is no longer present, creating a profile more similar to that of $\alpha = 0°$. Peak C_p is even higher, reaching a value of 0.7 at the frontal section of the CFJ slot, which continues to have a higher contribution to lift over the rear area. Lift contribution overall has increased over lower angles of attack, even within the wing-tip section.

Figure 4.27 shows the four views for the CFJ airplane at $\alpha = 30°$. At this angle of attack, flow is still reasonable attached although a tendency towards detachment is becoming apparent towards the rear of the aircraft. Flow within the wake region
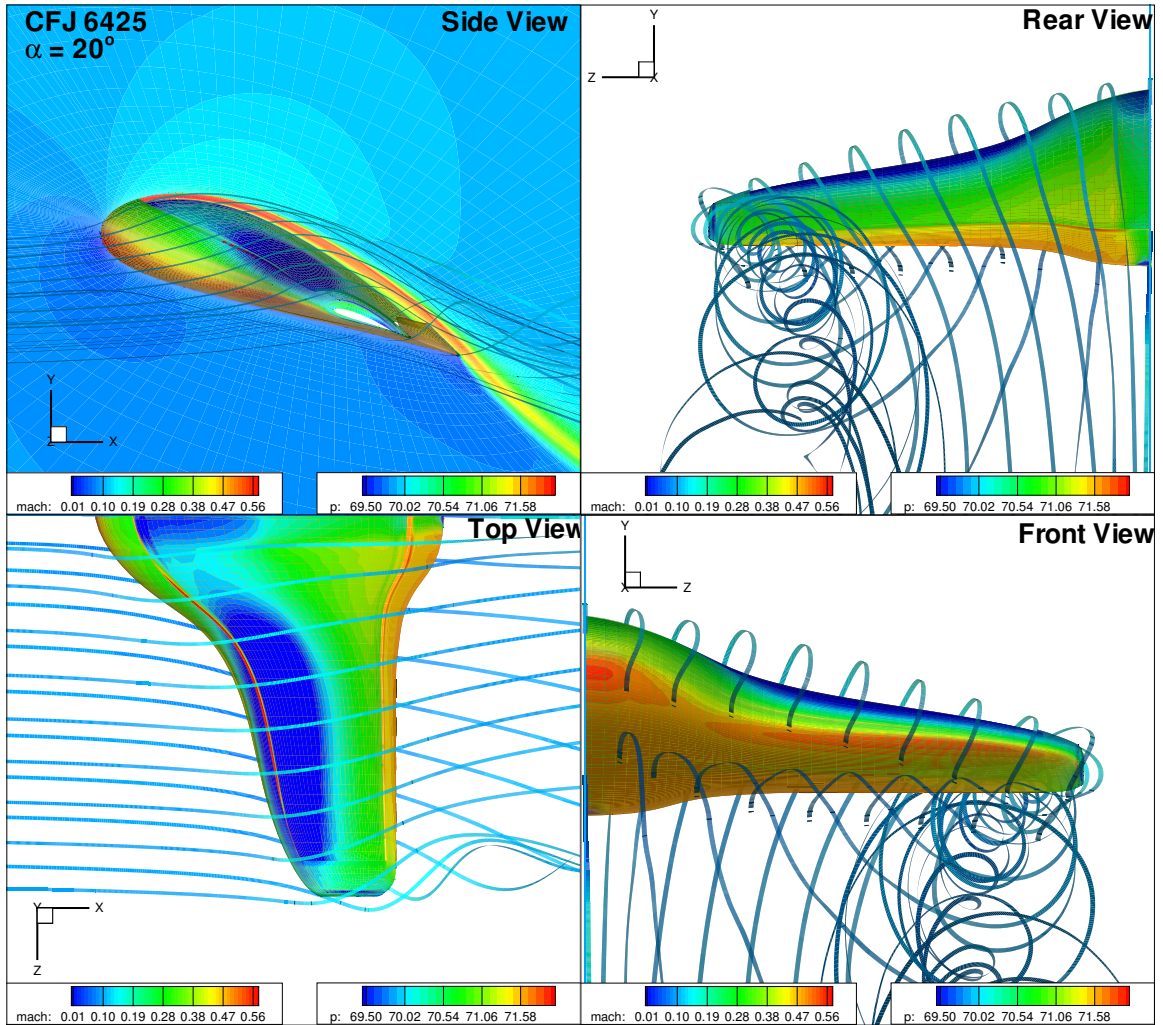
Figure 4.27: 3D surface pressure contours with Mach contours in mid-plane and 3D streamtraces for $\alpha = 30°$

remains highly accelerated. The low pressure area in the front part of the CFJ slot is very extensive, and has spilled over onto the top of the leading edge. The high pressure stagnation point has moved clearly onto the lower surface fo the airplane. Wing-tip vortices are becoming very strong, and dominate the flow behind the airplane.

Figure 4.28 shows the C_p profiles for an angle of attack of 30°. The peak C_p has increased further to a value above 0.8. The high lift contribution from the front part of the aircraft has further increased over lower angles of attack. Overall lift is very high, and there is no sign yet of strong separation.
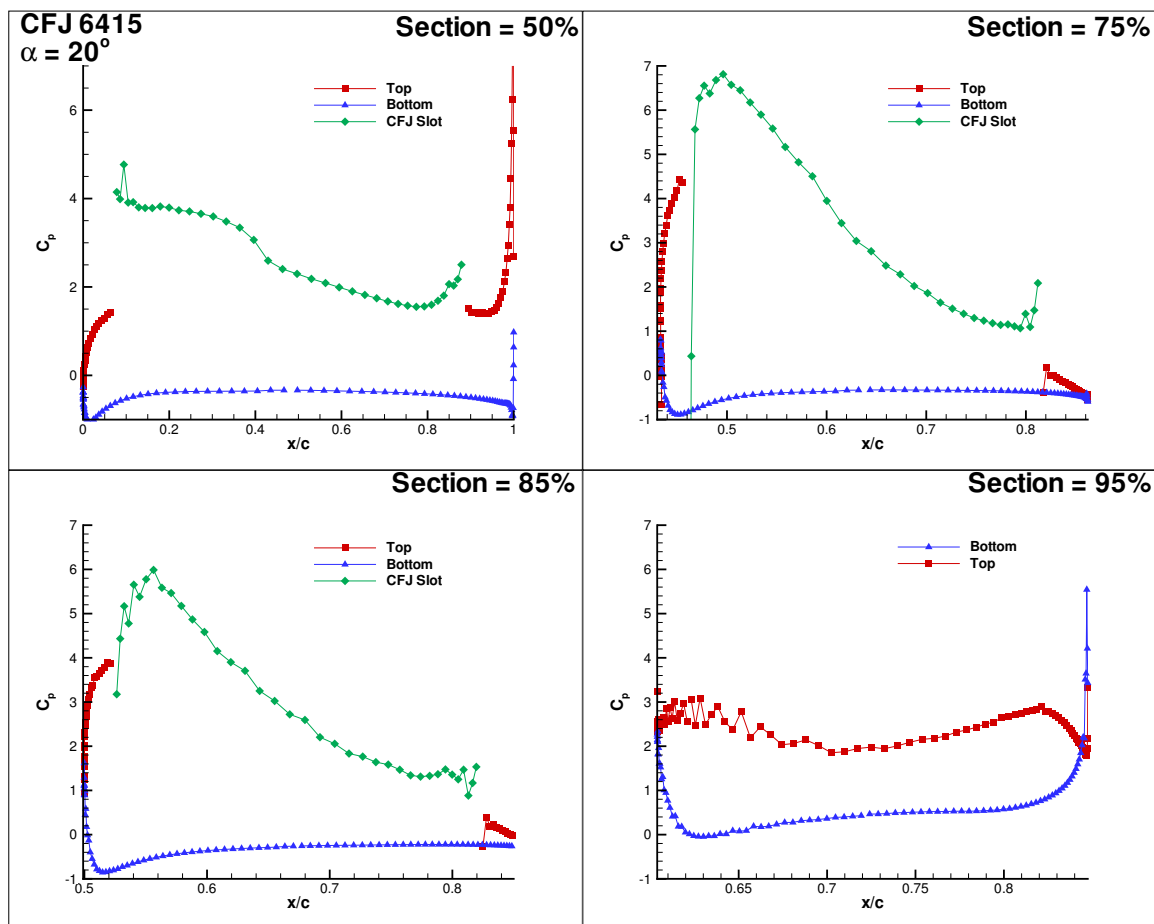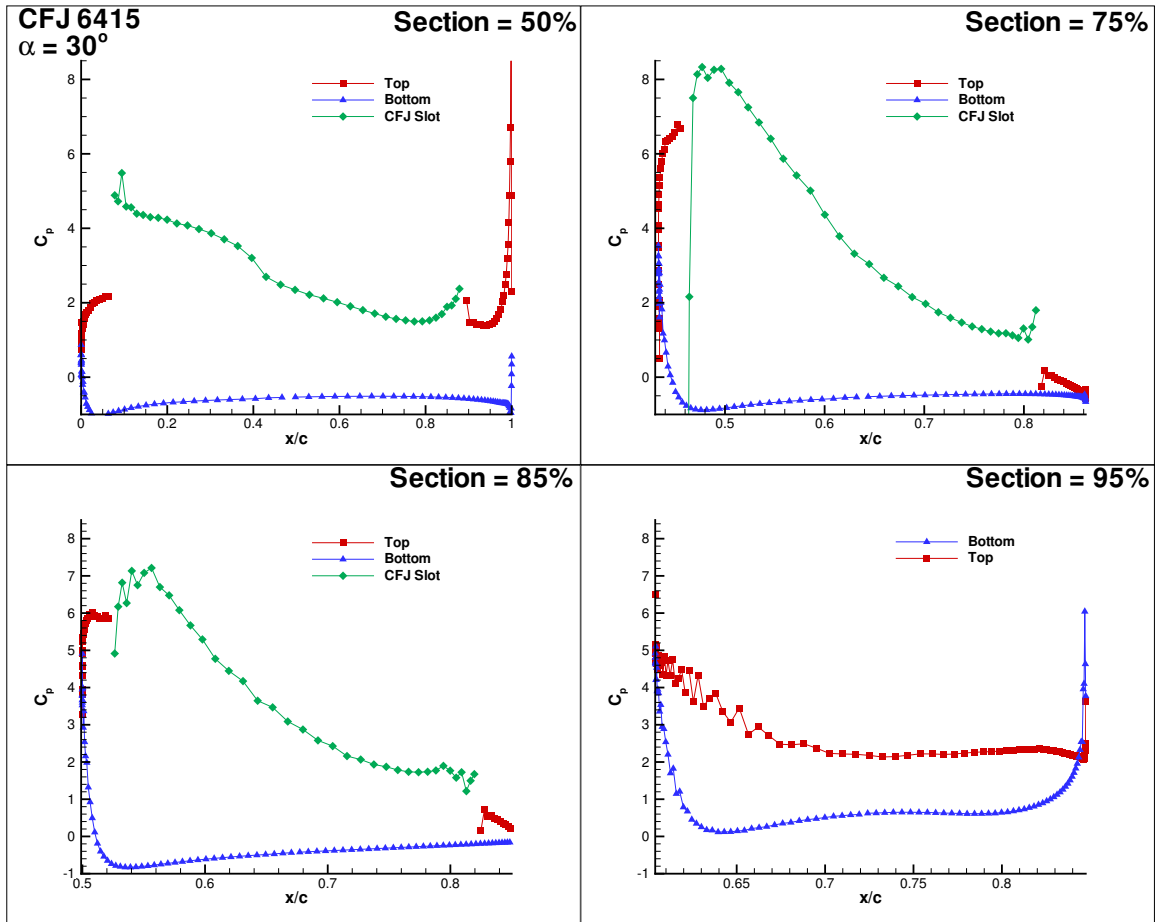
Figure 4.28: Pressure coefficient profiles for CFJ airplane at several span-wise locations for $\alpha = 30°$

Figure 4.29 shows the four views for the CFJ airplane at $\alpha = 30°$. From the flow field and streamlines it is apparent that flow separation has begun to occur. While the jet remains attached and highly accelerated, the sections above the jet are separating. Low pressure covers most of the frontal section of the airplane, while the high pressure stagnation point has moved well towards the center of the lower surface of the airplane. Wing-tip vortices seems to have weakened in the area immediately downstream of the trailing edge, but become stronger further downwind.

Figure 4.30 shows the C_p profiles for an angle of attack of $40°$. While loss of C_p, which denotes flow separation is not apparent within the CFJ section, where the jet is still strong enough to maintain attached flow, it is far more pronounced at the
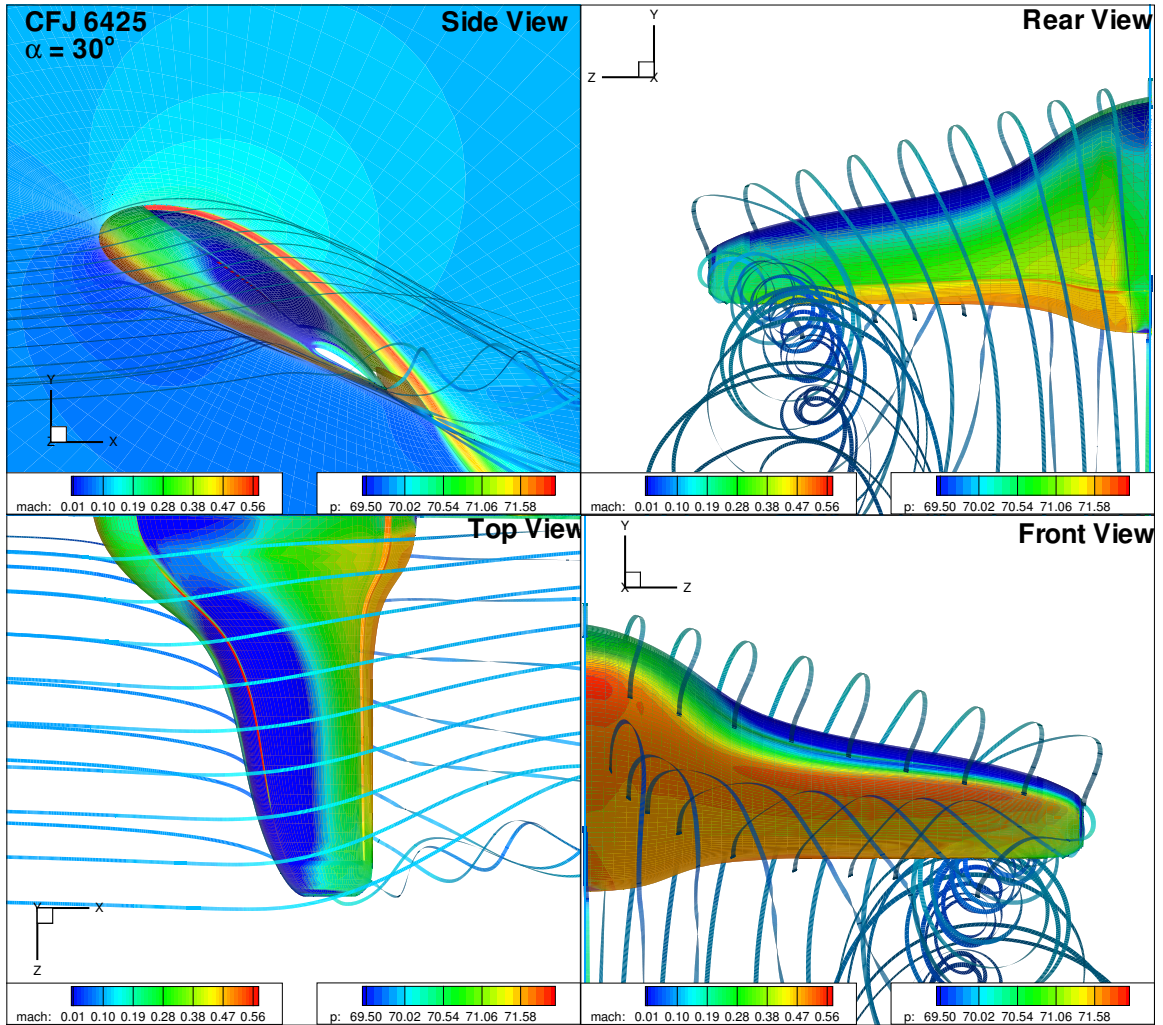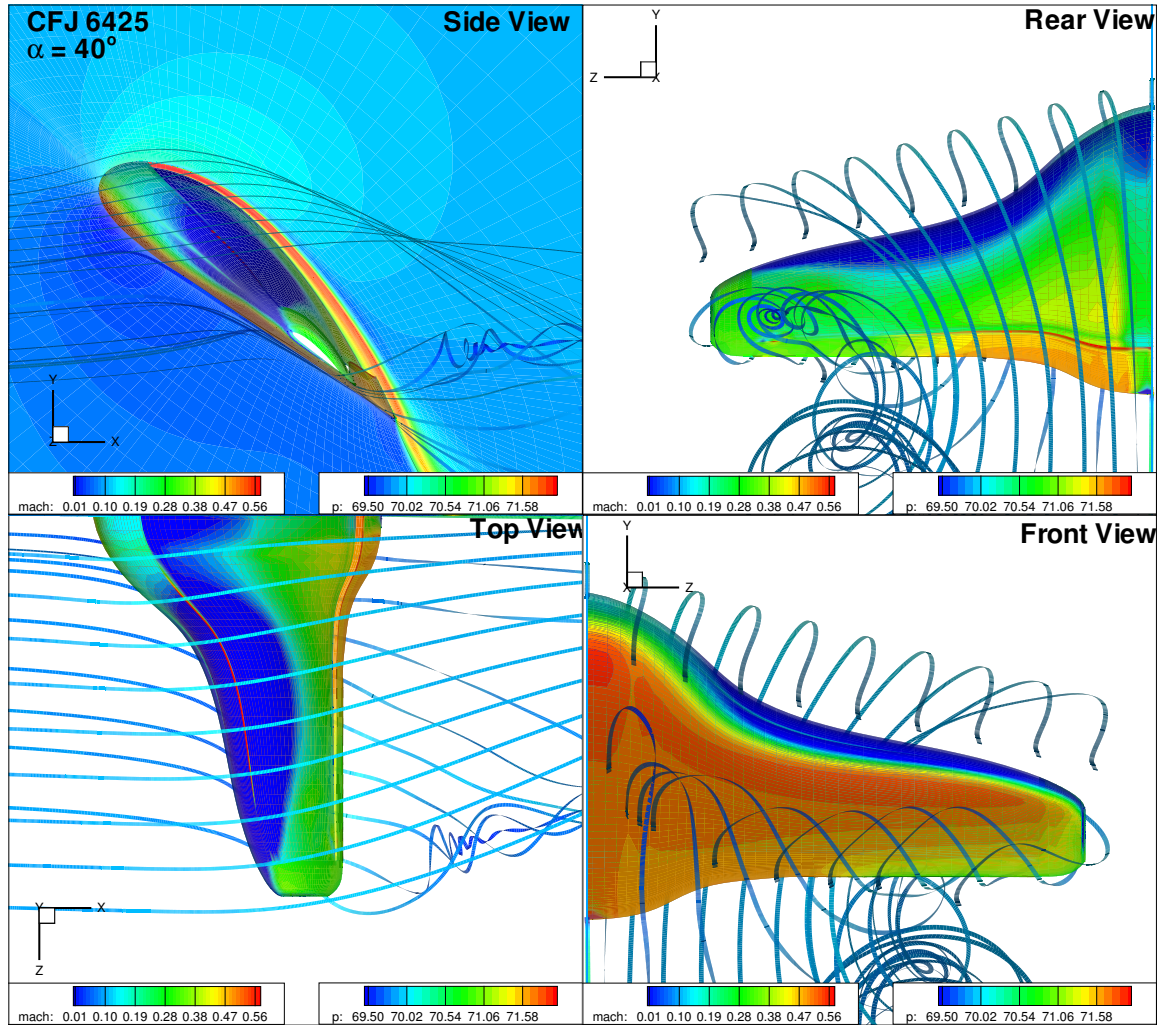
Figure 4.29: 3D surface pressure contours with Mach contours in mid-plane and 3D streamtraces for $\alpha = 40°$

wingtip, where C_p had dropped drastically from an average value of about 3.0 to an average value of about 1.0 on the upper surface. Peak C_p has increased to 0.9 in the still attached CFJ section.

Figure 4.31 shows Mach number isosurfaces at values of $M = 0.3$ and $M = 0.08$ for an angle of attack of $\alpha = 0°$. Note that the high velocity air flow in the wake has concentrated on a jet near the root of the wing. This accounts for the wakeshape seen in Figure 4.15. A small section of low velocity air is seen protruding from the rear section of the wing-tip, this section corresponds to the low velocity air at the
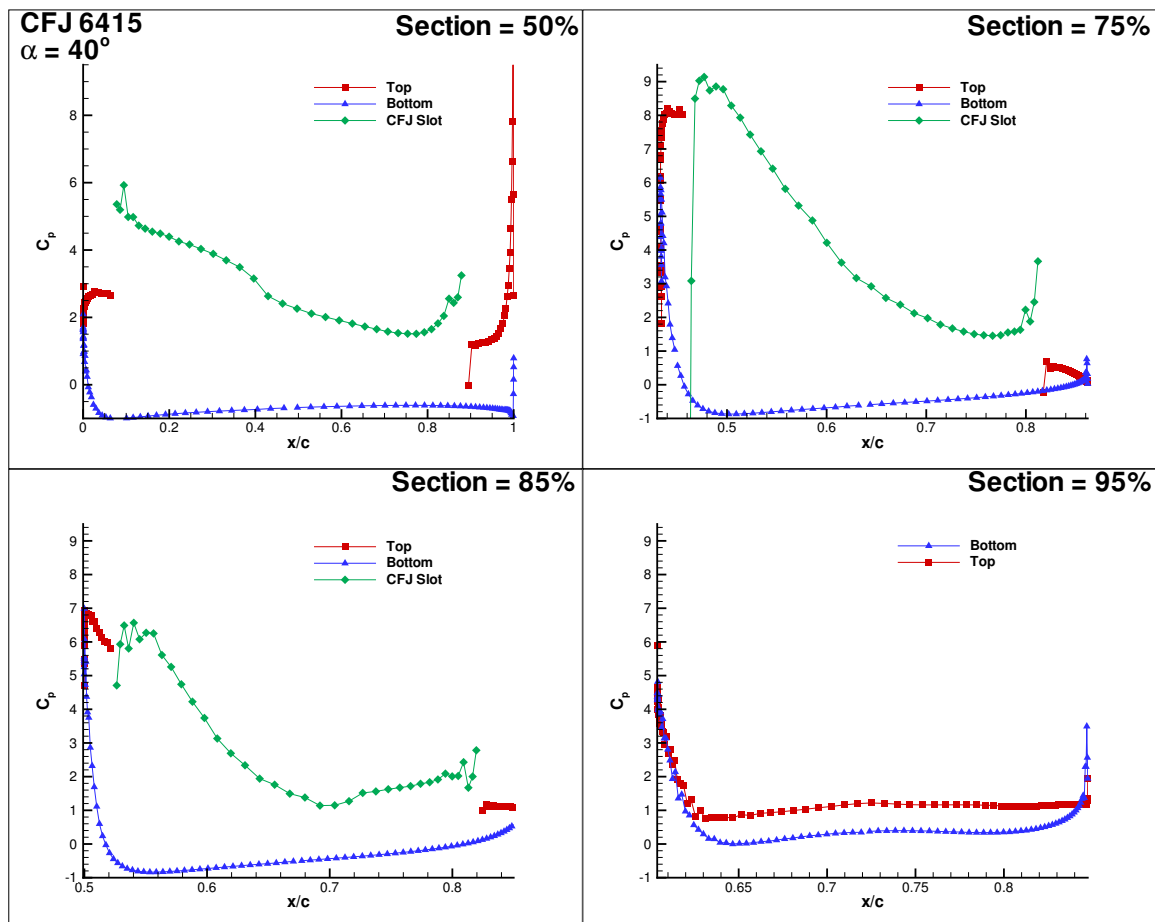
Figure 4.30: Pressure coefficient profiles for CFJ airplane at several span-wise locations for $\alpha = 40°$

core of the wing-tip vortex. A bubble of low velocity air is also seen at the leading edge, corresponding to the flow stagnation point, this area is most extensive at the root of the wing, where the chord is highest.

Figure 4.32 shows Mach number isosurfaces at values of $M = 0.31$ and $M = 0.08$ for an angle of attack of $\alpha = 10°$. The tube of high-velocity air at the root of the wing is still present, and in fact has become stronger. The high velocity surplus in the wake profile has become more restricted to the root section, as can be seen from Figure 4.16. The section of low velocity air emanating from the wingtip has now developed into a tube corresponding to the center of the now stronger wingtip vortex.

Figure 4.33 shows Mach number isosurfaces at values of $M = 0.3$ and $M = 0.07$
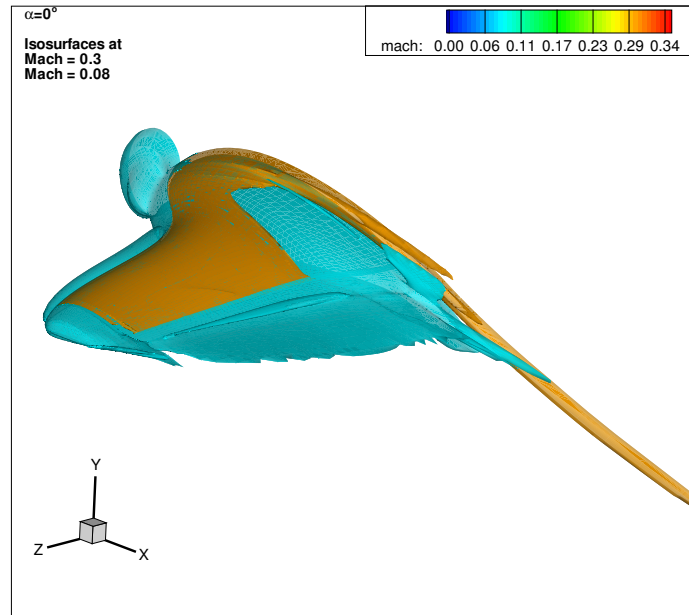
Figure 4.31: Mach isosurfaces for $\alpha = 0°$
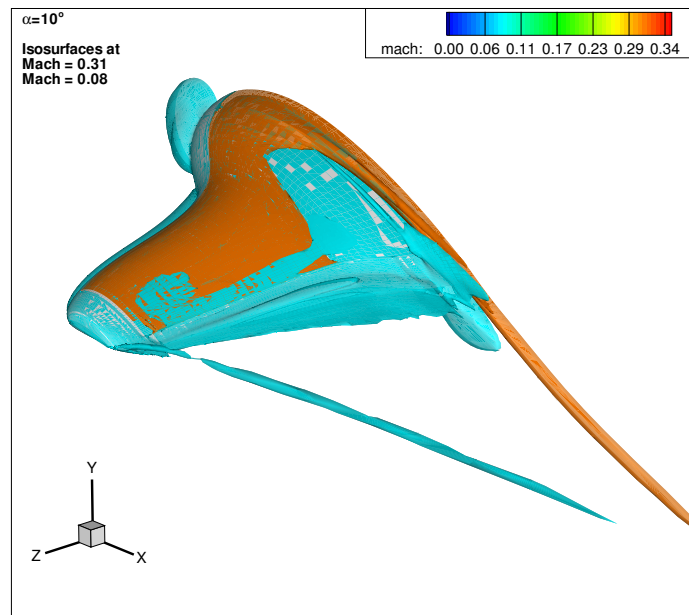
Figure 4.32: Mach isosurfaces for $\alpha = 10°$

for an angle of attack of $\alpha = 20°$. At this angle of attack, the high-velocity tube of air at the root section remains mostly unchanged. The wingtip vortex low-velocity tube, however, has become more extensive. This is indicative of a stronger wingtip
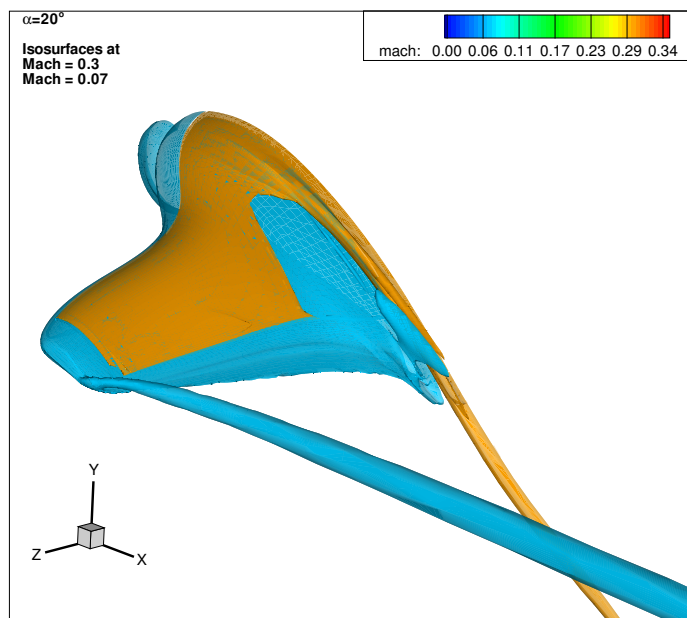
Figure 4.33: Mach isosurfaces for $\alpha = 20°$

vortex at this higher angle of attack, which can also be seen from the streamlines in Figure 4.25.
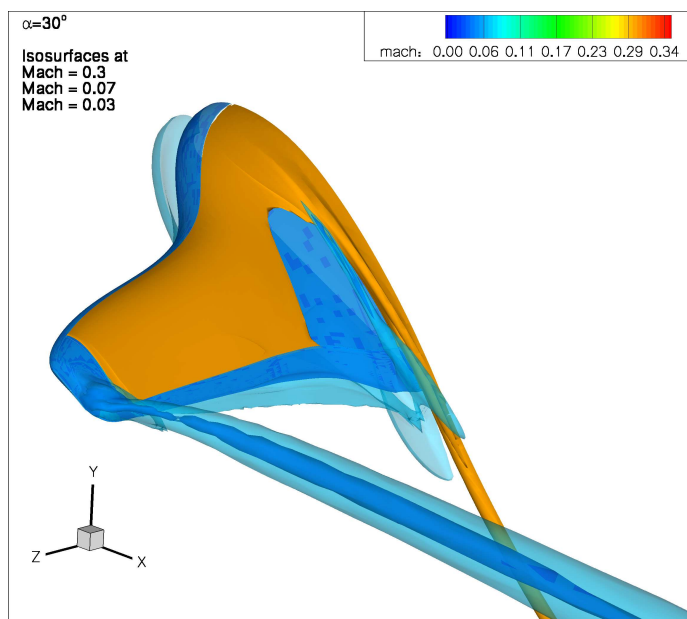
Figure 4.34: Mach isosurfaces for $\alpha = 30°$

Figure 4.34 shows Mach number isosurfaces at values of $M = 0.3$, $M = 0.07$,

and $M = 0.03$ for an angle of attack of $\alpha = 30°$. Even at this high angle of attack, the high-velocity tube of air remains strong and well attached. The wingtip vortex low-velocity tube has further expanded, which implied a much larger source of drag.
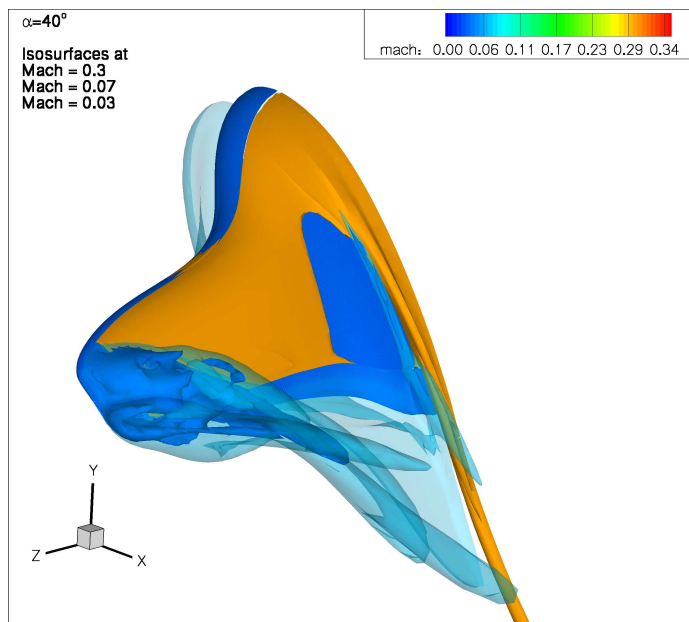
Figure 4.35: Mach isosurfaces for $\alpha = 40°$

Figure 4.35 shows Mach number isosurfaces at values of $M = 0.3$, $M = 0.07$, and $M = 0.03$ for an angle of attack of $\alpha = 40°$. The high velocity air at the root still remains attached. However, separation is beginning to occur at the wingtip. The isosurfaces in this region show a transition from a very laminar tube of air into a highly turbulent region. At this angle of attack, the flow is therefore beginning to stall. Figure 4.12 shows that at this angle of attack, a peak in C_L has been reached. At an angle of attack of $\alpha = 45°$, the flow has completely separated, and stall is occurring.

Chapter 5

CAARC Standard Tall Building Simulation

5.1 Background

The majority of testing of wind effects on buildings is presently performed within windtunnels on scaled models. While these tests can be reasonably accurate, and have become an invaluable tool in the design of high-rise buildings, they are still an approximation of the real case, and are dependent on the accuracy of the experimental setup. However, these wind tunnel tests have been shown to be more accurate than CFD models currently in use. Therefore, if CFD models can be developed which produce more accurate results to wind tunnel tests, it would be a step forward in the testing of wind effects on buildings. The problem lies in the highly turbulent and inherently separated fluid regimes associated with air flow around angular buildings, which are difficult to resolve using numerical methods. Accurate CFD models would provide a more economical alternative to wind tunnel testing, as well as giving engineers the oportunity to detect problems in design quicker, and thus lead to faster resolutions. It is therefore important to apply novel CFD models to building problems

as a step towards the developement of more accurate CFD and turbulence models for high-rise building design.

In keeping with this goal, the second major case analyzed within the present work is that of the Commonwealth Advisory Aeronautical Research Council standard tall building [33]. The CAARC tall building is used as a standard for high-rise buildings in the wind tunnel testing industry, particularly in Canada and other Commonwealth countries. The CAARC building has a height to width to depth ratio of 8 : 1 : 0.75 and is rectangular in shape.

As a part of the Miami Wind partnership between the University of Miami and RWDI, a leader in the wind engineering and building wind tunnel testing industry, CFD simulations are being performed for the CAARC building and will be compared to wind tunnel results carried out by RWDI.

5.1.1   Wind Tunnel Results by RWDI

Dragoiescu et al. [33] performed a wind tunnel analysis on a model of the CAARC building at RWDI's boundary layer wind tunnel facility in Guelph, Canada. A 1 : 400 scale model was used within a 2.4m × 2.0m test section. Measurements were gathered using both the High Frequency Force Balance (HFFB) and High Frequency Pressure Integration (HFPI) methods. RWDI provided the CFD Laboratory with information regarding their research, which was used to set up our CFD simulation of the CAARC building.

5.2   CFD Simulation

5.2.1   Mesh Generation for CFD

Initially, an H-mesh was chosen for the CAARC building case because such a shape has good compatibility with a rectangular geometry, such as is the case for the CAARC

building case. However, a convergent solution was not achieved using this mesh, and is was therefore discarded. Another attempt at simulating this case was made with a new O-type mesh, an approach which yielded convergent results. Such a mesh was chosen due to the symmetry in the building's geometry. The mesh was designed such that an area with a radius of 20 times the building width was captured. Blocks were split in the radial direction, radiating from the edges of the building. This can be seen in Figure 5.1.
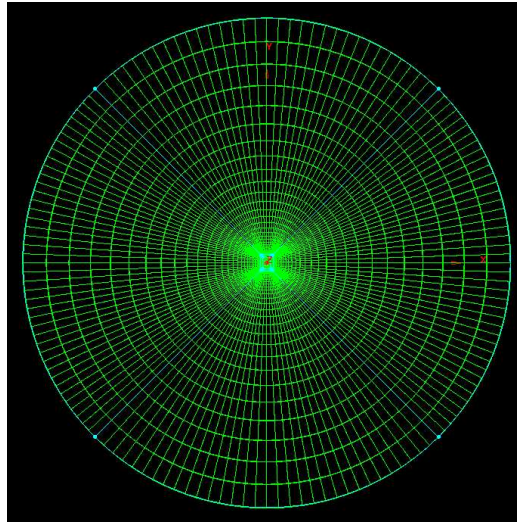
Figure 5.1: Top view of CAARC building mesh

Figure 5.2 shows the building mesh as seen from the front. It can be seen that a much higher distribution of points is given at the edges of the building walls, and a lower distribution is given towards the center of the building faces. The size of the finest mesh points, which are located along all wall boundaries including the ground is 0.024in.

Figure 5.3 shows a detailed cross-section of the mesh at the mid-plane of the building. The mesh was broken into a total of 9 blocks with dimensions given in Table 5.1.
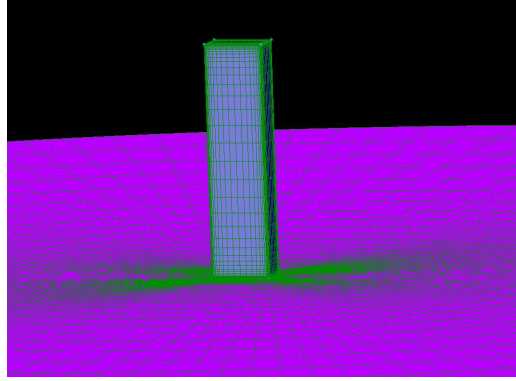
Figure 5.2: Front view of CAARC building mesh
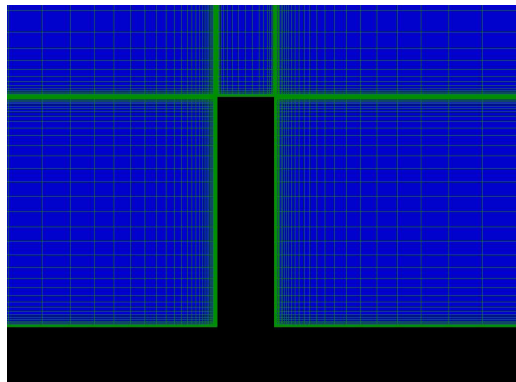
Figure 5.3: Cross-sectional detail of CAARC building mesh

5.2.2   CFD Pre-Processing

The CAARC building case was set up such that the main flow direction is directed towards the side of the building with the shortest width. The case was run at the conditions given in Table 5.2. Reference values are given relative to a building height of $182.88m$.

where p_{outlet} is given by Equation 4.6.

The computational values used to run this case can be seen in Table 5.3. This table also shows the number of time steps run, and the initial and final residuals.

block	section	size	number of cells
1	front face	43×70×67	201670
2	left face	33×70×67	154770
3	rear face	43×70×67	201670
4	right face	33×70×67	154770
5	front far field	43×70×67	201670
6	left far field	33×70×67	154770
7	rear far field	43×70×67	201670
8	right far field	33×70×67	154770
9	top face and far field	43×33×67	95073
total	-	-	1520833

Table 5.1: Block allocation for CAARC building mesh

Variable	Value
Mach	0.1
p_{outlet}	71.42857
p_{total}	71.92982
Reynolds	116000
T_{total}	1.002

Table 5.2: Flow conditions given in *datain* file for CAARC building case

Variable	Value
CFL	1.0
LHS Scheme	Zha 3
RHS Scheme	Van Leer
LHS Order	3
RHS Order	1
Turbulence Model	Baldwin Lomax
Time Steps	10000
Initial L2 Residual	0.125E-02
Final L2 Residual	0.829E-05

Table 5.3: Numerical parameters given in *datain* file and Residuals for steady 3rd order CAARC case

5.2.3 Boundary Condition Definition

The full boundary condition setup can be seen in the appendix, where the *datain* file is included in its entirety. The boundary conditions used for the CAARC Building

case are as follows:

- BC 1 - zero gradient used at the top far-field where flow is neither entering nor leaving the simulated region

- BC 3 - no-slip wall boundary given at all aircraft surfaces

- BC 6 - subsonic inflow used at the far-field where flow is entering the region

- BC 7 - interface boundary for MPI used at all block boundaries mirrored results

- BC 11 - subsonic outflow used at the far-field where flow is leaving the region

5.3   Results

Results have been achieved for the CAARC building under a steady state third order simulation. Work is under way to complete a steady state fifth order simulation, and to expand to the unsteady case.

5.3.1   Third Order Simulation

Since the CAARC building case, by its very nature, is an unsteady case, the steady-state results founds from this simulation are to be taken strictly as preliminary results. To fully capture phenomena such as vortex shedding, a higher-order unsteady case should be considered. However, the results which can be seen here can be used as a preview of the final, unsteady results. In fact, some indications of vortex shedding can be seen from the steady state simulation.

Figure 5.4 shows an isometric view of CAARC building results with streamlines and dimensionless surface pressure ($\bar{p}$) contours. The streamlines themselves are given Mach number contours. A large area of separation and recirculation can be seen behind the building. This is expected due to the rectangular shape of the building,
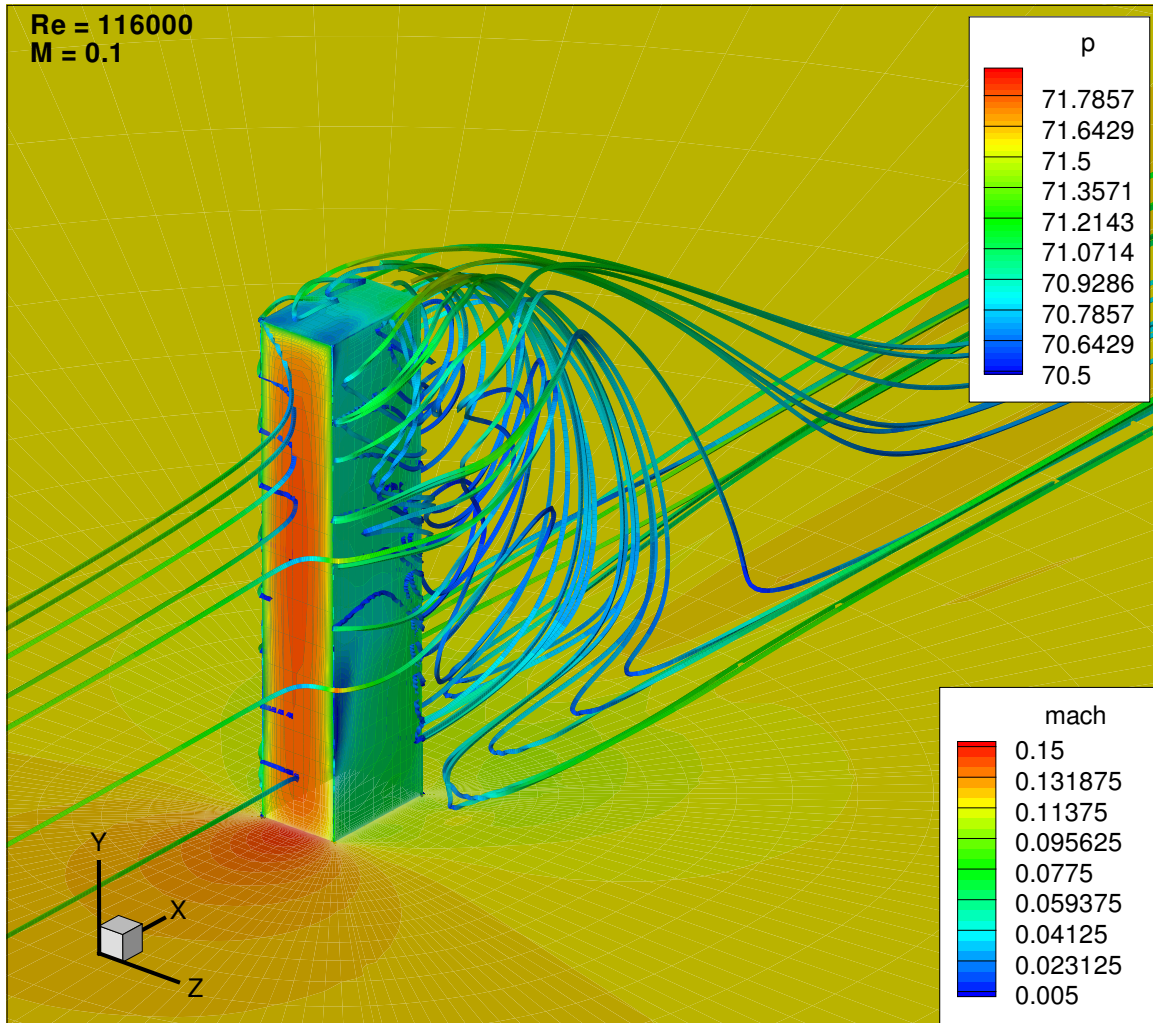
Figure 5.4: Isometric view of CAARC building with streamlines and surface pressure contours

which is not streamlined. The highest surface pressures can be found at the front face of the building, where flow stagnation occurs as the incoming flow encounters the building walls.

Figure 5.5 shows the front view of the CAARC building with streamlines and surface pressure contours at the same levels as shown previously. Incoming streamlines stagnate upon making contact with the front face of the building, at which point they diverge in all directions in a mostly symmetric fashion. Streamlines at higher levels of the building separate move further away from the wall than those closer to the ground.
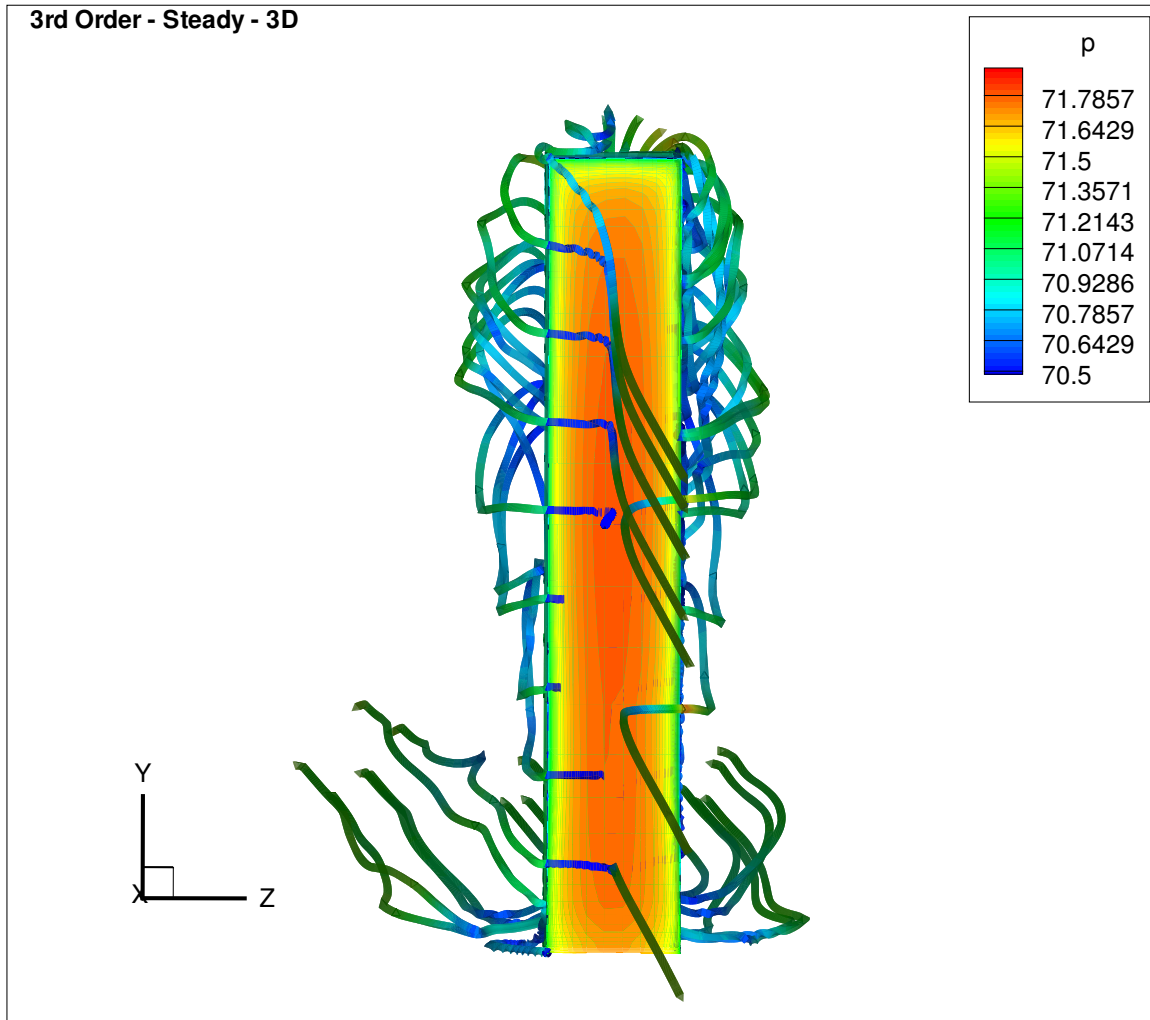
Figure 5.5: Front view of CAARC building with streamlines and surface pressure contours

The flow pattern around the building seems to have a mostly two dimensional profile for the lower third of the building height where it is restricted by the ground. However, it begins to become more three dimensional as it approaches the top of the building, where flow is free to move over as well as around it.

Figure 5.6 shows a rear view of CAARC building. In this plot, the highly separated region behind the building can be seen. It is interesting to note that the streamlines going over the building follow a narrow stream and later reattach near the ground level. That is, flow originating near the top of the building converges into a stream
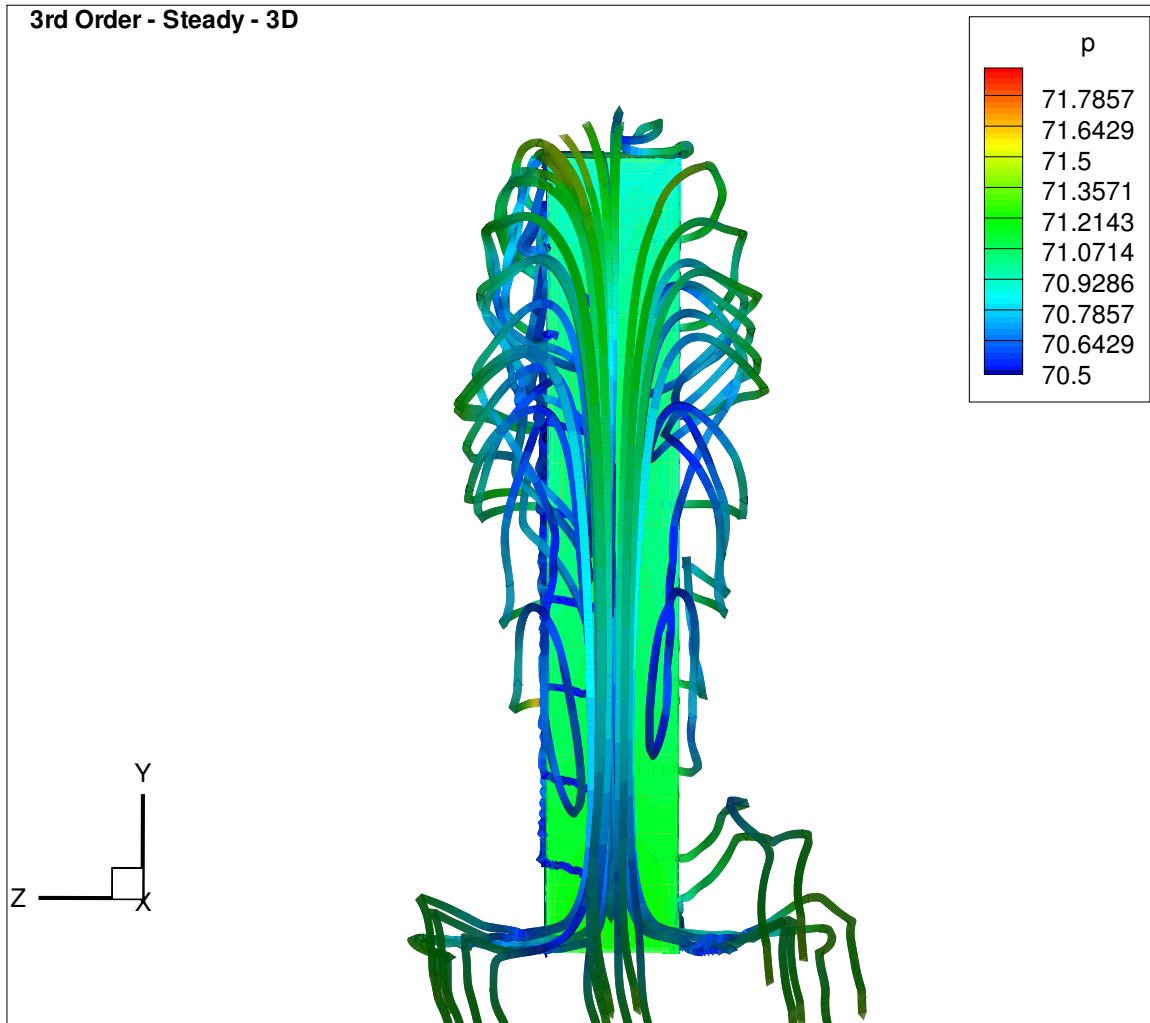
Figure 5.6: Rear view of CAARC building with streamlines and surface pressure contours

which eventually makes its way to ground level, where it once again diverges as it makes contact with the ground.

Figure 5.7 shows a side view of the flow field around the CAARC building. From this view, the separated region behind the building can be seen very clearly. Also, near the base of the building, small vortices can be seen forming at the point where the streamlines turn after encountering the front face of the building and move past the side wall. These vortices, however, do not continue to form at higher levels along the building height.
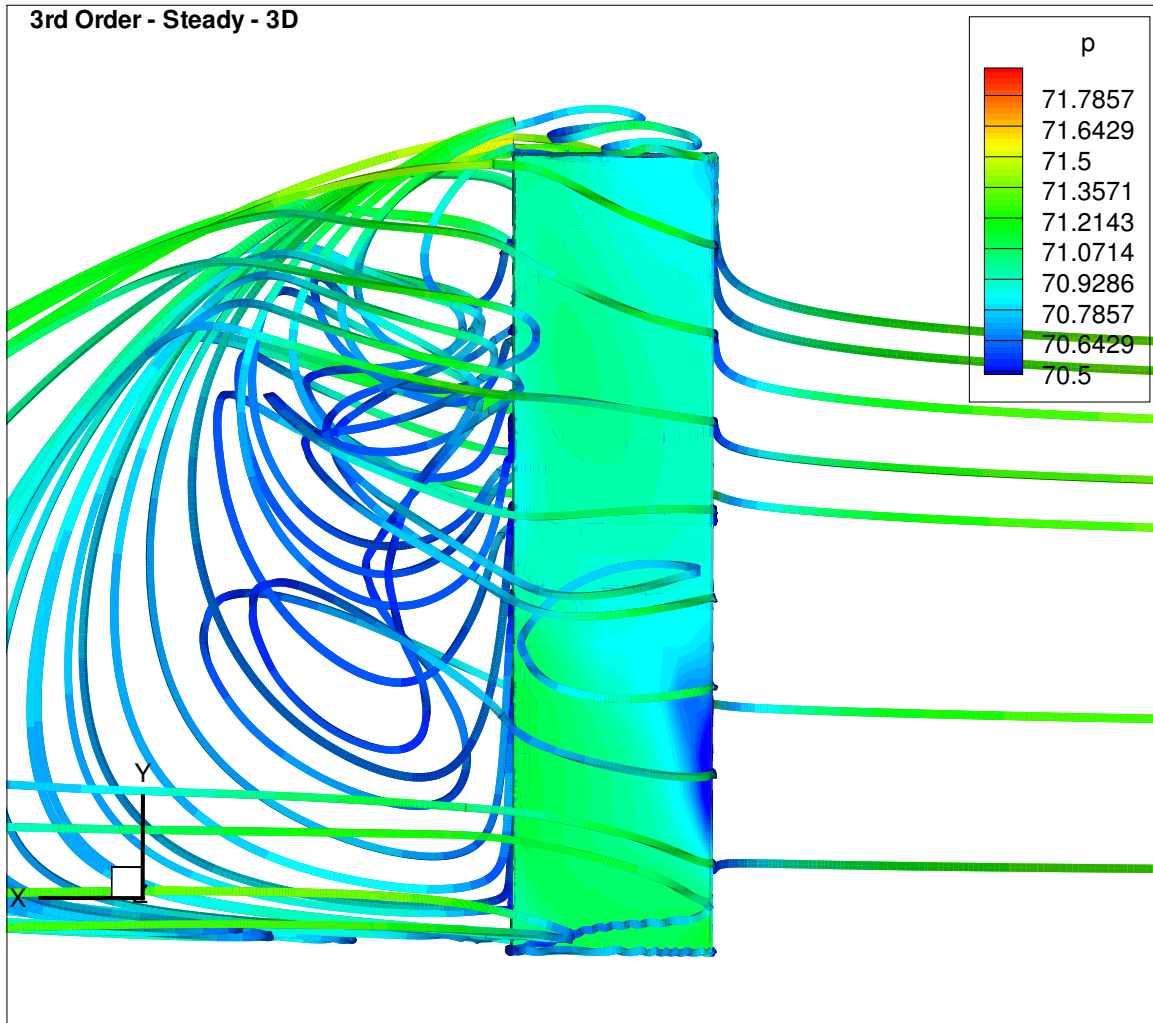
Figure 5.7: Side view of CAARC building with streamlines and surface pressure contours

Figure 5.8 shows the top view of the flow field around the CAARC building. From here, it can be seen that there are two main areas of circulation within the separated region. These two areas are separated from each other along the center of the back wall of the building. Stream velocity is lowest near the centers of these large vortexes. The top of the building shows lower surface pressures towards the front face of the building. This is due to the flow quickly turning in that region as it moves away from the stagnation point and over the top of the building, thus accelerating and lowering the pressure.
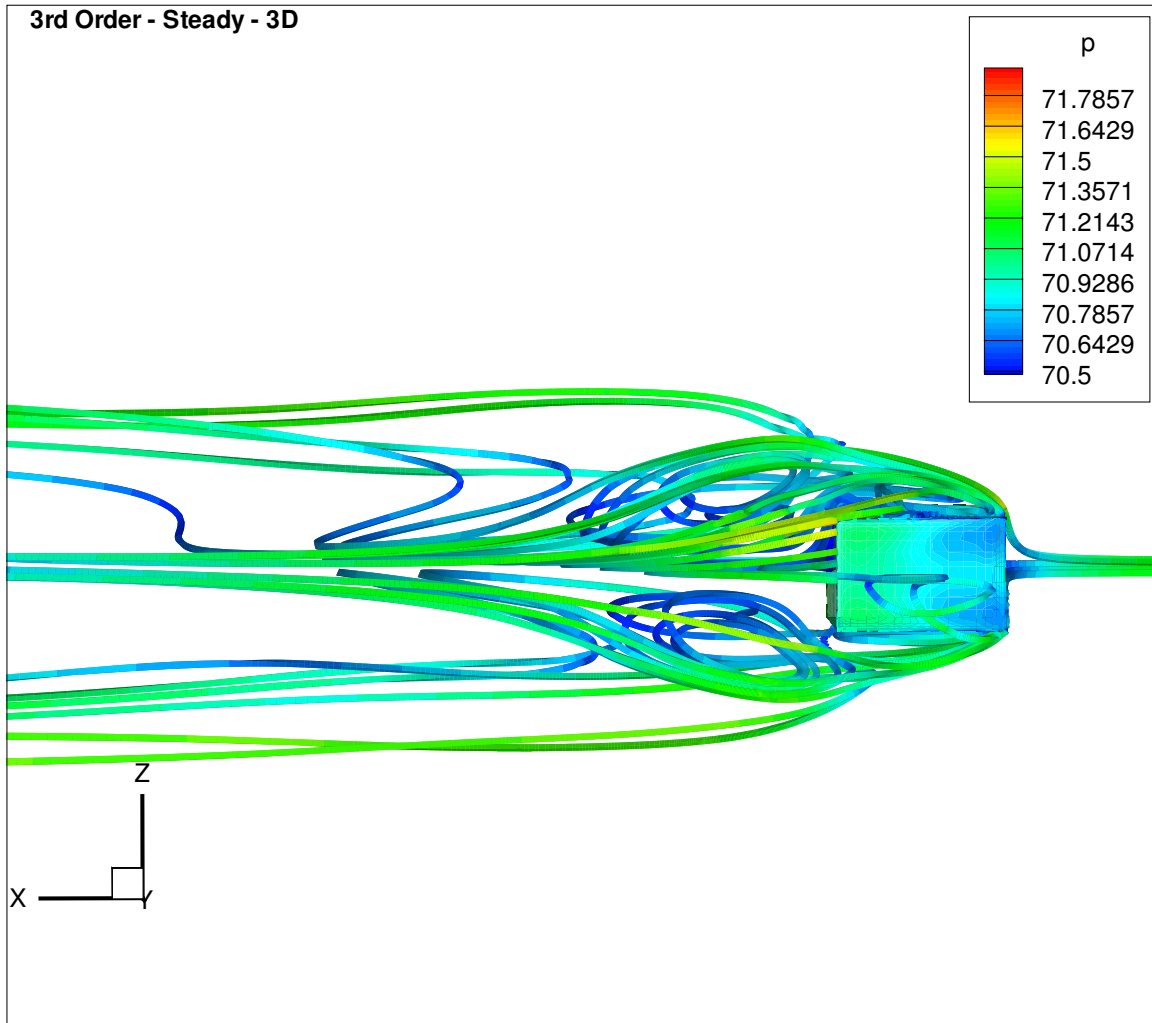
Figure 5.8: Top view of CAARC building with streamlines and surface pressure contours

Figure 5.9 shows Mach number contours at a y-direction slice at 50% of the building height. The two large vortexes at the separated region can be seen as two areas of low velocity flow. These two area are oblong in shape, and dissipate after a distance of about one and a half building heights behind the front face of the building. The separated region behing the building restricts itself to an area of about two building widths to either side of the building walls. This region is very narrow due to the high wind velocity. The highest wind velocities are seen emanating from the front face of the building to either side in the areas where flow is turning the front corners. At

Building - 3ʳᵈ Order Steady - 50% height
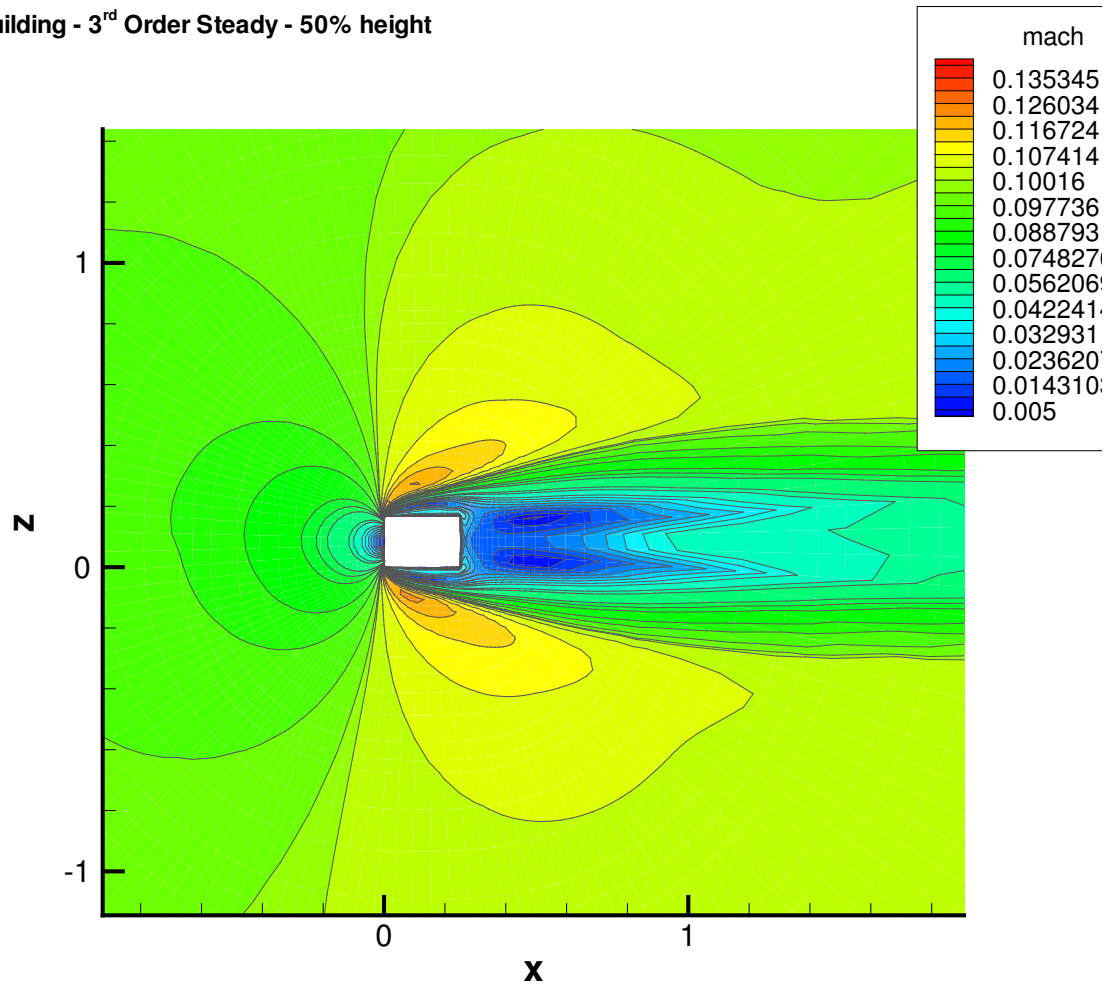
Figure 5.9: Mach contour slice at half-height for CAARC building

these areas flow is turning at a relatively high speed. However, the flow does not have enough energy and thus detaches at the corners.

Figure 5.10 shows pressure contours at the same level as the previous figure. Note that the pressure remains mostly symmetric along the wind direction axis. A high pressure area emanates from the stagnation point. On the areas adjacent to the side walls of the building the pressure in this section is very low compared to the front face. This very quick change in pressure would cause high structural stresses at this height level.

Figure 5.11 shows pressure contours at ground level. Alternating circular areas

Figure 5.10: Pressure contour slice at half-height for CAARC building

of low and high pressure are seen emanating from the sides of the building. The largest of the low-pressure area correspond to the two large areas of circulation in the separated region. These areas of alternating high and low pressure are reminiscent of vortex shedding. However, a steady-state solution is not sufficient to fully define these phenomena. This plot makes it clear that such phenomena, however, is likely to be occurring, and thus an unsteady simulation should be used to fully define them.

Figure 5.12 shows a constant-z slice of the flowfield around the CAARC building with Mach number contours at z=50%. This figure is very informative, as it shows how the relative velocity of the flow changes around the building in the direction of
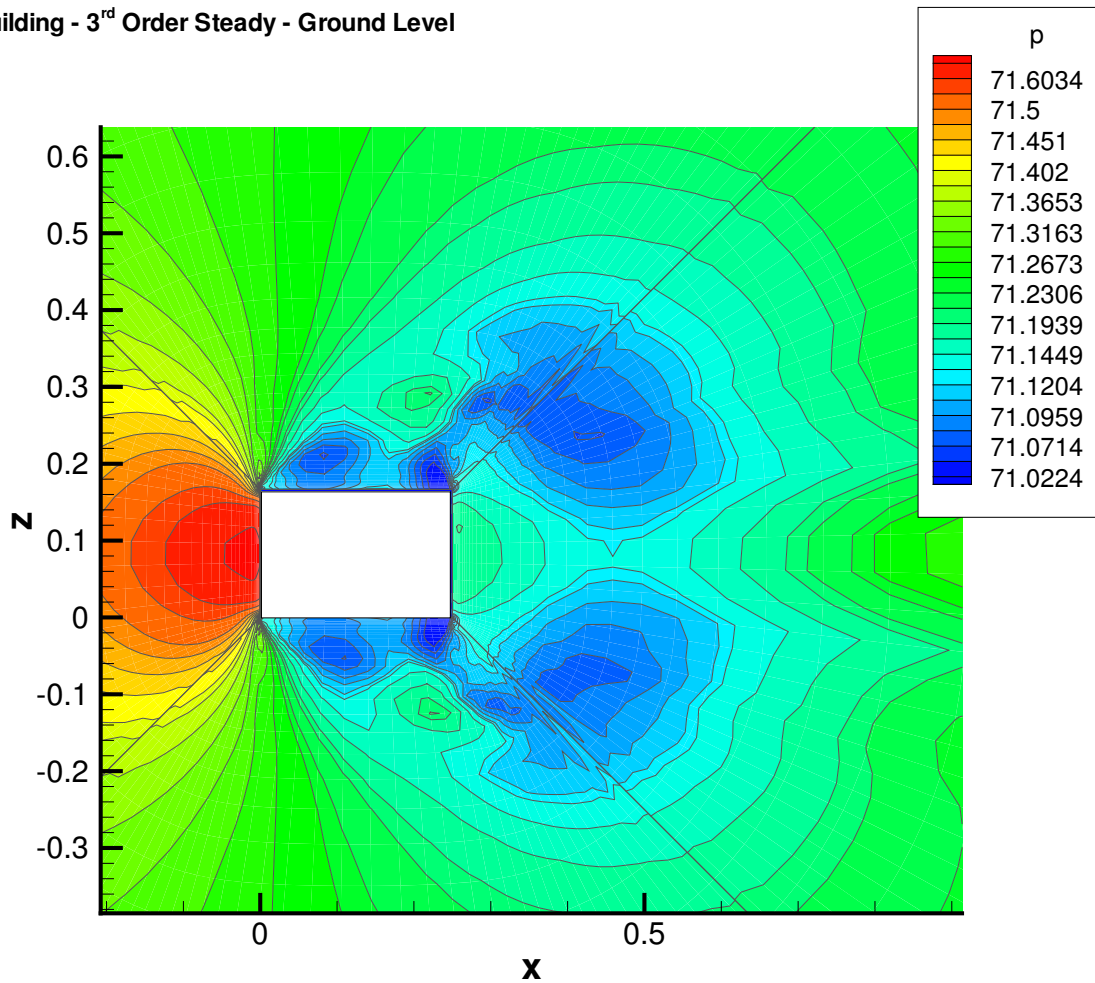
Figure 5.11: Pressure contour slice at ground level for CAARC building

the main flow. Flow is very slow in the separated region behind the building, but reaches a peak as it goes over the top of the building. Mach number remains high over a large area above and behind the building.

Figure 5.13 shows a constant-z slice of the flowfield around the CAARC building with dimensionless pressure contours. Pressure is highest in front of the building where flow is decelerating towards the stagnation point. Pressure is lowest above the building where flow is accelerating and quickly turning, as well as in the separated region behind it. There is a local area of higher pressure along the rear wall near ground level. This local change is due to the flow slowing in that area as it encounters

Building - 3rd Order Steady - 50% slice - N-S
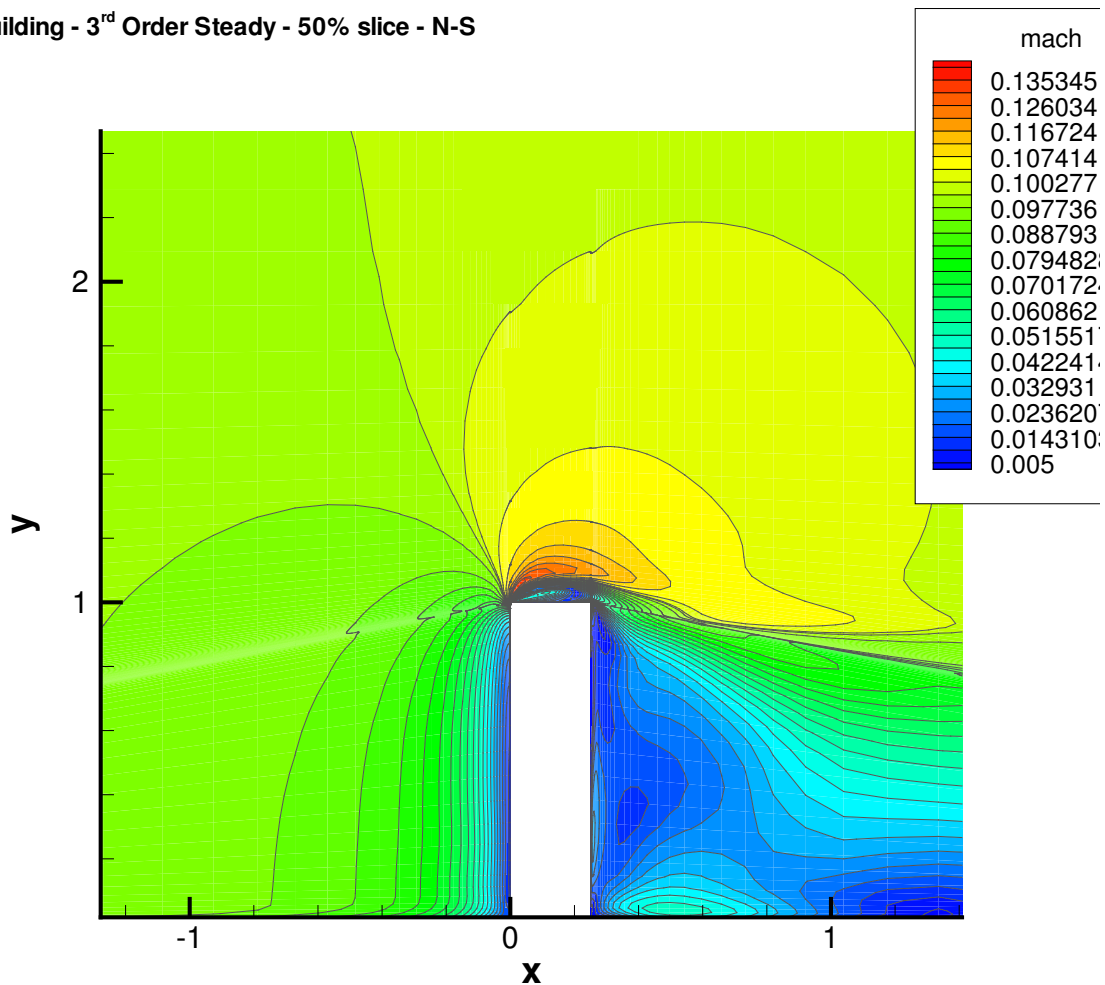
Figure 5.12: N-S slice at mid-plane for CAARC building showing Mach contours

the ground, where it is forced to turn.

Figure 5.14 shows a three-dimensional view of the building with surface pressure contours at all wall boundaries, including the ground. This figure illustrates the great difference in surface pressures experienced by different walls depending on their orientation with respect to the main flow direction. There are also some local changes in pressure within the same wall. One such case is seen at a height range of approximately 20-50% of the total building height, there is a very quick local drop in pressure in the side walls towards the front of the building. This high pressure gradient is likely to lead this section of the building to experience the highest wind loads.

Figure 5.13: N-S slice at mid-plane for CAARC building showing pressure contours

Figure 5.15 shows a similar view of the building, but from a rear vantage point. The low pressure area that was seen at the opposite wall at the 20-50% height range can be also seen here in the oposite wall at the same range. This similarity is expected due to the symmetry inherent in the unsteady simulation.
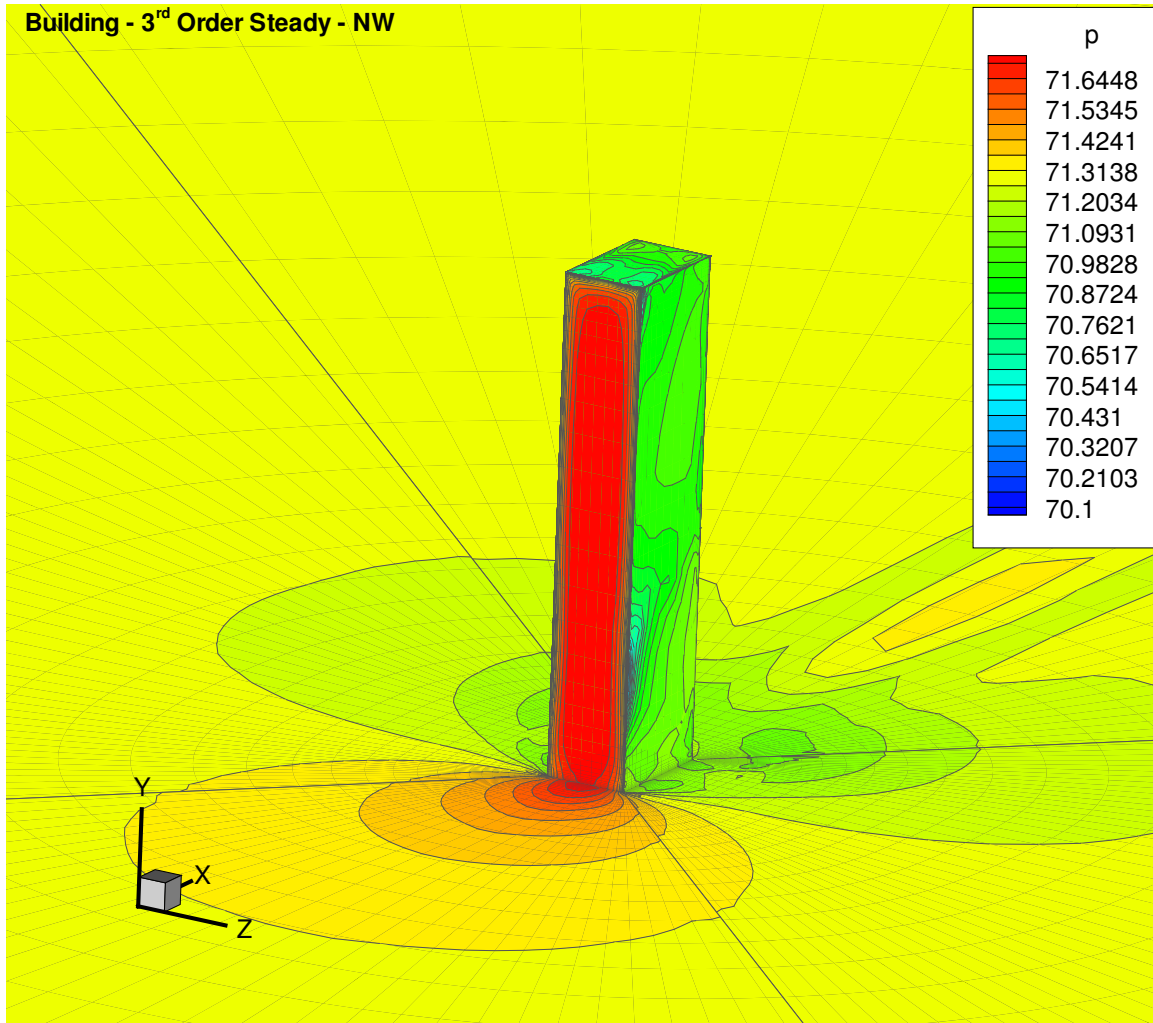
Figure 5.14: NW view of CAARC building showing surface pressure contours

Pressure Distributions

In this section, detailed pressure coefficient (C_p) plots are given for the four walls of the CAARC building. The North wall corresponds to the side facing the wind, while the South wall corresponds to the side facing away from it. The West and East walls are chosen respectively.

Figure 5.16 shows the C_p distributions at different height levels on the CAARC building's North wall. C_p values on this wall range from -0.65 to 0.65, these low values indicate that pressures on this wall are relatively high because, as can be seen
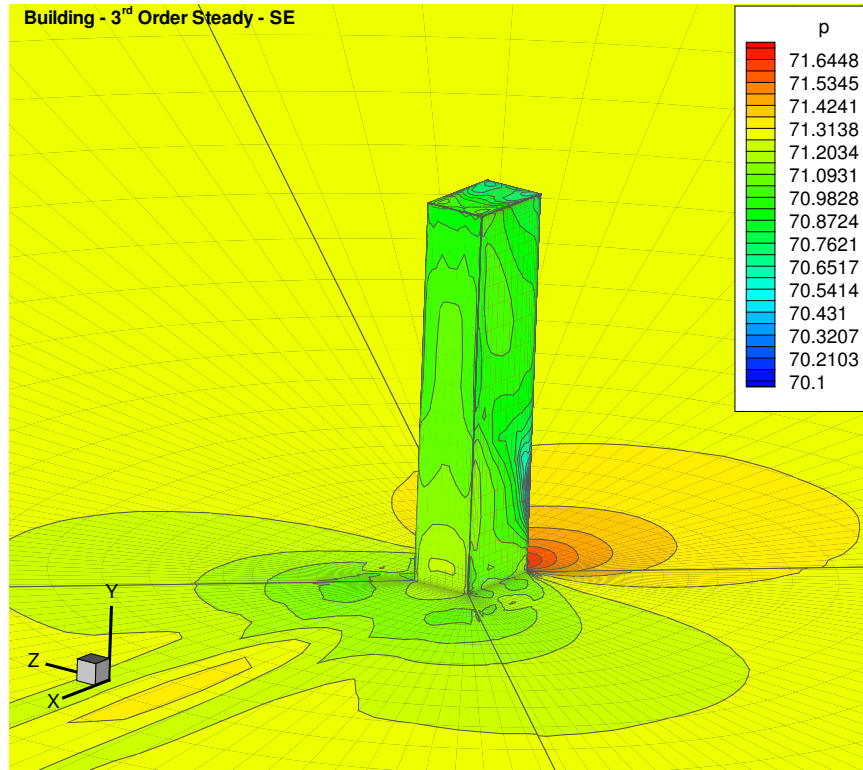
Figure 5.15: SE view of CAARC building showing surface pressure contours

from Equation 4.9, there is an inverse relation between the pressure coefficient and the pressure. These results are expected because the North wall contains the flow stagnation point, and thus should be experiencing high pressures. Both the shapes and values of C_p in the 0% to 60% range are very similar, indicating that there is very little change in pressure distribution over the lower section of the building. The pressure distribution along the lower section of the building can therefore be said to be close to two dimensional, something which can be verified by examining the streamline pattern in Figure 5.5. At 50% height, however C_p values at the corners of this wall are beginning to increase slightly, flattening the shape of the profile. At 70% height, the shape of the distribution has become even flatter, and the average C_p value has increased to about 0.1. At 100% height, the profile has become completely linear at a value of $C_p = 0.3$.

Figure 5.17 shows the C_p distributions at different height levels on the CAARC
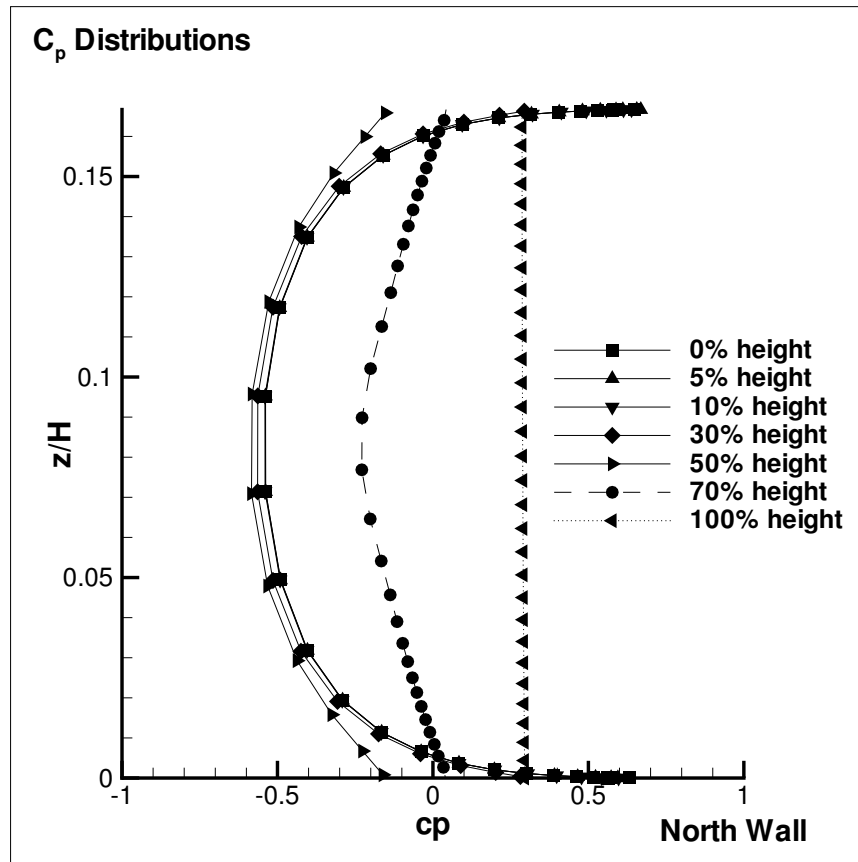
Figure 5.16: Surface pressure coefficients at different heights of the North wall of the CAARC building

building's South wall. C_p values on this wall range from -0.25 to 0.75, these values are higher than those of the North wall and indicate that pressures on this wall are low. This is also expected, as the South experiences low-energy separated flow. Once again, the profile shapes are roughly two dimensional over the lower section of the building, but begin to change quickly after about 30% height. At 50% height, the C_p values at the corners of this wall are beginning to increase slightly. At 70% height, the shape of the distribution has changed completely, becoming flatter. C_p values have experience an overall increase. At a height of 100%, the shape of the profile has become very flat, with minor fluctuations near the center. Values have decreased significantly over all other sections.
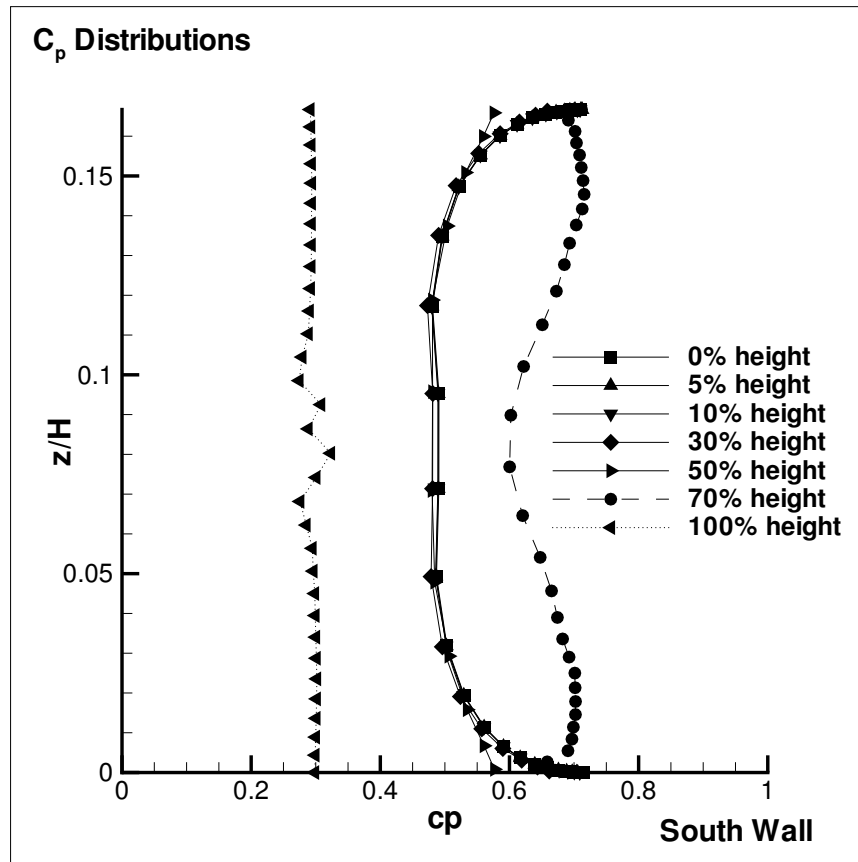
Figure 5.17: Surface pressure coefficients at different heights of the South wall of the CAARC building

Figure 5.18 shows the C_p distributions at different height levels on the CAARC building's West wall. In this wall, like the two previous ones, the shape of the C_p distributions at the lower section of the building changes little. At 30% height a slight change is seen at the very corner where the West and North walls meet. The C_p value there has dropped from 0.8 to 0.45, with little change elsewhere along the wall. At 50% height however, that value has further dropped to about 0.2, and the section of low pressure has extended further along the wall, returning to values close to its previous distribution at $x/H = 0.05$, where H is the total building height. At 70% height, the distribution has changed drastically over lower levels. The value of C_p at the North side of the wall had dropped further to about 0.07, while the shape of the
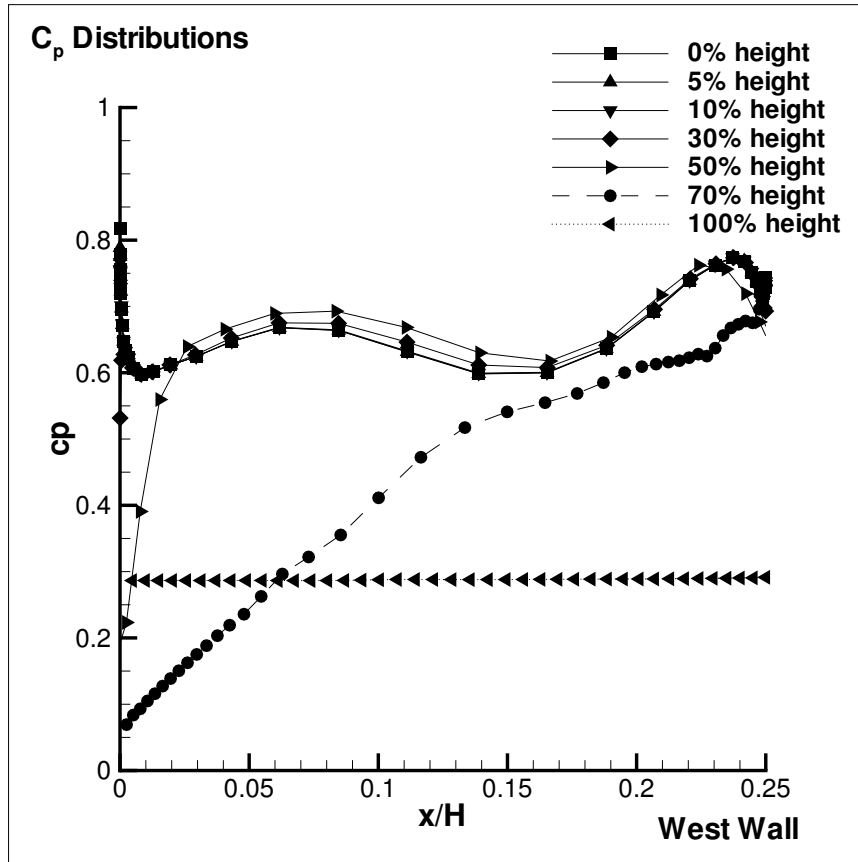
Figure 5.18: Surface pressure coefficients at different heights of the West wall of the CAARC building

distribution has become more linear. At a height of 100%, the shape of the profile has become completely flat, at a level of $C_p = 0.29$.

Figure 5.19 shows the C_p distributions at different height levels on the building's East wall. Both the shape and values of the C_p distribution on this wall are very similar to that of the West wall. This symmetry is due to the steady-state computation. An unsteady state case would be expected to show more asymmetry. The final equilibrium value achieved at the top of the building is of about $C_p = 0.3$.
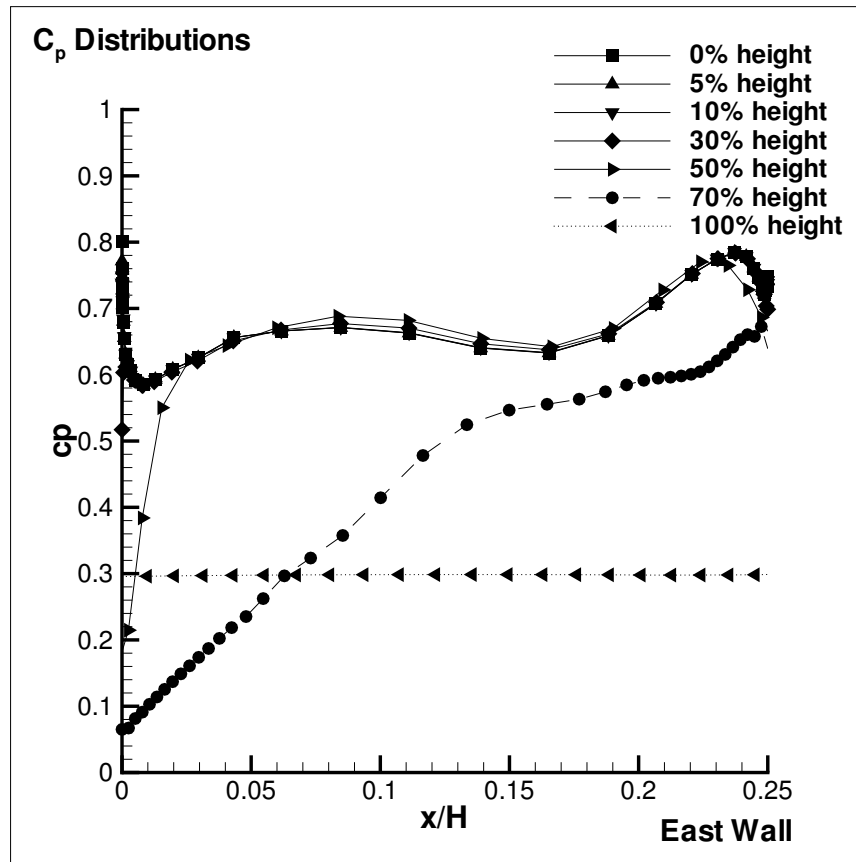
Figure 5.19: Surface pressure coefficients at different heights of the East wall of the CAARC building

5.3.2 Fifth Order Simulation

A steady-state fifth order simulation is the CAARC building is currently being performed. Results at this time are preliminary, and subject to change. However, these results, once finalized will constitute the next step in the simulation of the CAARC building using the FASIP CFD code. The unsteady simulation should be able to capture effects of aerodynamic instability, such as vortex shedding, which have major effects in the structural forces felt by the building.

5.3.3 Continuing Work

The present work will be continued by students at Dr. Gecheng Zha's CFD Laboratory. Future work includes expanding results to include varying wind directions, wind speeds, as well as finalizing the 5th order and unsteady simulations.

Chapter 6

Conclusions

The present thesis has attempted to study a new type of aircraft using the novel CFJ technology in order to vastly improve performance over conventional aircraft. The CFJ airfoil introduces an injection slot near the leading edge of the airfoil, and a suction slot near the trailing edge. High velocity air is then circulated between these two slots. In doing so, energy is added to the boundary layer, increasing turbulent mixing and thus allowing flow to remain attached even at angles of attack as high as 45°. It has been shown that the addition of the CFJ airfoil to a baseline aircraft increases lift and stall margin, reduces drag, and even at an operational range of angles of attack, creates a net thrust without the use of conventional engines. The FASIP CFD tool developed at the University of Miami was used to verify the design. A Riemann solver based on Zha's flux vector splitting scheme was used. CFD results have verified that the increase in performance is significant, and therefore, future research concerning the subject should be conducted to further the technology. The case of a building under high wind conditions has also been analyzed, although results are preliminary and necessitate continuation. An unsteady-state simulation would serve to better capture the phenomena such as vortex shedding, which can compromise structural integrity.

CFD analysis has been the main tool utilized in the present work to simulate complex geometries under different flow conditions using a code which, while under constant development, has been shown to conform very well to experimental and analytical results [12, 29, 30, 33, 34]. The results achieved in the present work can therefore be said to have a high fidelity, and constitute reasonable proof of concept.

Improvement in the design of the CFJ Airplane over conventional aircraft, such as the use of the CFJ airfoil cross-section and a Flying Wing configuration have been shown to have a significant positive impact on the performance of an aircraft. Due to the energy which the CFJ imparts to the incoming flow, it is capable of maintaining attached flow even under extremely adverse conditions. This has been verified for several two and three dimensional designs both by experiments and CFD results [34, 35]. The FW configuration also leads to an increase in efficiency over a more traditional aircraft design [1–4]. The CFJ airplane is also capable of producing a net thrust under certain conditions. These results imply that the main propulsion system of such an aircraft could be significantly downsized. It might even be possible to use a CFJ device alone to power a small lightweight aircraft. This would constitute a more efficient propulsion system than is currently in use by integrating the lift production and drag opposing systems of an aircraft. Such a radical redesign of the basic aircraft configuration could be considered to be a paradigm shift, and could lead to safer, more efficient, and more silent aircraft in the future.

Appendix A

Input Files for CFD Computation

A.1 CFJA Case *datain* File

```
&consts
delta        = 0.0d+00, 0.0d+00, 0.0d+00, 0.0d+00, 0.0d+00,
epsfactor    = 1.00d-06, ! epsilon used in linear reconstruction
gamma        = 1.40d+00, ! Ratio of specific heats
prandtl      = 0.72d0,   ! Molecular Prandtl number
prt          = .9d0,     ! turbulent prandtl number
suther       = T,        ! = T: Sutherlands Law. = F: mu = T
tref         = 0.43d0,   ! Non-dimensional ref temperature in Sutherland
/

&flows
angl1        = 0.0d0,    ! inlet angle 1
angl2        = 0.d0,     ! inlet angle 2
inviscid     = F,        ! = T: inviscid
machinf      = 0.10000d0 ! Mach no. based on U_infinity and a_infinity
poutlet      = 71.42857, ! outlet static pressure
ptotal       = 71.92982, ! Total pressure at inlet
reynolds     = 2000000.0 ! Reynolds number
tintvl       = .05,      ! unsteady time interval
ttotal       = 1.002,    ! Total temperature at inlet
turb         = 1,        ! BL turbulence viscosity inclded when 1
/

&comp
blen         = 2,        ! the number of the layer of the ghost cell
```

```
idimen     = 3,          ! = 1: 1-D, = 2: 2-D, = 3: 3-D
nl         = 5,          ! No. of equations
choice     = 'y'         ! ='y': from rstore. ='n': from initial value
cfl        = 10.00d0     ! CFL number
checksteps = 1,          ! print out status every # steps for monitoring
dual_t     = 0,          ! 1: unsteady, 0: steady
eps        = 1.d-15,     ! residual limit
gcl        = 0,          ! geometry conservation in moving grid
                         ! 0 - disabled
                         ! 1 - enabled
integrate  = 4,          ! =1: AF; =2: R-K, 3: Euler, =4: GS
intersteps = 50,         ! save results every # steps in steady state
                         ! computation
iter_gs    = 2,          ! number of Gauss-Seidel Iterations
kfactor    = 0.33333d0,  ! factor in linear reconstruction
lhs_order  = 0,          ! =0, 1st order MUSCL for LHS matrices;
                         ! =1, 2nd or 3rd order.
lhs_scheme = 4,          ! =1, Roe; =2, Zha;=3, none, =4, Van Leer
limiter    = 0,          ! =0, no limiter; =1, MINMOD ; =2, SUPERBEE
moving     = 0,          ! moving grid, 0-stationary, 1-fixed, 2-induced
nrbc_ex    = 0,          ! =3: use Euler Method non-reflective BC at exit
                         ! =0: no NRBC at exit
nstep      = 7500,       ! No. of time steps
rhs_order  = 1,          ! =0, 1st order MUSCL for RHS
                         ! =1, 2nd or 3rd  order
rhs_scheme = 2,          ! =1,Roe
                         ! =2,Zha2
                         ! =3,AUSM+
                         ! =4,Van Leer
                         ! =5,VL-Hanel
                         ! =6,Zha6
                         ! =7,AUSMV
                         ! =8:Zha
                         ! =9:AUSMD
strtp      = 0,          ! 1-cylinder, 2-airfoil
tsteps     = 2,          ! unsteady time marching stes using dual-time
                         ! stepping
unidt      = 0,          ! Uniform time interval in whole domain when > 0
velinit    = 1.d0,       ! dimensionless velocity initial value
strm_dir   = 1,          ! main flow direction
theta      = 0.d0,       ! initial velocity angle
twpar      = 2,          ! 1<=twpar<=10, initial for omega when nl=7
tkpar      = 5,          ! 2<=tkpar<=5, initial for k when nl=7
xyz        = 0,0,0,      ! when moving >0
vbd        = 0,0,0
```

```
/

&bcdef bcdir='xie',block=1,bctype=7,start=1,1,1,end=1,64,114,
       iblock=7,istart=24,1,1,iend=24,64,114,order=1,2,3/
&bcdef bcdir='xie',block=1,bctype=7,start=29,1,1,end=29,64,114,
       iblock=2,istart=1,1,1,iend=1,64,114,order=1,2,3/
&bcdef bcdir='eta',block=1,bctype=3,start=1,1,1,end=29,1,50/
&bcdef bcdir='eta',block=1,bctype=7,start=1,1,51,end=24,1,114,
       iblock=7,istart=24,1,51,iend=1,1,114,order=1,2,3/
&bcdef bcdir='eta',block=1,bctype=7,start=25,1,51,end=29,1,114,
       iblock=6,istart=24,1,51,iend=20,1,114,order=1,2,3/
&bcdef bcdir='zta',block=1,bctype=6,start=1,1,114,end=29,64,114/
&bcdef bcdir='zta',block=1,bctype=8,start=1,1,1,end=29,64,1/

&bcdef bcdir='xie',block=2,bctype=7,start=38,1,1,end=38,64,114,
       iblock=3,istart=1,1,1,iend=1,64,114,order=1,2,3/
&bcdef bcdir='eta',block=2,bctype=7,start=1,1,1,end=38,1,40,
       iblock=8,istart=1,20,1,iend=38,20,40,order=1,2,3/
&bcdef bcdir='eta',block=2,bctype=3,start=1,1,41,end=38,1,50/
&bcdef bcdir='eta',block=2,bctype=7,start=1,1,51,end=19,1,114,
       iblock=6,istart=19,1,51,iend=1,1,114,order=1,2,3/
&bcdef bcdir='eta',block=2,bctype=7,start=20,1,51,end=38,1,114,
       iblock=5,istart=24,1,51,iend=6,1,114,order=1,2,3/
&bcdef bcdir='eta',block=2,bctype=6,start=1,64,1,end=17,64,114/
&bcdef bcdir='eta',block=2,bctype=11,start=18,64,1,end=38,64,114/
&bcdef bcdir='zta',block=2,bctype=6,start=1,1,114,end=19,64,114/
&bcdef bcdir='zta',block=2,bctype=11,start=20,1,114,end=38,64,114/
&bcdef bcdir='zta',block=2,bctype=8,start=1,1,1,end=38,64,1/

&bcdef bcdir='xie',block=3,bctype=7,start=29,1,1,end=29,64,114,
       iblock=4,istart=1,1,1,iend=1,64,114,order=1,2,3/
&bcdef bcdir='eta',block=3,bctype=3,start=1,1,1,end=29,1,50/
&bcdef bcdir='eta',block=3,bctype=7,start=1,1,51,end=5,1,114,
       iblock=5,istart=5,1,51,iend=1,1,114,order=1,2,3/
&bcdef bcdir='eta',block=3,bctype=7,start=6,1,51,end=29,1,114,
       iblock=4,istart=24,1,51,iend=1,1,114,order=1,2,3/
&bcdef bcdir='eta',block=3,bctype=11,start=1,64,1,end=29,64,114/
&bcdef bcdir='zta',block=3,bctype=11,start=1,1,114,end=29,64,114/
&bcdef bcdir='zta',block=3,bctype=8,start=1,1,1,end=29,64,1/

&bcdef bcdir='xie',block=4,bctype=7,start=24,1,1,end=24,64,114,
       iblock=5,istart=1,1,1,iend=1,64,114,order=1,2,3/
&bcdef bcdir='eta',block=4,bctype=3,start=1,1,1,end=24,1,50/
&bcdef bcdir='eta',block=4,bctype=11,start=1,64,1,end=24,64,114/
&bcdef bcdir='zta',block=4,bctype=11,start=1,1,114,end=24,64,114/
```

```
&bcdef bcdir='zta',block=4,bctype=8,start=1,1,1,end=24,64,1/


&bcdef bcdir='xie',block=5,bctype=7,start=24,1,1,end=24,64,114,
       iblock=6,istart=1,1,1,iend=1,64,114,order=1,2,3/
&bcdef bcdir='eta',block=5,bctype=3,start=1,1,1,end=24,1,50/
&bcdef bcdir='eta',block=5,bctype=11,start=1,64,1,end=22,64,114/
&bcdef bcdir='eta',block=5,bctype=6,start=23,64,1,end=24,64,114/
&bcdef bcdir='zta',block=5,bctype=11,start=1,1,114,end=24,64,114/
&bcdef bcdir='zta',block=5,bctype=8,start=1,1,1,end=24,64,1/


&bcdef bcdir='xie',block=6,bctype=7,start=24,1,1,end=24,64,114,
       iblock=7,istart=1,1,1,iend=1,64,114,order=1,2,3/
&bcdef bcdir='eta',block=6,bctype=3,start=1,1,1,end=24,1,50/
&bcdef bcdir='eta',block=6,bctype=11,start=1,64,1,end=24,64,114/
&bcdef bcdir='zta',block=6,bctype=11,start=1,1,114,end=24,64,114/
&bcdef bcdir='zta',block=6,bctype=8,start=1,1,1,end=24,64,1/


&bcdef bcdir='eta',block=7,bctype=3,start=1,1,1,end=24,1,50/
&bcdef bcdir='eta',block=7,bctype=11,start=1,64,1,end=24,64,114/
&bcdef bcdir='zta',block=7,bctype=11,start=1,1,114,end=24,64,114/
&bcdef bcdir='zta',block=7,bctype=8,start=1,1,1,end=24,64,1/


&bcdef bcdir='eta',block=8,bctype=3,start=1,1,1,end=38,1,40/
&bcdef bcdir='xie',block=8,bctype=4,start=1,1,1,end=1,20,40/
&bcdef bcdir='xie',block=8,bctype=5,start=38,1,1,end=38,20,40/
&bcdef bcdir='zta',block=8,bctype=3,start=1,1,40,end=38,20,40/
&bcdef bcdir='zta',block=8,bctype=8,start=1,1,1,end=38,20,1/
&bcdef bcdir='end'/


&bcwake wbcdir='xie',wblock=3,wface=2,wbctype=1/
&bcwake wbcdir='xie',wblock=4,wface=1,wbctype=1/
&bcwake wbcdir='end'/
```

A.2   CFJA Case *init.input* File

```
200         !bc_max  the maximum of the BCs number defined in problem
8           !nb  the total number of blocks
29,64,114   !il,jl,kl  the cell's dimension of the grid of each block
38,64,114   !il,jl,kl  the cell's dimension of the grid of each block
29,64,114   !il,jl,kl  the cell's dimension of the grid of each block
24,64,114   !il,jl,kl  the cell's dimension of the grid of each block
```

```
24,64,114   !il,jl,kl  the cell's dimension of the grid of each block
24,64,114   !il,jl,kl  the cell's dimension of the grid of each block
24,64,114   !il,jl,kl  the cell's dimension of the grid of each block
38,20,40    !il,jl,kl  the cell's dimension of the grid of each block
2           !The number of additional poutlet condition
8,70.0000,87.00000,1.002.  !The block number,poutlet,ptotal and ttotal
8,70.0000,87.00000,1.002.  !The block number,poutlet,ptotal and ttotal
```

A.3 CAARC Building Case *datain* file

```
&consts
delta      = 0.0d+00, 0.0d+00, 0.0d+00, 0.0d+00, 0.0d+00,
                       ! Entropy cut-off for rho, rhou, rhov,
                       ! rhow and rhoe
epsfactor  = 1.00d-06, ! epsilon used in linear reconstruction
gamma      = 1.40d+00, ! Ratio of specific heats
prandtl    = 0.72d0,   ! Molecular Prandtl number
prt        = 0.9d0,    ! turbulent prandtl number
suther     = F,        ! = T: Sutherlands Law. = F: mu = T
tref       = 0.383d0,  ! Non-dimensional ref temperature in Sutherland
/

&flows
blen       = 2,        ! number of halo layers for block boundaries.
                       ! =2, under 3rd scheme;
                       ! =3, 5th scheme;
                       ! =4, 7th scheme
idimen     = 3,        ! = 1: 1-D, = 2: 2-D, = 3: 3-D
nl         = 5,        ! No. of eqs. =5, Laminar or BL model;
                       ! =6, SA model or DES
angl1      = 0.0d0,    ! inlet angle 1
angl2      = 0.0d0,    ! inlet angle 2
inviscid   = F,        ! = T: inviscid; = F: viscous
machinf    = 0.1d0,    ! Mach no. based on U_infinity and a_infinity
poutlet    = 71.42857, ! outlet static pressure
ptotal     = 71.78625, ! Total pressure at inlet
reynolds   = 160000,   ! Reynolds number
tintvl     = 0.05,     ! unsteady time interval
ttotal     = 1.008,    ! Total temperature at inlet
turb       = 1,        ! =0, Laminar flow or LES
                       ! =1 (nl=5), BL turbulence model;
                       ! =1 (nl=6), SA turbulence model or DES
```

```
      /

      &comp
      choice      = 'n',        ! ='y': from rstore. ='n': from initial value
      cfl         = 1.0d0,      ! CFL number
      checksteps  = 1,          ! print out status every # steps for monitoring
      dual_t      = 0,          ! 1: unsteady, 0: steady
      eps         = 1.d-12,     ! residual limit
      gcl         = 0,          ! geometry conservation in moving grid
                                ! =0, disabled; =1, enabled
      integrate   = 4,          ! =1, AF; =2, R-K; 3, Euler;
                                ! =4, GS; =5, LU-SGS; =6, LU-GSLR
      intersteps  = 50,         ! save results every # steps in computation
      iter_gs     = 2,          ! number of Gauss-Seidel sweeps
      kfactor     = 0.33333d0,  ! factor in linear reconstruction
      lhs_order   = 0,          ! =0, 1st order MUSCL for LHS matrices;
                                ! =1, 2nd or 3rd order.
      lhs_scheme  = 4,          ! =1, Roe;
                                ! =2, Zha;
                                ! =3, none,
                                ! =4, Van Leer (when RHS is not Roe scheme)
      limiter     = 0,          ! =0, no limiter;
                                ! =1, MINMOD ;
                                ! =2, SUPERBEE;
                                ! =3, A-T-VL
      moving      = 0,          ! moving grid, 0-stationary, 1-fixed, 2-induced
      nrbc_ex     = 0,          ! =0: no NRBC at exit;
                               ! =3: use Euler Method non-reflective BC at exit
      nstep       = 10000,      ! No. of time steps
      rhs_order   = 1,          ! =0, 1st order MUSCL (blen>=2);
                                ! =1, 2nd or 3rd order (blen>=2);
                                ! =4, 3rd-WENO (blen>=2);
                                ! =5, 5th order fixed stencil (blen=>3);
                                ! =6, 5th-WENO (blen=>3);
                                ! =7, 7th order fixed stencil (blen=>4);
                                ! =8, 7th-WENO (blen=>4)
      rhs_scheme  = 3,          ! =1,Roe; 2,Zha2; 3,Zha3; 4,Van Leer;
                                ! 5,Edwars; 6,Zha6; 7,AUSM+; 8:Zha;
                                ! 9:AUSMV; 10: AUSMD; 11: VAN LEER-HANEL
      strtp       = 0,          ! 0-no structure; 1-cylinder; 2-airfoil
      tsteps      = 20,          ! unsteady time marching stes using dual-time stepping
      unidt       = 0,          ! >0, Uniform time interval in whole domain
                                ! =0, Local time step
      vis_order   = 1,          ! The order of the viscous term.
                                !    =1, 2nd order(blen=2);
```

```
                                     !     =3, 4th order(blen=3);
                                     !     =5, 6th order(blen=4)
   velinit     = 1.d0,        ! dimensionless velocity initial value
   strm_dir    = 1,           ! main flow direction
   theta       = 0.d0,        ! initial velocity angle
   twpar       = 2,           ! 1<=twpar<=10, initial for omega when nl=7
   tkpar       = 5,           ! 2<=tkpar<=5, initial for k when nl=7
   xyz         = 0,0,0,       ! when moving >0
   vbd         = 0,0,0
   /


&coef1eq
   ides    = 0,              ! =0, 1EQ; =1, DES
   cdes    = 0.65d0,         ! parameter used in DES
   iblnu   = 1,              ! block number in which trip is placed
   ipt     = 1,              ! index of trip point in i-direction
   jpt     = 1,              ! index of trip point in j-direction
   kpt     = 1,              ! index of trip point in k-direction
   ic1     = 1,              ! ic1, ic2 and ic3 represent the i, j, k grid
   ic2     = 0,              ! spacing along the wall at the trip.
   ic3     = 0,              ! =0, no the direction; =1, along the direction
   tko   = 0.66666667d0,     ! constant used in SA 1EQ turbulence model
   cb1   = 0.1355d0,         ! constant used in SA 1EQ turbulence model
   cb2   = 0.622d0,          ! constant used in SA 1EQ turbulence model
   cap_k = 0.41d0,           ! constant used in SA 1EQ turbulence model
   cw2   = 0.3d0,            ! constant used in SA 1EQ turbulence model
   cw3   = 2.d0,             ! constant used in SA 1EQ turbulence model
   cv1   = 7.1d0,            ! constant used in SA 1EQ turbulence model
   ct1   = 0.0d0,            ! constant used in SA 1EQ turbulence model
   ct2   = 0.0d0,            ! constant used in SA 1EQ turbulence model
   ct3   = 0.0d0,            ! constant used in SA 1EQ turbulence model
   ct4   = 0.0d0 /           ! constant used in SA 1EQ turbulence model

&bcdef bcdir='xie',block=1,bctype=7,start=1,1,1,end=1,69,66,
       iblock=4,istart=32,1,1,iend=32,69,66,order=1,2,3/
&bcdef bcdir='xie',block=1,bctype=7,start=42,1,1,end=42,69,66,
       iblock=2,istart=1,1,1,iend=1,69,66,order=1,2,3/
&bcdef bcdir='eta',block=1,bctype=3,start=1,1,1,end=42,1,66/
&bcdef bcdir='eta',block=1,bctype=6,start=1,69,1,end=42,69,66/
&bcdef bcdir='zta',block=1,bctype=3,start=1,1,1,end=42,69,1/
&bcdef bcdir='zta',block=1,bctype=7,start=1,1,66,end=42,69,66,
       iblock=5,istart=1,1,1,iend=42,69,1,order=1,2,3/


&bcdef bcdir='xie',block=2,bctype=7,start=32,1,1,end=32,69,66,
       iblock=3,istart=1,1,1,iend=1,69,66,order=1,2,3/
```

```
&bcdef bcdir='eta',block=2,bctype=3,start=1,1,1,end=32,1,66/
&bcdef bcdir='eta',block=2,bctype=6,start=1,69,1,end=16,69,66/
&bcdef bcdir='eta',block=2,bctype=11,start=17,69,1,end=32,69,66/
&bcdef bcdir='zta',block=2,bctype=3,start=1,1,1,end=32,69,1/
&bcdef bcdir='zta',block=2,bctype=7,start=1,1,66,end=32,69,66,
       iblock=6,istart=1,1,1,iend=32,69,1,order=1,2,3/

&bcdef bcdir='xie',block=3,bctype=7,start=42,1,1,end=42,69,66,
       iblock=4,istart=1,1,1,iend=1,69,66,order=1,2,3/
&bcdef bcdir='eta',block=3,bctype=3,start=1,1,1,end=42,1,66/
&bcdef bcdir='eta',block=3,bctype=11,start=1,69,1,end=42,69,66/
&bcdef bcdir='zta',block=3,bctype=3,start=1,1,1,end=42,69,1/
&bcdef bcdir='zta',block=3,bctype=7,start=1,1,66,end=42,69,66,
       iblock=7,istart=1,1,1,iend=42,69,1,order=1,2,3/

&bcdef bcdir='eta',block=4,bctype=3,start=1,1,1,end=32,1,66/
&bcdef bcdir='eta',block=4,bctype=11,start=1,69,1,end=16,69,66/
&bcdef bcdir='eta',block=4,bctype=6,start=17,69,1,end=32,69,66/
&bcdef bcdir='zta',block=4,bctype=3,start=1,1,1,end=32,69,1/
&bcdef bcdir='zta',block=4,bctype=7,start=1,1,66,end=32,69,66,
       iblock=8,istart=1,1,1,iend=32,69,1,order=1,2,3/

&bcdef bcdir='xie',block=5,bctype=7,start=1,1,1,end=1,69,66,
       iblock=8,istart=32,1,1,iend=32,69,66,order=1,2,3/
&bcdef bcdir='xie',block=5,bctype=7,start=42,1,1,end=42,69,66,
       iblock=6,istart=1,1,1,iend=1,69,66,order=1,2,3/
&bcdef bcdir='eta',block=5,bctype=7,start=1,1,1,end=42,1,66,
       iblock=9,istart=1,32,1,iend=42,32,66,order=1,2,3/
&bcdef bcdir='eta',block=5,bctype=6,start=1,69,1,end=42,69,66/
&bcdef bcdir='zta',block=5,bctype=1,start=1,1,66,end=42,69,66/

&bcdef bcdir='xie',block=6,bctype=7,start=32,1,1,end=32,69,66,
       iblock=7,istart=1,1,1,iend=1,69,66,order=1,2,3/
&bcdef bcdir='eta',block=6,bctype=7,start=1,1,1,end=32,1,66,
       iblock=9,istart=42,32,1,iend=42,1,66,order=2,1,3/
&bcdef bcdir='eta',block=6,bctype=6,start=1,69,1,end=16,69,66/
&bcdef bcdir='eta',block=6,bctype=11,start=17,69,1,end=32,69,66/
&bcdef bcdir='zta',block=6,bctype=1,start=1,1,66,end=32,69,66/

&bcdef bcdir='xie',block=7,bctype=7,start=42,1,1,end=42,69,66,
       iblock=8,istart=1,1,1,iend=1,69,66,order=1,2,3/
&bcdef bcdir='eta',block=7,bctype=7,start=1,1,1,end=42,1,66,
       iblock=9,istart=42,1,1,iend=1,1,66,order=1,2,3/
&bcdef bcdir='eta',block=7,bctype=11,start=1,69,1,end=42,69,66/
&bcdef bcdir='zta',block=7,bctype=1,start=1,1,66,end=42,69,66/
```

```
&bcdef bcdir='eta',block=8,bctype=7,start=1,1,1,end=32,1,66,
        iblock=9,istart=1,1,1,iend=1,32,66,order=2,1,3/
&bcdef bcdir='eta',block=8,bctype=11,start=1,69,1,end=16,69,66/
&bcdef bcdir='eta',block=8,bctype=6,start=17,69,1,end=32,69,66/
&bcdef bcdir='zta',block=8,bctype=1,start=1,1,66,end=32,69,66/

&bcdef bcdir='zta',block=9,bctype=3,start=1,1,1,end=42,32,1/
&bcdef bcdir='zta',block=9,bctype=1,start=1,1,66,end=42,32,66/


&bcdef bcdir='end'/



&bcwake wbcdir='eta',wblock=1,wface=1,wbctype=0/
&bcwake wbcdir='eta',wblock=1,wface=2,wbctype=0/
&bcwake wbcdir='end'/
```

A.4   CAARC Building Case *init.input* File

```
200          !bc_max  the maximum of the BCs number defined in problem
9            !nb  the total number of blocks
42,69,66     !il,jl,kl  the density of the grid of each block
32,69,66     !il,jl,kl  the density of the grid of each block
42,69,66     !il,jl,kl  the density of the grid of each block
32,69,66     !il,jl,kl  the density of the grid of each block
42,69,66     !il,jl,kl  the density of the grid of each block
32,69,66     !il,jl,kl  the density of the grid of each block
42,69,66     !il,jl,kl  the density of the grid of each block
32,69,66     !il,jl,kl  the density of the grid of each block
42,32,66     !il,jl,kl  the density of the grid of each block
0            !The number of additional poutlet condition
```

References

[1] N. Qin, A. Valvalle, N. Le Moigne, M. Laban, K. Hackett, and P. Weinerfelt, "Aerodynamic Considerations of Blended Wing Body Aircraft," *Aircraft Design*, vol. 40, pp. 231–343, 2004.

[2] A. L. Bolsunovsky, N. P. Buzoverya, B. I. Gurevich, V. E. Denosov, A. I. Dunaevsky, L. M. Shkadov, O. V. Sonin, A. J. Udzhuhu, and J. P. Zhurihin, "Flying Wing - Problems and Decisions," *Aircraft Design*, vol. 4, pp. 193–219, 2001.

[3] B. Mialon, T. Fol, and C. Bonnaud, "Aerodynamic Optimization of Subsonic Flying Wing Configurations." AIAA Paper 2002-2931, 2002.

[4] J. Akerman, "Sustainable Air Transport – On Track in 2050," *Transportation Research Part D: Transport and Environment*, vol. 13-5, pp. 111–126, March 2005.

[5] J. Aguirre, B.-Y. Wang, and Z. G-C., "Design and Study of Engineless Airplane Using Co-Flow Jet Airfoil." AIAA Paper 2007-4441, July 2007.

[6] G.-C. Zha and D. C. Paxton, "A Novel Flow Control Method for Airfoil Performance Enhancement Using Co-Flow Jet." Chapter 10, *Applications of Circulation Control Technologies*, p. 293-314, Vol. 214, Progress in Astronautics and Aeronautics, AIAA Book Series, Editors: Joslin, R. D. and Jones, G.S., 2006.

[7] G.-C. Zha, B. Carroll, C. Paxton, A. Conley, and A. Wells, "High Performance Airfoil with Co-Flow Jet Flow Control." AIAA-Paper-2005-1260, January, 2005.

[8] G.-C. Zha, C. Paxton, A. Conley, A. Wells, and B. Carroll, "Effect of Injection Slot Size on High Performance Co-Flow Jet Airfoil," *AIAA Journal of Aircraft*, vol. 43, pp. 987–995, 2006.

[9] G.-C. Zha and W. Gao, "Analysis of Jet Effects on Co-Flow Jet Airfoil Performance with Integrated Propulsion System." AIAA Paper 2006-0102, AIAA 44th Aerospace Sciences Meeting and Exhibit, January 8-12, 2006.

[10] J. Steger and W. R., "Flux Vector Splitting of the Inviscid Gasdynamic Equations with Application to Finite-Difference Methods," *Journal of Computational Physics*, vol. 40, pp. 263–293, 1981.

[11] G.-C. Zha, "A Low Diffusion E-CUSP Upwind Scheme for Transonic Flows." AIAA Paper 2004-2707, to appear in AIAA Journal, 34th AIAA Fluid Dynamics Conference, June 28 - July 1 2004.

[12] B.-Y. Wang and G.-C. Zha, "Comparison of a Low Diffusion E-CUSP and the Roe Schemes for RANS Calculation." AIAA Paper 2008-0596, 2008.

[13] J. R. Edwards, "A Low-Diffusion Flux-Splitting Scheme for Navier-Stokes Calculations." AIAA Paper 95-1703-CP, June, 1995.

[14] J. R. Edwards, "A Low-Diffusion Flux-Splitting Scheme for Navier-Stokes Calculations," *Computer & Fluids*, vol. 6, pp. 635–659, 1997.

[15] B. Van Leer, "Flux-Vvector Splitting for the Euler Equations," *Lecture Note in Physics*, vol. 170, pp. 507–512, 1982.

[16] P. Roe, "Approximate Riemann Solvers, Parameter Vectors, and Difference Schemes," *Journal of Computational Physics*, vol. 43, pp. 357–372, 1981.

[17] B. Baldwin and H. Lomax, "Thin-layer approximation and algebraic model for separated turbulent flows." AIAA Paper 78-257, 1978.

[18] P. Spalart and A. S., "A One-Equation Turbulence Model for Aerodynamic Flows." AIAA Paper 92-0439, 1992.

[19] P. Spalart, W.-H. Jou, M. Strelets, and S. Allmaras, "Comments on the Feasibility of LES for Wings, and on a Hybrid RANS/LES Approach." Advances in DNS/LES, 1st AFOSR Int. Conf. on DNS/LES, Greyden Press, Columbus, H., Aug. 4-8, 1997.

[20] B.-Y. Wang, "A General Sub-Domain Boundary Mapping Procedure For Structured Grid Implicit CFD Parallel Computation." AIAA Paper 2007-4432, 2007.

[21] G.-C. Zha, "Low Diffusion Efficient Upwind Scheme ," *AIAA Journal*, vol. 43, pp. 1137–1140, 2005.

[22] X.-Y. Chen and G.-C. Zha, "Fully Coupled Fluid-Structural Interactions Using an Efficient High Solution Upwind Scheme." AIAA Paper 2004-2331, to appear in Journal of Fluids and Structures, 2005.

[23] Z.-J. Hu and G.-C. Zha, "Simulation of 3D Flows of Propulsion Systems Using an Efficient Low Diffusion E-CUSP Upwind Scheme." AIAA Paper 2004-3928, 40th AIAA/ASME/SAE/ASEE Joint Propulsion Conference and Exhibit, 11 - 14 July 2004.

[24] G.-C. Zha and C. Paxton, "A Novel Airfoil Circulation Augment Flow Control Method Using Co-Flow Jet." NASA/CP-2005-213509, June 2005; AIAA Paper 2004-2208, June 2004.

[25] E. M. Greitzer, C. S. Tan, and M. B. Graf, *Internal Flow*. Cambridge University Press, 2004.

[26] W. L. I. Sellers, B. A. Singer, and L. D. Leavitt, "Aerodynamics for Revolutionary Air Vehicles." AIAA 2004-3785, June 2003.

[27] M. Gad-el Hak, "Flow Control: The Future," *Journal of Aircraft*, vol. 38, pp. 402–418, 2001.

[28] M. Gad-el Hak, *Flow Control, Passive, Active, and Reactive Flow Management*. Cambridge University Press, 2000.

[29] W. Zha, G.-C.and Gao, C. D. Paxton, and A. Palewicz, "Numerical Investigation of Co-Flow Jet Airfoil with and without Suction." AIAA Paper 2006-1061, 2006.

[30] G.-C. Zha and W. Gao, "Analysis of Jet Effects on Co-Flow Jet Airfoil Performance with Integrated Propulsion System." AIAA Paper 2006-0102, January 2006.

[31] G.-C. Zha, B. Carroll, C. Paxton, A. Conley, and A. Wells, "High Performance Airfoil with Co-Flow Jet Flow Control," *AIAA Journal*, vol. 45, pp. 2087–2090, 2007.

[32] A. Wells, "Experimental investigation of an airfoil with co-flow jet flow control." Master's Thesis, Dept. of Mechanical and Aerospace Engineering, University of Florida, June 2005.

[33] C. Dragoiescu, J. Garber, and S. Kumar, "A Comparison of Force Balance and Pressure Integration Techniques for Prediting Wind-Induced Responses of Tall Buildings." RWDI Internal Literature, Guelph, Ontario, Canada, 2007.

[34] C. Paxton, G.-C. Zha, and D. Car, "Design of the Secondary Flow System for a Co-Flow Jet Cascade." AIAA Paper 2004-3928, July, 2004.

[35] J. Aguirre, N. Chamie, and V. Casado, "Mars Intelligent Reconaissance Aerial and Ground Explorer (MIRAGE)." AIAA Paper 007-0244, January 2007.